[AMERICAN JOURNAL OF SCIENCE, VOL. 321, OCTOBER, 2021, P. 1111–1163, DOI 10.2475/08.2021.01]

American Journal of Science

OCTOBER 2021

ROCK WEATHERING AND NUTRIENT CYCLING ALONG AN ERODOSEQUENCE

FRIEDHELM VON BLANCKENBURG[*,**,†], JAN A. SCHUESSLER[*,***],
JULIEN BOUCHEZ[*,§], PATRICK J. FRINGS[*], DAVID UHLIG[*,§§],
MARCUS OELZE[*], DANIEL A. FRICK[*], TILAK HEWAWASAM[§§§],
JEANNIE DIXON[‡], and KEVIN NORTON[‡‡]

ABSTRACT. How flowing water and organisms can shape Earth's surface, the Critical Zone, depends on how fast this layer is turned over by erosion. To quantify the dependence of rock weathering and the cycling of elements through ecosystems on erosion we have used existing and new metrics that quantify the partitioning and cycling of elements between rock, saprolite, soil, plants, and river dissolved and solid loads. We demonstrate their utility at three sites along a global transect of mountain landscapes that differ in erosion rates – an "erodosequence". These sites are the Swiss Central Alps, a rapidly-eroding, post-glacial mountain belt; the Southern Sierra Nevada, USA, eroding at moderate rates; and the slowly-eroding tropical Highlands of Sri Lanka. The backbone of this analysis is an extensive data set of rock, saprolite, soil, water, and plant geochemical and isotopic data. This set of material properties is converted into process rates by using regolith production and weathering rates from cosmogenic nuclides and river loads, and estimates of biomass growth. Combined, these metrics allow us to derive elemental fluxes through regolith and vegetation. The main findings are: 1) the rates of weathering are set locally in regolith, and not by the rate at which entire landscapes erode; 2) the degree of weathering is mainly controlled by regolith residence time. This results in supply-limited weathering in Sri Lanka where weathering runs to completion in the regolith, and kinetically-limited weathering in the Alps and Sierra Nevada where soluble primary minerals persist; 3) these weathering characteristics are reflected in the sites' ecosystem processes, namely in that nutritive elements are intensely recycled in the supply-limited setting, and directly taken up from soil and rock in the kinetically settings; 4) the weathering rates are not controlled by biomass growth; 5) at all sites we find a deficit in river solute export when compared to solute production in regolith, the extent of which differs between elements. Plant uptake followed by litter export might explain this deficit for biologically utilized elements of high solubility, and rare, high-discharge flushing events for colloidal-bound elements of low solubility. Our data and new metrics have begun to serve for calibrating metal

---

[*] GFZ German Research Centre for Geosciences, Section Earth Surface Geochemistry, Telegrafenberg, 14473 Potsdam, Germany

[**] Also at: Institute of Geological Sciences, Freie Universität Berlin, Malteserstr. 74-100, 12249 Berlin, Germany

[***] Present address: Thermo Fisher Scientific, Hanna-Kunath-Str. 11, 28199 Bremen, Germany

[§] Present address: Université de Paris, Institut de physique du globe de Paris, 1 rue Jussieu, F-75005 Paris, France

[§§] Present address: Forschungszentrum Jülich GmbH, Institute of Bio- and Geosciences, IBG-3: Agrosphere, Wilhelm-Johnen-Str., 52425 Jülich, Germany

[§§§] Department of Geography, Center for Environmental Studies (CES), University of Peradeniya, 20400, Sri Lanka

[‡] Department of Earth Sciences, Montana State University, Bozeman, Montana 59717, USA

[‡‡] School of Geography, Environment and Earth Sciences, Victoria University of Wellington, New Zealand

[†] Corresponding author: fvb@gfz-potsdam.de

isotope systems in the weathering zone, the isotope ratios of which depend on the flux partitioning between the compartments of the Critical Zone. We demonstrate this application in several isotope geochemical companion papers.

Key words: Critical Zone, erosion rate, weathering rate, biogenic weathering, soil formation, river geochemistry, nutrient cycling, metal stable isotopes

INTRODUCTION

Soils in sloping landscapes experience mass loss by erosion and weathering. At steady state, soil-forming processes balance these degradational processes, such that all state variables of the system are independent of time. Under these conditions a soil system as a whole has no age, but rather is comprised of constituents that move through it and remain within for a duration called residence time. The steady-state model requires that, averaged over the time scale of the regolith residence time, mass loss by particle and solute export is balanced by regolith production (where the term "regolith" is taken to mean the sum of consolidated and unconsolidated material above the weathering front, including soil). Because there are non-linear feedbacks between regolith thickness, regolith production, and regolith removal, the expectation for most boundary conditions is a regolith of non-zero but finite thickness. The occurrence and persistence of regolith across about 94 % of the ice-free terrestrial land surface (Hengl and others, 2014) – even though half of the terrestrial land surface has slope angles exceeding 5° (Larsen and others, 2014) and is thus subject to significant erosion – supports this view. Yet the mere presence and persistence of a soil cover cannot be used as a demonstration that a balance exists between soil formation and degradation. However, typical regolith residence times ($\leq 10^4$ yr) are often shorter than or equal to the time scales over which tectonics and climate vary ($\geq 10^4$ yr). This suggests that much of the Earth surface operates in a manner that is consistent with the steady-state model of soil formation.

In a steady-state eroding system the residence time of solid material in the regolith sets the weathering degree (Stallard, 1995; Waldbauer and Chamberlain, 2005; Gabet and Mudd, 2009). All else being equal, the longer the time available for the solid material to weather, the greater the degree of weathering. Weathering degrees and rates are also modulated by the residence time of water in the subsurface. Ultimately water flow path lengths and the degree of weathering of the regolith flushed by water flow set the time required for a weathering reaction to reach equilibrium (Maher, 2010, 2011). This "reactivity" of regolith over a given length scale is predicted to be low in slowly eroding landscapes with thick weathering zones, and high in rapidly eroding landscapes with thin weathering zones and short regolith residence time (Bazilevskaya and others, 2012).

As the third player besides regolith residence time and water flow, the activity of biota is intimately linked to the state of the regolith (Brantley and others, 2011; Porder, 2019). The Critical Zone concept encompasses regolith processes and a suite of linked biotic interactions. The Critical Zone is defined as the layer extending from the top of unweathered bedrock to the top of the vegetation (Chorover and others, 2007; Lin, 2010a; Brantley and others, 2016; Riebe and others, 2017). In this layer, plants, animals, and micro-organisms influence soil structure and resistance to erosion (Roering and others, 2010; Ghestem and others, 2013; Pawlik and others, 2016,). Biota impacts the water cycle (Brooks and others, 2010; Fan and others, 2017) for example through the creation or destruction of secondary porosity and preferential flow paths. Biota may also enhance weathering rates through several mechanisms. These include aiding secondary mineral formation and the production of bio-minerals, or the exudation of organic acids and ligands. The production of subsurface CO_2 via root and microorganism respiration results in below-ground CO_2 partial pressures

($p$$CO_2$) that can be up to two orders of magnitude higher than in the atmosphere (Lucas, 2001; Amundson and others, 2007), increasing mineral decomposition rates via kinetic and thermodynamic controls. Plants and associated microorganisms also weather minerals directly. Fungi and bacteria can accelerate mineral dissolution kinetics, leading to the release of mineral nutrients that can be supplied to higher plants in return for photosynthates (van Scholl and others, 2008; Uroz and others, 2009). Some ectomycorrhizal fungi are able to extract nutrients such as P, K, Ca, Mg, and Fe directly from minerals (Jongmans and others, 1997; Hoffland and others, 2003; Balogh-Brunstad and others, 2008; Smits and others, 2012). As a result, it is not surprising that plants and associated microbiota are suggested to impact weathering fluxes (Moulton and others, 2000; Berner and others, 2003; Chaudhuri and others, 2007; Cornelis and others, 2009; Riotte and others, 2014). But a counter-perspective – namely how ecosystem nutrition is influenced by the state of the regolith – is just as relevant (Chadwick and Asner, 2016, 2020).

The exploration of the interactions between weathering processes and ecosystem nutrition in well-characterized natural sites is an important avenue of research to pursue. However, many of the studies that have addressed these interactions have done so within a perspective that differs from the steady-state framework described above. These studies tend to make use of geomorphically stable surfaces in which the degree of rock weathering and soil formation reflect a discrete soil age for a given environment. In this "continuous evolution model" of soil formation, soils and the weathered substrate beneath them evolve from an initially pristine state towards an altered and chemically depleted state with time as the only independent variable (Lin, 2010b; Egli and others, 2014). Its classical study object is the "chronosequence" – a series of non-eroding field sites with identical rock type, topography, and climate, yet of differing soil age in which a 'space-for-time' approach can be used to explore ecosystem succession as the degree of weathering evolves (Blum and Erel, 1997; Chadwick and others, 1999; Sauer and others, 2007, White and others, 2008; Bernasconi and others, 2011; Porder and Hilley, 2011; Mavris and others, 2012; Laliberte and others, 2013). Classical examples include chronosequences developed on lava flows of known age (Chadwick and others, 1999), or progressively uplifted beach terraces with known timing of isolation from wave attack (White and others, 2008). In the continuous evolution model, ecosystems evolve together with soils. Ecology and soil development are linked via progressive increases in soil stability and water retention capacity, and decreases in mineral nutrient availability (Vitousek and Farrington, 1997; Lambers and others, 2008; Laliberte and others, 2013,). In contrast, in the steady-state model, regolith replenishment by uplift and erosion sets the upward advection of mineral nutrients through the Critical Zone (Vitousek and others, 2003; Waldbauer and Chamberlain, 2005; Porder and others, 2007; Buendía and others, 2010; Uhlig and von Blanckenburg, 2019), so the combination of regolith residence time and mineral weathering rates determines whether an ecosystem is limited in a specific mineral nutrient.

There has been considerable focus on interactions between weathering and ecosystem nutrition within the continuous evolution model, but less attention has been paid to these interactions in eroding settings, although they characterize the majority of Earth's surface (Buss and others, 2010, 2017; Chadwick and Asner, 2016; Wilcke and others, 2017; Oeser and others, 2018, Uhlig and von Blanckenburg, 2019). Further, many studies that do investigate weathering and ecosystem processes are focused on a single location and thus do not systematically explore a gradient in erosion rate or regolith residence time. We identify at least three motivations to explore the "steady-state model" with field studies that quantify how both weathering and ecosystem nutrition are governed by erosion. First, half of the terrestrial land surface has slope angles exceeding 5° (Larsen and others, 2014) and is thus subject to significant erosion. These surfaces fall into the "steady state" category. Second, the importance of such studies becomes more apparent when considering that the regulation of Earth's climate and global biogeochemical fluxes are ultimately governed by weathering rates or land surface reactivity, which in turn are set by erosion rate (Berner and others, 1983; Kump and Arthur, 1997; Maher and Chamberlain, 2014; Caves and others, 2016; Frings and Buss, 2019), where it has been suggested that land plants play a key role in enhancing weathering and thus the drawdown of atmospheric CO_2 (Berner and others, 2003; Pagani and others, 2009). Third, quantitative data on absolute and relative fluxes and their partitioning between compartments can now routinely be obtained from a suite of isotope systems. Such isotope systems include *in situ* cosmogenic ^{10}Be (Heimsath and others, 1997; Granger and Riebe, 2007), meteoric cosmogenic $^{10}Be/^{9}Be$ (Maher and von Blanckenburg, 2016; von Blanckenburg and others, 2012), or metal and metalloid stable isotope systems, including $^{7}Li/^{6}Li$, $^{26}Mg/^{24}Mg$, or $^{30}Si/^{28}Si$ (Bouchez and others, 2013; Sullivan and others, 2016). At the same time, field data from well-characterized eroding settings can be used to calibrate and thus improve our interpretative ability of these novel isotope approaches in the Critical Zone.

Here we present a study of three sites across the globe that cover a gradient in erosion rates, but with similar lithology (felsic igneous or metamorphic rock). Our sites are located in the Swiss Central Alps (A), a post-glacial mountain belt that is eroding most rapidly of the three sites, when quantifying erosion at the landscape scale; the Southern Sierra Nevada (SN), USA in which the landscape is eroding at moderate rates; and the slowly eroding landscapes in the tropical Highland of Sri Lanka (SL). At these sites the regolith is permanently turned over by erosion, so this transect is not a chronosequence, but an "erodosequence".

Weathering has been extensively explored in previous studies in the Swiss Central Alps (Norton and von Blanckenburg, 2010; Norton and others, 2010); the Southern Sierra Nevada, which is also a US-Critical Zone Observatory (Dixon and others, 2009a, 2009b; Hahm and others, 2014; McCorkle and others, 2016; Hunsaker and Johnson, 2017), and the Highlands of Sri Lanka (Hewawasam and others, 2003, 2013; von Blanckenburg and others, 2004; Behrens and others, 2015, 2021). We supply an extensive set of new rock, saprolite, soil, river water, soil water, and plant chemical and isotopic data from the three sites that we combine with a compilation of previously published denudation-, regolith production-, erosion-, and weathering rates from cosmogenic nuclides. This data is available in a comprehensive open-access data publication (von Blanckenburg and others, 2021). We then suggest a set of simple metrics, many of which are novel, that quantify the partitioning and cycling of elements between rock, saprolite, soil, plants, river dissolved, and river sedimentary loads. With these metrics, we attempt to make the quantification of weathering and plant biogeochemical fluxes tractable. In a series of companion papers we show the application of these metrics to new stable isotope data from these field sites, namely those of Si (Frings and others, 2021a) combined with the Ge/Si "pseudoisotope" ratio (Frings and others, 2021b), and stable Sr (Bouchez and von Blanckenburg, 2021). These studies complement previously reported applications of Mg stable isotopes at these sites (Uhlig and others, 2017; Schuessler and others, 2018).

CONCEPTUAL FRAMEWORK

Chronosequences and Erodosequences

Using a simple mass balance model, we display the basic concepts of a chronosequence and an erodosequence in figure 1. For a chronosequence, the sampling sites

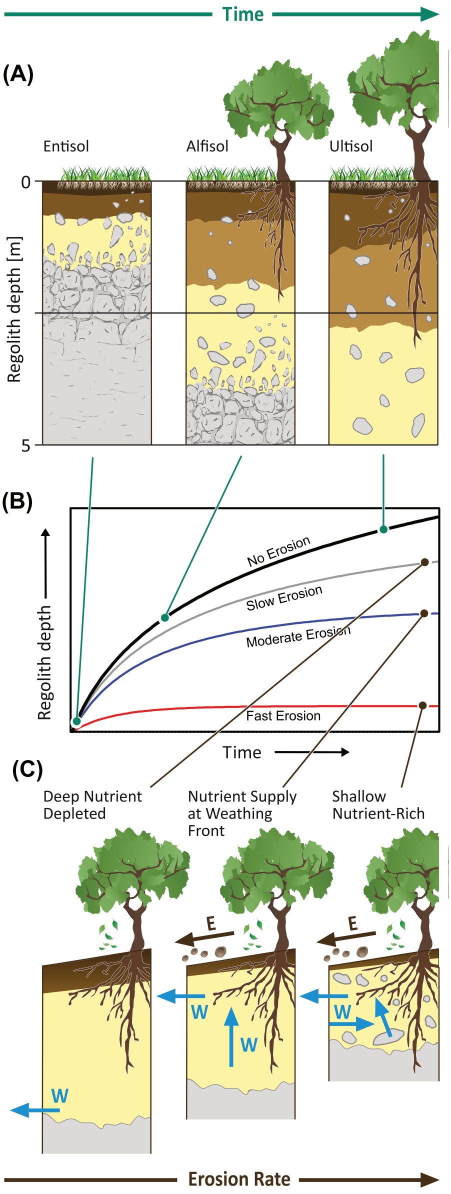

Fig. 1. The concepts of a "chronosequence" (A) after Lin (2010b) and an "erodosequence" (C) this study. The curves in (B) schematically show how the development of weathering zone thickness may depend on erosion rate. The black curve shows the predicted increase in regolith thickness in the case of no erosion - a "chronosequence", where soil development is purely a function of age. The green pointers show the three potential soil evolution stages shown in (A). The grey, blue, and red curves show the increase in thickness as a function of erosion rate for three rates typical of tectonically quiescent uplands ("slow"), tectonically active low mountain range ("moderate") and the regolith production limit in high, active mountains ("fast"). After some time, typically corresponding to $> 10^4$ yrs, the weathering zone attains steady-state thickness. At this steady state, the characteristics of the weathering zone differ depending on erosion rate, resulting in an "erodosequence".

are chosen for their lack of significant surface erosion, and the development of these sites with time conforms to the "continuous evolution model". Figure 1A (after Lin, 2010b) shows that with time (green arrow) soils thicken, and soil horizons develop. Figure 1C shows the "steady-state model". Here, all three settings are invariant with time, but span a gradient of erosion rates (brown arrow) and thus constitute an "erodosequence".

For illustrational purposes we show in figure 1B possible scenarios for the temporal evolution of regolith thickness as a function of erosion rate. In these scenarios regolith thickness increases with time from an initial pristine state, for example, a freshly exposed rock surface. Unless erosion is zero (upper black curve in fig. 1B) regolith thickness eventually attains a finite and constant thickness once regolith production is balanced by mass removal via physical erosion and chemical weathering. These scenarios assume that at steady state, regolith thickness is a function of erosion rate, in accordance with observations and concepts from soil studies (Heimsath and others, 1997; Ferrier and Kirchner, 2008). To date, little direct evidence supports a dependence of whole weathering zone thickness on erosion rate (Hayes and others, 2020), though this assumption is not unlikely. First, there are known mechanisms that may couple weathering front propagation at depth with erosion rate at the surface (Lebedeva and others, 2010; Behrens and others, 2015). Second, a balance between weathering front propagation and erosion is a necessary requirement to explain the prevalence of regolith on most landscapes over extended time scales. Third, the depth over which this balance is established depends on the factors that control the rate and degree of weathering, like fluid flow, fluid undersaturation, development of porosity, soil CO_2 input, and biogenic activity. These are more effective at shallow depth (Hilley and others, 2010, Maher, 2010), and fast regolith production is thus favoured at fast erosion.

Regardless of the under-constrained functional expression that links regolith production at depth with surface lowering, we see important conceptual differences in time over which regolith in an erodosequence attains steady state and how this time is reflected in its properties. The grey, blue, and red curves show the temporal evolution of regolith thickness for a slow, a moderate, and a fast erosion rate, respectively. In the slowest erosion rate setting, steady-state thickness is attained last. When primary minerals persist at the regolith surface, the weathering regime is called "kinetically limited" (Dixon and others, 2012) because mineral dissolution is controlled by dissolution kinetics unless fluids are saturated in which case the regime is at the "thermodynamic limit" (Maher, 2010). Conversely, when the erosion rate is sufficiently slow that primary minerals are entirely lost at the top of the regolith, the regime is termed "supply limited" as weathering scales linearly with the supply of weatherable primary minerals into the weathering zone by regolith production (Dixon and others, 2012).

Ecosystem states will, to some extent, reflect these weathering regimes. In the continuous-evolution (chronosequence) case, a co-evolution of plant communities with soil properties – termed a succession – occurs, until after sufficient time a relatively stable state is attained. A classic example would be the recolonization of land following a disturbance, where ecosystem composition, diversity, and functioning evolve in a manner that follows certain patterns (Birks and Birks, 2004, Wardle and others, 2004). In the steady-state case, a succession does not take place in the absence of a change of boundary conditions (for example, climate, tectonic uplift rate) or some aspect of ecosystem functioning (for example, arrival of invasive species). Each weathering zone state is then associated with a particular state of the ecosystems. Mineral nutrient supply as one possible control over ecosystem nutrition is shown in the lower panel: the slowly eroding setting (fig. 1, left) is strongly depleted in mineral nutrients like phosphorus or magnesium. Under these conditions, ecosystems will be nourished by atmospheric inputs (Hedin and others, 2003) and conserve nutrients by recycling within topsoil to prevent nutrient limitation (Lang and others, 2016). In the quickly eroding setting (fig. 1, right) a rich stock of mineral nutrients is available in the regolith and as long as plants have the ability to access them, ecosystems are not limited by availability of phosphorus or other mineral nutrients (Porder and others, 2007; Porder, 2019). Landscape rejuvenation in the form of river incision, for example, was shown to set higher foliar concentrations of P and K in the trees that grow on the incised parts than in non-incised segments of the landscape (Chadwick and Asner, 2016). At intermediate erosion rates (fig. 1, center) minerals are depleted above the weathering front, and thus access to fresh nutrients may only be possible at the weathering front (Uhlig and others, 2020).

Metrics for the eroding Critical Zone

The aim of this study is to provide a framework that allows for testing these predictions by quantifying element partitioning and fluxes in the Critical Zone and thus to trace the apportionment of elements released in the Critical Zone among different pools. Here, we use established methods to determine regolith production rates, degree of chemical depletion, and weathering rates (Riebe and others, 2003; Brantley and Lebedeva, 2011), and then apply a suite of metrics to quantify ecosystem fluxes (first introduced by Uhlig and others, 2017; Uhlig and von Blanckenburg, 2019) (table 1; fig. 2).

Weathering Zone Metrics

The regolith production rate *RP* is the rate at which unweathered rock is converted into weathered rock, that is, regolith, at the weathering front. *RP* itself is difficult to determine. Disequilibrium in the uranium decay series has recently been successfully employed for *RP* determination (Dosseto and others, 2012; Chabaux and others, 2013; Schoonejans and others, 2016), but is not attempted here. Instead, we assume that *RP* at depth is equal to the total denudation rate ($D_{regolith}$), and by doing so rely on the steady-state assumption of constant thickness that is inherent to the steady-state model. This means we can use denudation rates determined by *in situ* cosmogenic ^{10}Be in soil quartz (Granger and Riebe, 2007). Quartz ^{10}Be concentrations reflect the rate of mass loss by physical erosion E at the surface and dissolved mass loss by chemical weathering W above the cosmic ray attenuation depth, corresponding to approximately 60 cm for rock and 100 cm for soil. As with any flux determination based on cosmogenic nuclides, *RP* estimated in this manner integrates over the residence time of regolith in the upper 60 cm of rock-equivalent (or *ca.* 100 cm of soil), typically between 10^3 and 10^5 years, depending on denudation rate (von Blanckenburg, 2005).

$$RP = D_{regolith} \tag{1}$$

If chemical mass loss occurs below this depth, the ^{10}Be-derived denudation rate must be corrected (for example, Dixon and others, 2009a; Riebe and Granger, 2013), which is often achieved with the ratio of the concentration of an insoluble element Xi (for example, Zr, Nb) at below the cosmic ray attenuation depth to that from bedrock.

$$RP = D_{regolith} \times \frac{[Xi]_{saprolite}}{[Xi]_{bedrock}} \tag{2}$$

Note that in the following $D_{regolith}$ is simply referred to as D.

TABLE 1

Variables in the "erodosequence"

Equation	Name	Description	Formula	Interpretation
(1)	***RP*** *(t km^{-2}yr^{-1})*	Regolith Production Rate	$D_{regolith}$	Regolith production rate assuming steady regolith thickness; then *RP* is identical to the denudation rate $D_{regolith}$ from cosmogenic nuclides.
(2)		Regolith Production Rate corrected for dissolved mass loss	$D_{regolith} \times \frac{[Xi]_{saprolite}}{[Xi]_{bedrock}}$	Correction for chemical mass loss beneath the cosmic ray attenuation pathway.
(3)	***RP^X*** *(t km^{-2}yr^{-1})*	Regolith Production Rate of Element X	$RP \times [X]_{rock}$	Transfer of *X* from bedrock to regolith at the weathering front.
(4)	***CDF*** *dimensionless*	Chemical Depletion Fraction	$1 - \frac{[Xi]_{unweathered\ bedrock}}{[Xi]_{weathered\ regolith}}$	Fractional net mass loss from regolith relative to bedrock. *CDF* = 0: no net loss. *CDF* = 0.5: approximately maximum loss of *X* in granitoid rock. Here we used Zr for *Xi*.
(5)	τ_{Xi}^{X} *dimensionless*	Elemental Depletion or Gain Coefficient	$\frac{[Xi]_{unweathered\ bedrock}}{[Xi]_{weathered\ regolith}} \times \frac{[X]_{weathered\ regolith}}{[X]_{unweathered\ bedrock}} - 1$	Fractional mass loss or gain of an element relative to bedrock. $\tau_{Xi}^{X} < 0$: net elemental loss. $\tau_{Xi}^{X} > 0$: net elemental gain (e.for example: caused by atmospheric inputs). Here we used *Zr* for *Xi*.
(6)	$W_{regolith}$ *(t km^{-2}yr^{-1})*	Regolith Weathering Rate	$RP \times (CDF)$	Rate of net dissolved mass loss from regolith from regolith chemistry and cosmogenic nuclides.
(7)	W_{river} *(t km^{-2}yr^{-1})*	River Weathering Rate	$\sum_{i=1}^{365} \frac{[Cations + SiO_2]_{river_i} \cdot Q_i}{A}$	Rate of net dissolved mass loss from a catchment; calculated from river dissolved loads.
(8)	$W_{regolith}^{X}$ *(t km^{-2}yr^{-1})*	Regolith Weathering Rate of Element X	$RP^X \times (-\tau_{Xi}^{X})$	Net solubilisation flux of element *X*; release flux of *X* from minerals minus the flux of incorporation of X into secondary minerals.
(9)	W_{river}^{X} *(t km^{-2}yr^{-1})*	River Weathering Rate of Element X	$\sum_{i=1}^{365} \frac{[X]_{river_i} \times Q_i}{A}$	Dissolved river flux of element *X*.

Table 1

(continued)

Equation	Name	Description	Formula	Interpretation
(10)	***U^X*** *($t\ km^{-2}yr^{-1}$)*	Plant Uptake Rate of Element X	$GrowthRate_{Plant} \times [X]_{plant}$	Plant uptake flux of element *X* during plant growth.
(11)	***L^X*** *($t\ km^{-2}yr^{-1}$)*	Litterfall Rate of Element X	$LitterfallRate_{Plant} \times [X]_{plant}$	Litterfall flux of element *X*; sum of leaf, trunk and root litter flux of *X* from trees to topsoil through litterfall.
(12)	***Rec^X*** *dimensionless*	Biomass Recycling Number of Element X	$\frac{L^X}{W^X_{regolith}+Dep^X_{wet}+Dep^X_{dry}}\ or\ \frac{U^X}{W^X_{regolith}+Dep^X_{wet}+Dep^X_{dry}}$	Number of cycles of an element *X* through biomass after dissolution from regolith or, if present, wet and the dissolved fraction of dry atmospheric deposition before loss into drainage or erosion; calculated using litterfall or biomass production. Eq 12* is valid if atmospheric deposition is much smaller than $W^X_{regolith}$
(12*)			$\frac{L^X}{W^X_{regolith}}\ or\ \frac{U^X}{W^X_{regolith}}$	
(13)	***DEE^X*** *dimensionless*	Dissolved Export Efficiency of Element X	$\frac{\mathrm{W^X_{river}}}{\mathrm{W^X_{regolith}}}$	Ratio of flux of element *X* found in dissolved river export relative to the flux released by weathering in regolith. If present, wet and the dissolved fraction of dry atmospheric deposition terms have to be added to the denominator (as in eq. (12)).
(14)	***DEE^X_{Na}*** *dimensionless*	Na-Normalised Dissolved Export Efficiency of Element X	$\frac{W^X_{river}/W^{Na}_{river}}{(W^X_{regolith}+Dep^X_{wet}+Dep^X_{dry})/(W^{Na}_{regolith}+Dep^{Na}_{wet}+Dep^{Na}_{dry})}$	Ratio of flux of element *X* found in dissolved river export relative to the flux released by weathering in regolith. Ratio is normalised by the conservative element Na so that the ratio is independent of rate estimates. Eq 14* is valid if atmospheric deposition is much smaller than $W^X_{regolith}$.
(14*)			$\frac{\frac{W^X_{river}}{W^{Na}_{river}}}{\frac{W^X_{regolith}}{W^{Na}_{regolith}}} = \frac{(\frac{[X]_{river}}{[Na]_{river}})\ /\ (\frac{[X]_{rock}}{[Na]_{rock}})}{\frac{(\tau^X_{Xi})}{(\tau^{Na}_{Xi})}}$	

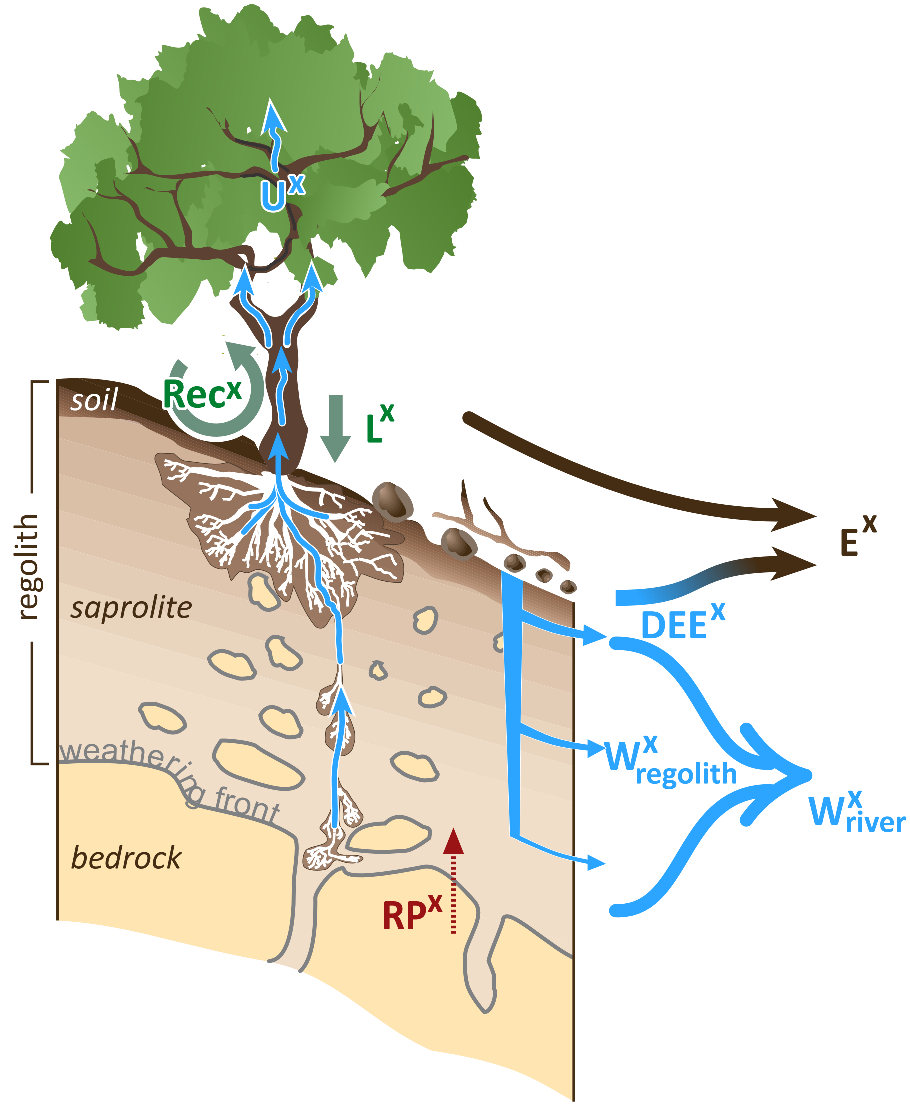

Fig. 2. Schematic representation of the parameters used in this paper to quantify the partitioning of a given element X between compartments, namely the regolith production rate (RP^X), elemental erosion rate (E^X), regolith weathering rate ($W^X_{regolith}$), river weathering rate (W^X_{river}), plant uptake rate (U^X), litterfall rate (L^X), biomass recycling number (Rec^X), and dissolved export efficiency (DEE^X)). Note that the ratio of W^X_{river} to $W^X_{regolith}$ denotes the "missing" dissolved export flux of element X not found in rivers after regolith production, as quantified by the dissolved export efficiency $DEE^X < 1$.

The element-specific regolith production rate RP^X is calculated by multiplying RP with $[X]_{rock}$, the concentration of the element X in bedrock:

$$RP^X = RP \cdot [X]_{rock} \tag{3}$$

The chemical depletion fraction CDF is the fractional dissolved mass loss of all elements together (primary mineral dissolution minus secondary precipitate formation) relative to unweathered, completely fresh bedrock, calculated from measurements of a chemically immobile element (here Zr is used that is contained in the refractory mineral zircon (Riebe and others, 2003)). The ability of *CDF* to accurately represent element depletion depends on the homogeneity of bedrock and the ability to sample unweathered, representative bedrock. A *CDF* of 0 means no loss, and a *CDF* of 0.5 means 50 % mass loss, which is also roughly the maximum mass loss attainable for felsic rock (Dixon and von Blanckenburg, 2012) since quartz is essentially inert during weathering and other minerals weather to produce insoluble Al-, Si-, and Fe-bearing secondary clay and oxide phases.

$$CDF = 1 - \frac{[Xi]_{unweathered\ bedrock}}{[Xi]_{weathered\ regolith}} \tag{4}$$

As an immobile element *Xi*, we use Zr in this study. The element-specific depletion fraction (also called the "mass-transfer coefficient"; Chadwick and others, 1990) τ_{Xi}^{X} is the fractional mass loss of element *X* relative to unweathered bedrock, determined by measuring the concentrations of both *X* and the chemically immobile Zr in bedrock and regolith. A τ_{Xi}^{X} of 0 means no net element loss, and a τ_{Xi}^{X} of −0.5 means 50 % element loss:

$$\tau_{Zr}^{X} = \frac{[Xi]_{unweathered\ bedrock}}{[Xi]_{weathered\ regolith}} \times \frac{[X]_{weathered\ regolith}}{[X]_{unweathered\ bedrock}} - 1 \tag{5}$$

Note that by convention, τ^{X} is opposite in sign to *CDF* values. In this publication, we refer to τ_{Zr}^{X}, reflecting the use of Zr for *Xi*. The chemical weathering rate of regolith $W_{regolith}$ is the chemical denudation by dissolved mass loss. $W_{regolith}$ integrates over the time over which regolith is being weathered (regolith thickness divided by *RP*), typically 10^3 and 10^5 years:

$$W_{regolith} = RP \times (CDF) \tag{6}$$

We can compare the longer-term $W_{regolith}$ with the shorter-term, catchment-integrated estimate W_{river}, which is the chemical weathering rate calculated from the river runoff [$m^3\ yr^{-1}$ or $L\ yr^{-1}$], the sum of all concentrations $[X]_{diss,i}$ of dissolved, rock-derived cation (in oxide equivalents) and SiO_2 concentration in river runoff (Bouchez and Gaillardet, 2014) measured at time *i*, and the catchment area *A*. A single measurement of river dissolved composition typically integrates over the residence time of water in the catchment, that ranges from weeks to years depending on the catchment and the sampling time, but this integration time is extended (typically years) when repeated sampling campaigns are performed. In the case of multiple sources of solutes (for example, silicate rock, carbonate rock, atmospheric deposition), different components of $[X]_{diss,i}$ have to be distinguished using an "end member mixing analysis" (EMMA, see below). Assuming that one measurement per day is available, an annual estimate of W_{river} can be obtained:

$$\frac{W_{river} = \sum_{i=1}^{365} [Cations + SiO_2]_{river_i} \times Q_i}{A} \tag{7}$$

The element-specific chemical weathering rate of regolith $W^X_{regolith}$ is calculated from RP^X (eq 3) and $-\tau^X_{Zr}$.

$$W^X_{regolith} = RP^X \times \left(-\tau^X_{Zr}\right) \tag{8}$$

As with equation (8) we can calculate the element-specific river weathering rate W^X_{river}:

$$W^X_{river} = \sum_{i=1}^{365} \frac{[X]_{river_i} \times Q_i}{A} \tag{9}$$

In practice, daily coupled measurements of water chemistry and discharge are not always available, and we thus use the product of annual runoff and an unweighted mean solute concentration to derive W_{river} and W^X_{river}. Runoff estimates and sources for the three sites are given below and in Data Table C1. Note that the weathering parameters as calculated in equations, (4), (6), and (8) are strictly only valid if atmospheric mass fluxes into the regolith, including dust and rainwater inputs, do not affect $Zr_{weathered\ regolith}$ or $D_{regolith}$, otherwise modified expressions that take dust input into account are required (Ferrier and others, 2011). Although all our sites have minor atmospheric inputs, when necessary, we circumvent this correction by using chemical depletion parameters measured in the uppermost saprolite sample, which is not affected by dust input. Thus, all our weathering fluxes exclusively pertain to the mass fluxes arising from the conversion of bedrock to regolith. River dissolved loads (eq 9) however are partially derived from wet and dry atmospheric inputs, and as explained below plant mineral nutrient uptake does not discriminate between for example, dust and regolith sourced nutrients. The contributions of dry and wet atmospheric depositional fluxes, termed Dep^X_{dry} and Dep^X_{wet} respectively, are added to the weathering inputs (eqs 12 and 13 below), after their quantification which results from an end member mixing analysis of river water chemistry (see Data Table C4, Data Publication Part 2).

Ecosystem Metrics

We estimate the uptake of nutritive elements into an entire ecosystem, called U, from the plant biomass growth rate $GrowthRate_{Plant}$. In the absence of adequate monitoring of this parameter at our sites, $GrowthRate_{Plant}$ is obtained from a globally gridded, machine-learning convolution of remote-sensing imagery with eddy covariance GPP (Gross Primary Production) data from the FLUXNET network (Jung and others, 2019). Biomass production is estimated by assuming that NPP(C) $\approx$ GPP(C)/2, where NPP is the Net Primary Production (Chapin and others, 2011), and further that dry biomass consists of 50 wt% carbon, such that $GrowthRate_{Plant} \sim$ GPP(C). To obtain the element-specific uptake rate U^X, $GrowthRate_{Plant}$ is multiplied with the bulk concentration of X in the plants $[X]_{plant}$. Where possible, bulk elements concentrations should be estimated based on concentrations in different organs of plants weighted by scaling relationships (Uhlig and others, 2017; Uhlig and von Blanckenburg, 2019):

$$U^X = GrowthRate_{Plant} \times [X]_{plant} \tag{10}$$

Given the systematic uncertainties associated with U^X, an alternative means to estimate elemental fluxes through plants is to rely on the return flux through litterfall L^X, the product of litterfall rates and the bulk concentration of element X in the plants $[X]_{plant}$ where Litterfall L is the sum of leaf, trunk and root litter flux. L^X is likely a minimum estimate compared to elemental uptake, because L^X does not include stemflow or resorption during senescence. In other words, U^X from NPP provides an estimate of gross elemental uptake, whereas L^X from litterfall provides an estimate of net uptake.

$$L^X = LitterfallRate_{Plant} \times [X]_{plant} \tag{11}$$

A parameter we developed within the context of the erodosequence study is the ecosystem recycling factor Rec^X (Uhlig and others, 2017; Schuessler and others, 2018; Uhlig and von Blanckenburg, 2019). Rec^X is obtained by normalising either L^X or U^X by the elemental weathering rate $W^X_{regolith}$ plus solute input fluxes from atmospheric deposition Dep^X_{wet} and Dep^X_{dry}. Rec^X is a metric that quantifies the number of uptake and release cycles of an element by ecosystem vegetation after its release by chemical weathering of parent bedrock or atmospheric deposition. Rec^X is equivalent to the inverse of the fraction of "new" nutrient as defined by Cleveland and others (2013) that quantifies the proportion of fresh weathering-derived nutrients that is taken up by plants. We note that Rec^X estimates the nutrient uptake relative to the release from the entire weathering zone. Not all of the weathering release flux will be available to ecosystems if some is immediately lost to groundwater before uptake; as a consequence Rec^X represents a minimum estimate for recycling within the upper soil layer. If wet atmospheric Dep^X_{wet} (rain) deposition, or dry Dep^X_{dry} (dust) input - some of which is subsequently dissolved – is significant, these fluxes need to be added to the denominator. They are quantified using results from the river dissolved end member mixing analysis (see below).

$$Rec^X = \frac{L^X}{W^X_{regolith} + Dep^X_{wet} + Dep^X_{dry}} \; or \; \frac{U^X}{W^X_{regolith} + Dep^X_{wet} + Dep^X_{dry}} \tag{12}$$

In the case that $Dep^X << W^X_{regolith}$ equation (12) simplifies to

$$Rec^X = \frac{L^X}{W^X_{regolith}} \text{ or } \frac{U^X}{W^X_{regolith}} \tag{12*}$$

Another parameter developed within the erodosequence study is the elemental "Dissolved Export Efficiency" DEE^X, which compares the release of an element X by weathering in regolith (including, if present, wet atmospheric deposition and the dissolved fraction of dust flux) with its dissolved export in the fluvial system. If $DEE^X = 1$, element loss from the regolith and solute export from the catchment are the same. If DEE^X exceeds 1, either the system is not at steady state or the catchment receives net atmospheric input that is found in the river but not in regolith beneath soil. In this case the river dissolved load should be corrected for these additional inputs. If $DEE^X < 1$ either the system is not at steady state, or a fraction of element X is withdrawn from the dissolved pool after release by weathering and before export into the river (we evaluate other factors like unrepresentative parent bedrock below). Below, we argue that plant uptake of X followed by export of plant debris is a likely explanation for cases where $DEE^X < 1$, in which case DEE^X is a powerful metric for the partitioning of a nutritive element between the dissolved flux and plants. The same compartment separation would also fractionate metal(loid) stable isotopes.

$$DEE^X = \frac{W^X_{river}}{\mathrm{W}^X_{regolith} + Dep^X_{wet} + Dep^X_{dry}} \tag{13}$$

In the case that $Dep^X << W^X_{regolith}$ equation (12) simplifies to:

$$DEE^X = \frac{W^X_{river}}{W^X_{regolith}} \tag{13*}$$

An alternative version of DEE^X is obtained by normalizing both the weathering release and the river discharge by Na, yielding DEE^X_{Na}. Sodium is considered a "conservative" element in the sense that it is neither a nutrient nor a major clay-forming element. The advantage of DEE^X_{Na} is that unlike for DEE^X, river runoff does not need to be known. Potential non-steady state behavior likely affects DEE^X due to the different integration time scales of $W^X_{regolith}$ and W^X_{river}, but is mitigated in $\mathrm{DE}E^X_{Na}$ since Na concentrations are affected by changes in flux proportional to the element of interest, such that temporal variations are assumed to cancel out (see below for a discussion of this assumption).

$$DEE^X_{Na} = \frac{W^X_{river} / W^{Na}_{river}}{(W^X_{regolith} + Dep^X_{wet} + Dep^X_{dry}) / (W^{Na}_{regolith} + Dep^{Na}_{wet} + Dep^{Na}_{dry})} \tag{14}$$

In the case that $Dep^X << W^X_{regolith}$ equation (12) simplifies to:

$$DEE^X_{Na} = \frac{\frac{W^X_{river}}{W^{Na}_{river}}}{\frac{W^X_{regolith}}{W^{Na}_{regolith}}} = \frac{\left(\frac{[X]_{river}}{[Na]_{river}}\right) / \left(\frac{[X]_{rock}}{[Na]_{rock}}\right)}{\frac{\left(\tau^X_{Zr}\right)}{\left(\tau^{Na}_{Zr}\right)}} \tag{14*}$$

Unlike equation (14) that requires estimates of absolute fluxes W^X and Dep^X, DEE^X_{Na}calculated with the simplified equation (14*) requires only elemental ratios, and so is not subject to uncertainties on for example, river discharge or dust deposition rates, parameters that may be difficult to precisely constrain. Throughout, all uncertainties on measured concentrations and fluxes are fully propagated into the derived metrics (U^X, Rec^X, DEE^X), including the uncertainties resulting from the EMMA analysis where appropriate (Data Table C5).

FIELD SITES

The location of the field sites is shown in figures 3A, B, and C, and their main characteristics are summarized in table 2.

Swiss Central Alps

The sampling site is located in the Swiss Central Alps on a soil-mantled ridgetop of the Honeggerhorn at 2565 m altitude on the northern slope of the upper Rhone

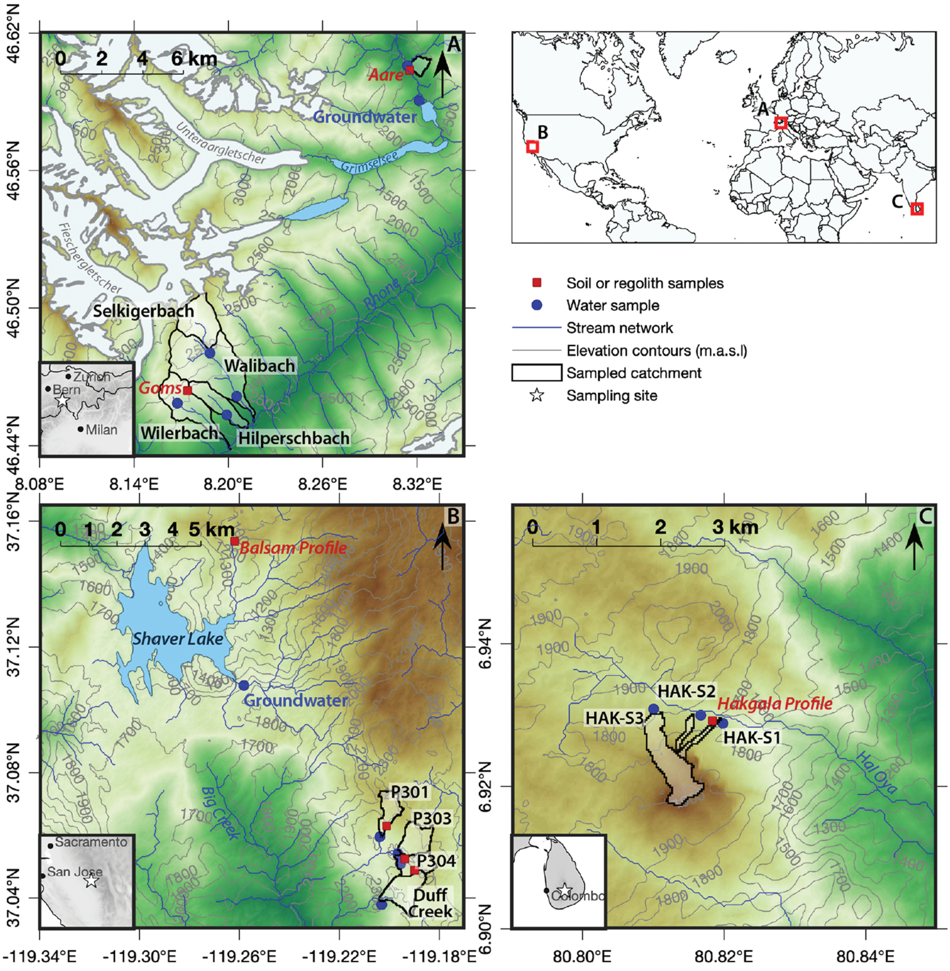

Fig. 3. Locations of the three study sites defining the erodosequence presented in this study. (A) the Alps sites showing the upper Rhone valley; (B) Sierra Nevada sites showing Providence Creek and the Balsam profile; (C) Sri Lankan Highlands showing the Hakgala site. Regolith profile locations are shown as white star. Produced with http://www.geomapapp.org using the Global Multi-Resolution Topography (GMRT). The delineation of Swiss glaciers is from Fischer and others (2014).

valley (Goms). A nearby meteorological station at Ulrichen (elevation = 1346 masl) records 3.1 °C and 1137 mm annual averages for temperature and precipitation, respectively. Bedrock is the Aare Massif that mainly comprises foliated gneiss (major mineral components: 23 % quartz, 53 % plagioclase, 17 % orthoclase, 4 % biotite and 3 % muscovite) and granite in the upper valley sections (major mineral components: 34 % quartz, 35 % plagioclase, 27 % orthoclase, 4 % biotite). The sites were glaciated up to 15 kyr ago. Successive glaciations, culminating in the last glacial maximum (LGM, *ca.* 21 kyr) carved the > 1500-m deep Rhone Valley, generating a landscape characterized by smooth, glacially scoured landscapes that are largely devoid of glacial till. At low elevations in the main Rhone Valley, thin glacial deposits are plastered to the hillsides. The glacially eroded landscapes are generally steeper than the surrounding, non-glaciated hillslopes and ridges with mean basin slopes of > 30 degrees. At this sampling site soils are immature and minimally developed, with thicknesses less

TABLE 2

Summary of study site characteristics

	MAT	**MAP**	**Landscape Scale Denudation**	**Regolith thickness**	**RP**	±	**Regolith residence time**	**CDF**	±	**W$_{\mathrm{regolith}}$**	±	**E**	±	**W$_{\mathrm{river}}$**	**W$_{\mathrm{river}}$**	±	**Dust flux**	**Runoff**	±	**Biomass Production**	±
	(°C)	(mm)	(t km^{-2} yr^{-1})	(cm)	(t km^{-2} yr^{-1})		(kyr)	(dimension-less)		All fluxes (t km^{-2} yr^{-1})				Total	Silicate		(t km^{-2} yr^{-1})	(M yr^{-1})		(t km^{-2} yr^{-1})	
Alps	3	1140	220-5500	35	103	40	10	0.31	0.21	32	25	71	55	89.3	42.9		0.6 to 6	1.51	0.3	779	9
Sierra Nevada	7.8	750 - 2000	70-200	700	221	56	86	0.36	0.09	80	28	141	50	*Mean*	24	11	6.6	0.40	0.09	1348	27
														P301	21	1.6					
														P303	14	1.0					
														P304	40	3.8					
														D102	20	1.3					
Sri Lanka	16	2013	50-100	1000	42	6.4	600	0.50	0.15	20.8	7.0	20.8	7.0	38	18		5 to 10	1.14	0.35	2957	53

See Supplementary Data Tables C1 and C2 for data sources and calculations.

than 50 cm at the ridgetop site. In general, soils in this region of the Alps are mostly Podzols that mantle slopes between 1800 to 2600 m elevation (Egli and others, 2008). According to visual inspection, only thin saprolite is visible below the soil. While clay mineralogy was not determined for these soils, clay coatings and partially dissolved plagioclase are evident in SEM imagery (Norton and von Blanckenburg, 2010). A more detailed description of the sampling site can be found in Norton and von Blanckenburg (2010), Norton and others (2010).

The landscape-scale denudation rate measured from cosmogenic nuclides (^{10}Be) in river sediment is 220 to 5500 t km^{-2} yr^{-1}, and strongly depends on average hillslope (Norton and others, 2010). The average denudation rate derived from cosmogenic ^{10}Be measured on soils of the sampling site are 38.4 mm kyr^{-1} (103 ± 40 t km^{-2} yr^{-1}) (Data Table C2). Norton and von Blanckenburg (2010) determined a mean fraction of mass loss by chemical weathering (*CDF*) of 0.31.

The vegetation cover at the ridge top site is mainly grass. Annual biomass production from 1980 to 2013 derived from an interpretation of satellite imagery guided by FLUXNET GPP data at 0.5° resolution (Jung and others, 2011) was 779 ± 18 t km^{-2} yr^{-1}. We estimate an annual runoff of 1.51 ± 0.30 (m yr^{-1}, ±1sd) from the Swiss Bundesamt für Umwelt BAFU monitoring of Wilberbach and Walibach catchments (see fig. 3).

We sampled five soil depth profiles (B1, B2, B4, B5, B6, Data Table A1) and thin saprolite from their C horizon of up to 30 cm thickness on the south-facing slope of the Upper Rhone Valley ("Goms" site). Soil profile details are shown in figure 4A. Further soil analyses and bedrock composition were compiled from Norton and von Blanckenburg (2010) (Data Table A1). We sampled water from streams draining the hillslope: the Selkligerbach, Walibach, Wilerbach, and Hilpersbach; and soil water from our profiles (Data Table A2). A secondary site located in the Upper Rhine Valley next to the Grimsel Pass ("Aare" site) was sampled for grass, the only relevant plant species at higher elevations at the Goms site (Data Table A3) and groundwater in the Grimsel underground rock laboratory. We note that the bedrock at the Aare site is granitic and differs from the Goms gneiss. In the Data Tables we also report rock, soil, and water compositional data from the Aare site (underlain by the Aare granite, glaciated up to 11 kyr ago), though we do not evaluate these data in the current paper (Data Tables A1, 2, 3).

Sierra Nevada

The soil profiles are located in the Kings River Experimental Watersheds ("KREW") in the southern Sierra Nevada (USA) mountain range, part of the Southern Sierra Critical Zone Observatory (SSCZO, O'Geen and others, 2018). Soils were sampled within catchments located at the Providence Creek (PC) site. Associated PC catchments (P301, P303, P304) range in size between 0.49 to 1.32 km^2 at an elevation between 1479 to 2113 m, and have annual precipitation of between 750 to 2000 mm (Hunsaker and Neary, 2012). Mean annual air temperature is 7.8 °C (Liu and others, 2013). A separate regolith profile exposed in a roadcut located NE of Shaver Lake along the Tollhouse Road (California State Route 168) was sampled. Detailed descriptions of the sampling sites can be found elsewhere (Bales and others, 2011; Hunsaker and Neary, 2012; Liu and others, 2013; Uhlig and others, 2017).

The soils in the PC catchments are well-drained and mainly underlain by tertiary granitic rocks. The bedrock at both PC catchments and the Shaver Lake locations is dominated by the 'Dinkey Creek Granodiorite', a medium-grained, equigranular, strongly foliated biotite-hornblende granodiorite/tonalite with sphene, plagioclase, and opaque minerals, which contains abundant disc-shaped mafic inclusions

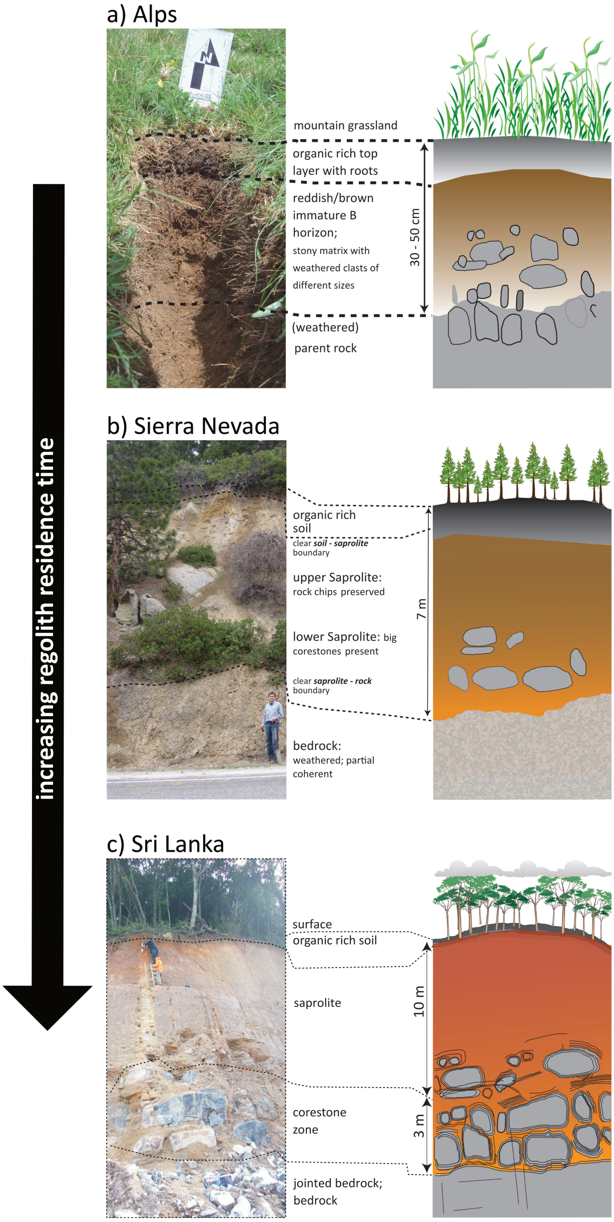

Fig. 4. Photographs of regolith profiles (left) and profile schematics (right) of the three study sites. (A) Alps site: typical example of a soil profile at the ridge top (Honeggerhorn) in the upper Rhone Valley. (B) The sampled saprolite profile ("Balsam-Profile") to the north east of Shaver Lake, Southern Sierra Nevada, California, USA. Isotope geochemist for scale. (C) Sri Lankan Highlands, sampled regolith profile in the vicinity of Hakgala Botanical Garden, Nuwara Eliya district.

(Bateman and Wones, 1972). The well-developed soils at the PC sites are dominated by the "Shaver soil series", a coarse-loamy, mixed mesic Humic Dystroxerept. This soil series has a balanced supply of moisture, is free of carbonates and has an organic-rich surface soil horizon. Dahlgren and others(1997) described the clay mineralogy of these soil types to be dominated by hydroxyl-Al interlayered vermiculite and gibbsite.

The weathering of plagioclase under these environmental conditions results in the formation of kaolinite.

The landscape-scale denudation rate measured from cosmogenic nuclides (^{10}Be) in river sediment is 70 to 200 t km^{-2} yr^{-1} (Callahan and others, 2019) and 102 to 153 t km^{-2} yr^{-1} (Hahm and others, 2014) as recalculated by Arvin and others (2017). The average denudation rate derived from cosmogenic ^{10}Be concentrations in soil quartz at the sampling site is 220 ± 56 t km^{-2} yr^{-1} (Data Table C2, after Dixon and others,2009b) corresponding to 81.5 ± 22 mm kyr^{-1}.

The vegetation cover mainly consists of a Sierran Mixed Conifer Forest. Tree species are dominated by *Pinus ponderosa* (Ponderosa Pine), *Pinus jeffreyi* (Jeffrey Pine), *Pinus lambertiana* (Sugar Pine), *Calocedrus decurrens* (Incense-Cedar), *Abies concolor* (White Fir). Understory shrubs include *Chamaebatia foliolosa* (Mountain Misery), *Ceanothus cordulatus* (Mountain Whitethorn), *Arctostaphylos manzanita* (Manzanita), and the occasional *Cannabis sativa.* Mean annual biomass production derived from globally upscaled FLUXNET at 0.5° resolution eddy covariance GPP data (Jung and others, 2011, 2019) for the years 1980 to 2013 was 1348 ± 54 t km^{-2} yr^{-1}. We estimate an annual runoff of 0.4±0.09 (m yr^{-1}, ±1sd) from the KREW stream monitoring program.

We sampled bulk soil and saprolite from the P301 soil profile to 100 cm depth and the soil-saprolite Shaver Lake profile (named the "Balsam" profile) that consists of at least 600 cm of altered rock (fig. 4B, Data Table SN 1). As bedrock was not encountered at the base of either profile, we collected bedrock samples exposed in the respective catchments. Because these may be biased in composition due to local heterogeneity we complemented our own bedrock data with a compilation from Hahm and others(2014) and Riebe and Granger(2013) (Data Table SN 1) to recalculate *CDF* using a common and presumably representative bedrock Zr concentration. Creek water of the individual Providence Creek sites (P301, P303, P304, D102, Data Table SN2), soil water (P301, P303, P304), and groundwater (P301 well 1 and well 2) were sampled (Data Table SN2). We also sampled the main vegetation types in the forest (Data Table SN3).

Sri Lanka

The study site is located in the Central Highlands of Sri Lanka. The sampling location is a regolith profile located at 1753 m altitude that is exposed along the road from Nuwaraeliya to Welimada, close to the Hakgala Botanical garden (fig. 3C). The profile's mineralogy and geochemistry, including soil water and surface water chemistry is described in detail in Hewawasam and others(2013) and the mineralogical transformations in Behrens and others(2015). Landscape-scale erosion and denudation rates from both cosmogenic nuclides and river loads are given in Hewawasam and others(2003) and von Blanckenburg and others(2004). The mean annual temperature ranges from 7.8 °C to 23.4 °C. The forest receives both north-east and south-west monsoons with annual precipitation ranging from 1237 mm to 2269 mm. The regolith at the sampling site is located on a hillslope and developed from the underlying charnockite bedrock (a high-grade metamorphic rock consisting of K-feldspar (32 %), quartz (30 %) and plagioclase (25 %) as major mineral components and biotite (7 %) and orthopyroxene (4 %) as minor mineral components). The profile has a depth of >10 m (fig. 4C) with a red-yellow lateric soil layer in the uppermost 60 cm of the profile. Between the base of the soil layer and 6 m depth the saprolite is reddish and highly weathered. The lower part of the saprolite is banded with thin white and yellow layers and contains small rounded charnockite core stones ranging in diameter from a few cm to 50 cm. Below a depth of 8 m, massive charnockite corestones were found, affected by incipient weathering reactions.

The landscape-scale denudation rate measured from cosmogenic nuclides (^{10}Be) in river sediment is 50 to 100 t km^{-2} yr^{-1} (von Blanckenburg and others, 2004). The average denudation rate derived from cosmogenic ^{10}Be measured on soils in close vicinity to the sampled regolith profile is 42 ± 6 t km^{-2} yr^{-1} (Data Table C2, after Hewawasam and others(2013), corrected for dissolved loss in the saprolite below the cosmogenic attenuation depth, corresponding to 16.0 ± 2.5 mm kyr^{-1}.

The upslope catchment of the regolith profile is steep with slopes of 10° to 25° and completely covered by a natural forest. The vegetation cover consists of a tropical forest with a thick canopy up to a height of 20 m and hosts at least 97 tree species, of which 62 are endemic. The most common tree species are: *Allophylus varians* (Sapindaceae), *Cinnamonum ovalifolium* (Laureacea), *Eugenia mabaeoides* (Myrtaceae), *Memecylon parvifolium* (Melastromataceae), *Michelia nilagirica* (Magnoliaceae), *Neolitsea fuscata* (Lauraceae), *Psychotria bisulcata* (Rubiaceae), *Semecarpus coriacea* (Anacardiaceae), *Symplocos loha* (Symplocaceae), *Syzygium revolutum* (Myrtaceae), and *Syzygium rotundifolium* (Myrtaceae) (Weerakkody and Parkinson, 2006a). Mean annual biomass production derived from globally upscaled FLUXNET eddy covariance data at 0.5° resolution for 1980-2013 (Jung and others, 2019) was 2957 ± 106 t km^{-2} yr^{-1}. We estimate a runoff of 1.14 ± 0.35 (m yr^{-1}, ±1sd) from reported gauging of the smaller rivers in Hewawasam and others (2013) and von Blanckenburg and others (2004), excluding the larger Uma Oya catchment.

We collected bulk soil, saprolite and bedrock samples of the regolith profile at Hakgala (Data Table SL1). Soil water and river water of three creeks (in the vicinity of the regolith profile within a distance of 300 m) draining undisturbed, first-order forested catchments were also sampled (Data Table SL2). We also sampled the main vegetation types present in the vicinity of the regolith profile (Data Table SL3).

METHODS

Rock and Regolith Chemical Composition by X-Ray Fluorescence

Total element concentrations of soil, saprolite and rock were analyzed on bulk samples using X-ray fluorescence spectrometry (XRF, Panalytical Axios Advanced, German Research Center for Geosciences (GFZ Potsdam), section Inorganic and Isotope Geochemistry). All silicate sample types (bedrock, saprolite and soil) were oven-dried at 60 °C, and representative aliquots of the samples were pulverized in an agate mill to < 63 μm grain size. Sample powders were weighed before and after combusting for 5 h at 600 °C to determine the loss on ignition (LOI). The remaining powder was then used for alkali fusion using Li-metaborate to produce glass beads that were analyzed for bulk chemical composition. Relative analytical uncertainties on the reported XRF data are about 5 % for major elements and about 10 % on trace elements.

Reported major element composition and Zr concentration of bulk samples were corrected for loss on ignition LOI. For calculation of *CDF* and τ^X values we use the LOI-corrected concentrations to rescale all reported element concentration data to 100 %:

$$[X]_{solid,corrected} = \frac{([X]_{solid,uncorrected} \cdot 100)}{(100 - LOI)} \qquad (15)$$

Mineralogical Characterization by X-Ray Diffraction

Powder X-ray diffraction analyses (Siemens D5000, Cu-Kα radiation, resolution 0.01° 2 Theta, <63 μm fraction) were performed at GFZ Potsdam for mineral identification on selected sieved samples. For peak maxima identification, we used the software MATCH! 3.3.

Anion Concentrations by Ion Chromatography

Water samples were taken into 5 ml glass vials and sealed gas free. Major anion (Cl^-, NO_3^-, PO_4^- SO_4^-) concentrations were determined using a Thermo Scientific Dionex Ion Chromatograph DX-120 or a Thermo Scientific ICS 1100 with the column Ion Pac AS 9-HC at section 3.1, GFZ Potsdam. Sample, eluent, and standard preparation for both instruments and measurements was similar. We always used a freshly prepared 9 mmol/l Na_2CO_3 solution as eluent. Calibration standard solutions were prepared daily from Merck 1000 mg/l standard solutions. For data evaluation, we used total peak integration of the analyzed anions to determine their concentrations.

Alkalinity by Photometry

Alkalinity was measured in the field using the photometer system AL400 from Aqualytic on 10 ml of sampled water and an ALKA-M-PHOTOMETER tablet. For some samples, total alkalinity was determined in the laboratory by titration with 0.01 M HCl (Titrisol Merck) to a pH of 4.3 as measured by a pH meter.

Major Element Concentration of Water Samples by ICP-OES

ICP-OES measurements of major element concentrations were performed in the Helmholtz Laboratory for the Geochemistry of the Earth Surface "HELGES" (von Blanckenburg and others, 2016) at GFZ Potsdam, using an axial ICP-OES (Varian 720-ES). Details on the instrumental setup and the analytical method are given in (Schuessler and others, 2016) and are briefly summarized here. Water samples were filtered (< 0.2 µm) and acidified to pH ~ 2 with Suprapur grade HNO_3 in the field and stored at 4 °C in acid cleaned PE bottles. Before concentration analysis, samples were diluted in 0.3 M HNO_3 containing 1 mg/g Cs. Matrix matched calibration standards were made from a mixture of single element ICP standards (Merck CertiPur, traceable to NIST reference materials). Procedural blanks were below 0.1 % of analyte solutions and are considered to be negligible. Relative analytical uncertainties for data measured during this study are estimated to be between 5 and 10 %.

Trace Element Concentration of Water Samples by ICP-MS

Trace element concentrations were measured in the "HELGES" Laboratory at GFZ Potsdam using a high-resolution inductively coupled plasma mass spectrometer (HR-ICP-MS; Element 2, Thermo Fisher Scientific). Li, Rb, Sr, Y, Ba were measured in low mass resolution and Al, P, V, Cr, Ni, Zn in medium mass resolution mode. In both modes Rh was used as internal standard. All samples and calibration standards were diluted in sub-boiled 0.3 M HNO_3. Tests prior to the measurements showed that matrix-matching of the calibration solutions is not needed, as no significant matrix effects are observed in the presence of major elements in the concentration range expected in river and soil water. Relative analytical uncertainties for data measured during this study are estimated to be between 10 and 20 % for most elements, verified by the same method used for ICP-OES analysis (see table C6 for individual quality control results). The certified reference standard (SLRS-6, National Research Council of Canada), three standard reference samples (M-212, T-213, and T-227, U.S. Geological Survey), as well as one in-house standard (GFZ-RW 1e, prepared from single element standards, traceable to NIST) resembling a typical river water matrix containing the major constituents Ca, Mg, K, Si, Na, S, P and the trace constituents Cu, Ni, Zn, Ti and Fe, were analyzed together with unknown samples. The uncertainty of the measurements is given in tables A2, SN2, and SL2 as one standard deviation, for the reference standards in table C6 it was estimated from repeated measurements over multiple sessions. For every measurement session the limits of quantification (LOQ) were calculated based on the ten-fold standard deviation above the blank.

Sr and Nd Isotope Ratios by MC-ICP-MS

In order to identify sources of material, Sr isotope analyses of rock, regolith, water and plant samples from all three sites were performed in the HELGES laboratory following the method described in Hewawasam and others (2013). In brief summary for all water and solid samples (digested using concentrated acid mixtures of HF, HNO_3 and HCl, see for example, Hewawasam and others, 2013), Sr was separated from the sample matrix by extraction chromatography (using an Sr-SPEC resin, Eichrom), and Sr isotope ratios were measured by multicollector ICP-MS (Neptune Plus, Thermo Fisher Scientific) using an APEX-Q (ESI) desolvation system as the sample introduction system. Kr interferences on masses 84 and 86 and a Rb interference on mass 87 were corrected for using ^{83}Kr and ^{85}Rb signals along with Kr and Rb isotope ratios as measured at the beginning of the sequence. Natural and instrumental mass fractionation on the $^{87}Sr/^{86}Sr$ ratio was corrected for using an exponential law, the measured $^{88}Sr/^{86}Sr$ ratio and a normalizing natural abundance ratio, taken as 8.3752. Each sample was measured three to six times during a session. The associated double standard deviation (2 S.D.) was in the range 1 to 5 x 10^{-5} on the $^{87}Sr/^{86}Sr$ ratio, equivalent to that estimated on a longer-term basis using the Sr carbonate reference material NIST SRM 987, which was frequently measured to check the accuracy of the method.

To identify possible dust additions at the Sierra Nevada CZO, Nd isotope analyses were performed for soil and saprolite samples from this site only at the analytical platform PARI of IPGP by MC-ICP-MS (Neptune Plus, Thermo Fisher Scientific) using an APEX-IR (ESI) desolvation system as the sample introduction system with N_2 addition and X-cones. Chromatographic separation of Nd prior to analysis was achieved using columns packed with the TRU-SPEC and Ln-SPEC resins (Eichrom). Natural and instrumental mass fractionation on the $^{143}Nd/^{144}Nd$ ratio was corrected for using an exponential law, the measured $^{146}Nd/^{144}Nd$ ratio and a normalizing natural abundance ratio, taken as 0.7218. Nd isotope ratios are reported as ε_{Nd} values, with $^{143}Nd/^{144}Nd$ ratios normalized to the ratio of the CHUR (0.512638).

Element Concentrations in Plant Material

Plant samples were digested in the HELGES laboratory using a microwave-assisted digestion system (MLS Start), or in PFA vials on a hotplate, in a concentrated acid mixture of HNO_3/H_2O_2 followed by a treatment with concentrated HF to remove biogenic silica. Alkali fusion was performed on separate sample aliquots to obtain concentrations of Si, which is otherwise volatilized by the HF. After digestion samples were diluted in 0.3 M HNO_3 containing 1 mg/g Cs (see detailed method description for ICP-OES analysis above) and analyzed by ICP-OES (Varian 720-ES). Relative uncertainties were determined by repeated analyses of standard reference materials (NIST SRM1515, ERM-CD281) and are better than 20 % for all elements with the exception of Fe, Na and Zn (relative uncertainty <30 %).

Stream Solute Corrections and End Member Mixing Analysis (EMMA)

Surface and subsurface waters combine solutes derived from a variety of sources, including wet (rain) and dry (dust) atmospheric deposition, anthropogenic inputs (for example, fertilizers), and weathering solutes of various mineral types (for

Table 3

Fractional contributions to dissolved elements in stream water deduced from the inversion of mixing equations

Alps	**K**	±	**Na**	±	**Sr**	±	**Ca**	±	**Mg**	±
Silicate	0.98	0.02	0.89	0.08	0.18	0.17	0.49	0.25	0.62	0.30
Carbonate	0.00	0.00	0.00	0.00	0.80	0.18	0.51	0.25	0.37	0.30
Rain	0.02	0.03	0.11	0.08	0.01	0.02	0.00	0.00	0.01	0.01

Sierra Nevada	**K**	±	**Na**	±	**Sr**	±	**Ca**	±	**Mg**	±
Silicate	0.92	0.09	0.87	0.16	1.00	0.01	1.00	0.00	0.99	0.02
Carbonate	0.00	0.00	0.00	0.00	0.00	0.00	0.00	0.00	0.00	0.00
Rain	0.08	0.09	0.13	0.16	0.00	0.01	0.00	0.00	0.01	0.02

Sri Lanka	**K**	±	**Na**	±	**Sr**	±	**Ca**	±	**Mg**	±
Silicate	0.56	0.19	0.11	0.13	0.12	0.02	0.64	0.06	0.25	0.16
Carbonate	0.00	0.00	0.00	0.00	0.77	0.04	0.32	0.06	0.70	0.16
Rain	0.44	0.19	0.89	0.13	0.11	0.04	0.05	0.02	0.05	0.01

For all other elements, the fractional contribution of silicate weathering is assumed to be 1.00 ± 0.00.
See Data Supplemental Table C4 for end member contributions in individual streams.

example, carbonates, evaporites or silicates). Because $W^{X}_{regolith}$ is measured on the small spatial scale of regolith, whereas W^{X}_{river} integrates over the catchment scale, these contributions likely differ. To allow inter-method comparison, solute concentrations must be corrected for non-silicate sources. For each site of the erodosequence, concentrations measured in water samples were first corrected for rain inputs assuming all Cl is sourced in rain. Thus $[X]_{diss,corrected} = [X]_{diss,uncorrected} - [Cl]_{diss} * (X/Cl)_{seawater}$, where $[X]_{diss,uncorrected}$ is the measured concentration of the solute X, $[X]_{diss,corrected}$ is the rain-corrected concentration, and $(X/Cl)_{seawater}$ is the marine X/Cl ratio (as the rainwater chemistry is usually considered to be derived from sea salts, at least for the solutes considered in the present study). Note that for consistency between the three sites we update the results for the EMMA in Sri Lanka from those presented in a previous publication (Hewawasam and others, 2013) where a different method was used to correct for rain water contribution.

To identify the sources of solutes in water samples and the proportions by which they contribute solutes, we examined our data in mixing diagrams (see fig. S1 in Data publication Part 2), using elemental molar ratios (Mg/Na, Sr/Na, Ca/Na, Na/Sr; all corrected for rain water inputs) ratios and Sr (^{87}Sr/^{86}Sr) isotope ratios. This ratio approach has the advantage over using simple element concentrations of dilution effects cancelling out. In addition, Ca, Mg, Na, and Sr are thought to be the most soluble rock-forming elements and to be the least sensitive to secondary phase formation, such that *a priori* these ratios can be considered conservative during water mass mixing. The "radiogenic" isotope ratio ^{87}Sr/^{86}Sr is insensitive to processes such as secondary phase formation and biological uptake, since internal normalization of the ^{88}Sr/^{86}Sr ratio during measurement removes any imprint of Critical Zone processes. As a consequence, these elemental and isotope ratios can be used to distinguish different rock types as solute sources, and to quantify the contributions thereof. The details of this analysis are provided in Data Publication Part 2, and the results are provided in table 3 and Data Table C4.

Data and Metadata Reporting and Supplementary Information

This publication is accompanied by an open-access online data publication at GFZ Data Services (von Blanckenburg and others, 2021) that consist of two parts.

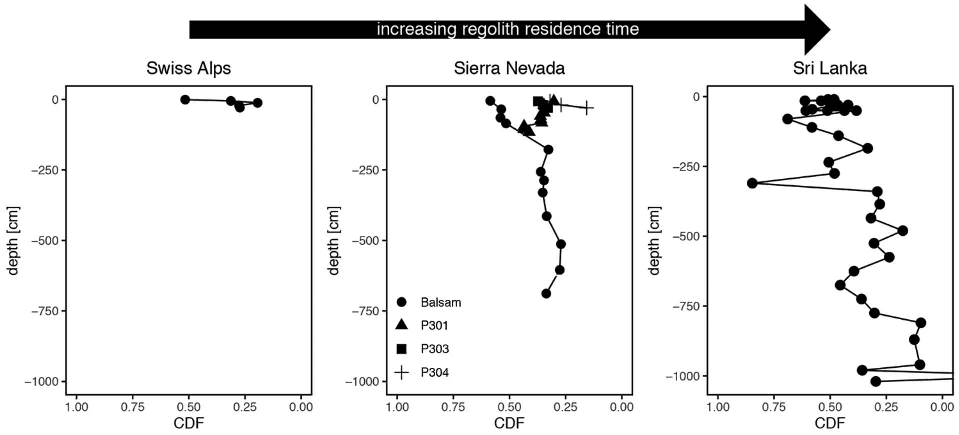

Fig. 5. Chemical Depletion Fraction (*CDF*; denoting the fractional mass loss of total solutes relative to unweathered bedrock, where 0 represents no loss, and 1 is complete loss; eq 4) *versus* depth in the weathering profiles of the three study sites. Soil and saprolite overlying granitic rock typically have a maximum possible *CDF* of *ca.* 0.5, due to the presence of weathering-resistant quartz and the formation of secondary aluminosilicates and Fe and Al oxyhydroxides.

All elemental concentration data produced in this study (together with data taken from previous publications: Uhlig and others, 2017; Schuessler and others, 2018) on bedrock, saprolite, soil, soil solutions, river water, groundwater, dominant plant species, plus a summary of rates previously published elsewhere are provided in an extensive set of background data tables (hereafter referred to as "Data Tables"). The aim is to make this data readily available for global compilations. These Data Tables provide support for metal isotope studies already published (Uhlig and others, 2017; Schuessler and others, 2018), plus the companion papers to this contribution (Bouchez and von Blanckenburg, 2021, Frings and others, 2021a, Frings and others, 2021b). All samples have been attributed a unique identifier, an "International Geo Sample Number" (IGSN), including parent- and daughter relationship. Sample metadata is linked to IGSNs at http://igsn.org.

Supplementary information is contained in a second part of this online data publication, hereafter called "Data Publication Part 2" (http://earth.eps.yale.edu/%7eajs/SupplementaryData/2021/vonBlanckenburg). This part contains 1) a detailed description of the results of the end member mixing analysis EMMA including their graphical presentation; 2) a re-assessment of the significance of dust input in the Sierra Nevada as previously published by Aciego and others, 2017; 3) XRD diffractograms of bulk samples at all sites.

RESULTS AND INTERPRETATION

Degree of Weathering

To characterize the degree of weathering at all three sites we calculated the chemical depletion fraction *CDF* (eq 4). *CDF* is shown in figure 5 and provided in Data Table A1 (Alps), SN1 (Sierra Nevada), and SL1 (Sri Lanka). Mean values are summarized in table 2. In the Alps, *CDF* is low, with values from 0.1 to 0.4 (mean value 0.3). In the Sierra Nevada, *CDF* is 0.3 to 0.5 (mean value 0.4). These values are typical of kinetically limited weathering regime throughout the profile that is typical for high-erosion rate settings. In Sri Lanka, the *CDF* ranges from 0.1 just above the weathering front to 0.6 in the topmost soil (mean value 0.5). This implies that near the

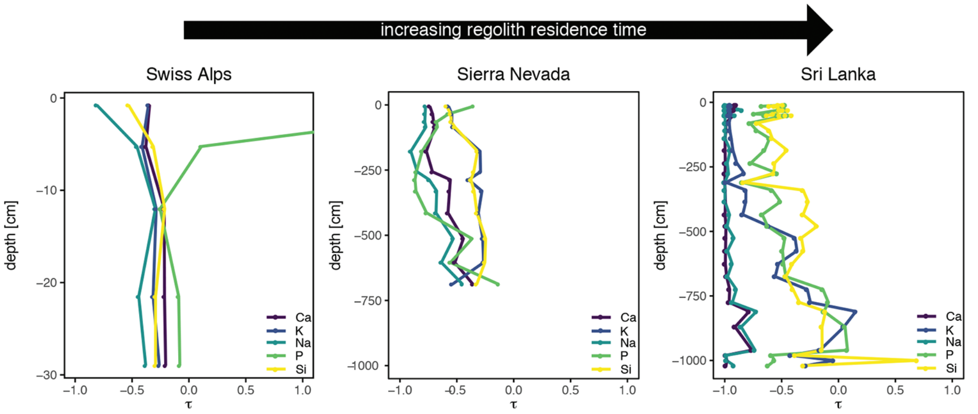

Fig. 6. Element-specific depletion fraction τ^x using Zr as the chemically immobile element for Ca, K, Na, P and Si plotted as function of depth for the three study sites. By convention τ^x is opposite in sign to *CDF*, such that 0 implies no loss, −1 is complete loss, and positive τ^x denotes elemental gain (eq 5).

surface, weathering has essentially run to completion and the site is in the supply-limited regime typical of well-drained, low-erosion rate settings.

Elemental depletion fractions τ_{Zr}^{X} confirm this picture and provide additional insight (fig. 6). In the Alps, τ_{Zr}^{X}values are uniform with depth, and only P is enriched at the surface. Na is most strongly depleted at $\tau_{Zr}^{Na}$of −0.5, indicative of efficient weathering of albite-rich plagioclase. In the Sierra Nevada Na is not totally depleted ($\tau_{Zr}^{Na} > -1$) at the surface, implying that plagioclase weathering does not run to completion, and small amounts persist to be eroded. K and Si remain in appreciable proportions, while P is depleted at depth but increases at the surface, as does K. Increasing τ_{Zr}^{X} for nutritive elements towards the surface of soil profiles is characteristic of nutrient uplift processes (Jobbagy and Jackson, 2001; Lucas, 2001). In Sri Lanka, almost all soluble elements (Ca, Na, K) are totally depleted meaning none of the primary minerals that host these elements can be exported by topsoil erosion. In the upper soil layers, P and Ca and Mg are enriched relative to deeper layers, hinting at nutrient uplift and the input of dust (see also Data Publication Part 2; fig. S1). Element depletion profiles in the Alps and Sierra Nevada are thus characteristic of kinetically limited weathering regimes, while the Sri Lanka site falls in a supply-limited regime (Dixon and others, 2012).

X-Ray Diffraction analyses also corroborate these interpretations. At the Alps site, the XRD diffractogram (Data Publication Part 2, fig. S3a) show that biotite and plagioclase abundances slowly decrease towards the top of the soil profile and that first signs of kaolinite appear. At the Sierra Nevada site, XRD diffractograms (Data Publication Part 2; fig. S3b; Uhlig and others 2017) show that plagioclase, K-feldspar, and biotite abundances decrease towards the surface but do not reach zero, while kaolinite abundance increases. Others have reported that clay contents are less than 10 % in SN soils (Dahlgren and others, 1997). At Sri Lanka, XRD diffractogram on bulk samples show that the abundance of plagioclase, K-feldspar, and biotite strongly decrease towards the surface whereas kaolinite abundances increase (Data Publication Part 2; fig. S3c). Published XRD diffractograms (Behrens and others 2015) of the clay-sized fraction show that kaolinite is the major secondary clay mineral throughout the regolith, followed by gibbsite, indicative of an intense weathering regime that produces a highly insoluble residue. In some cases, quartz and feldspars are detected in the clay-sized fraction.

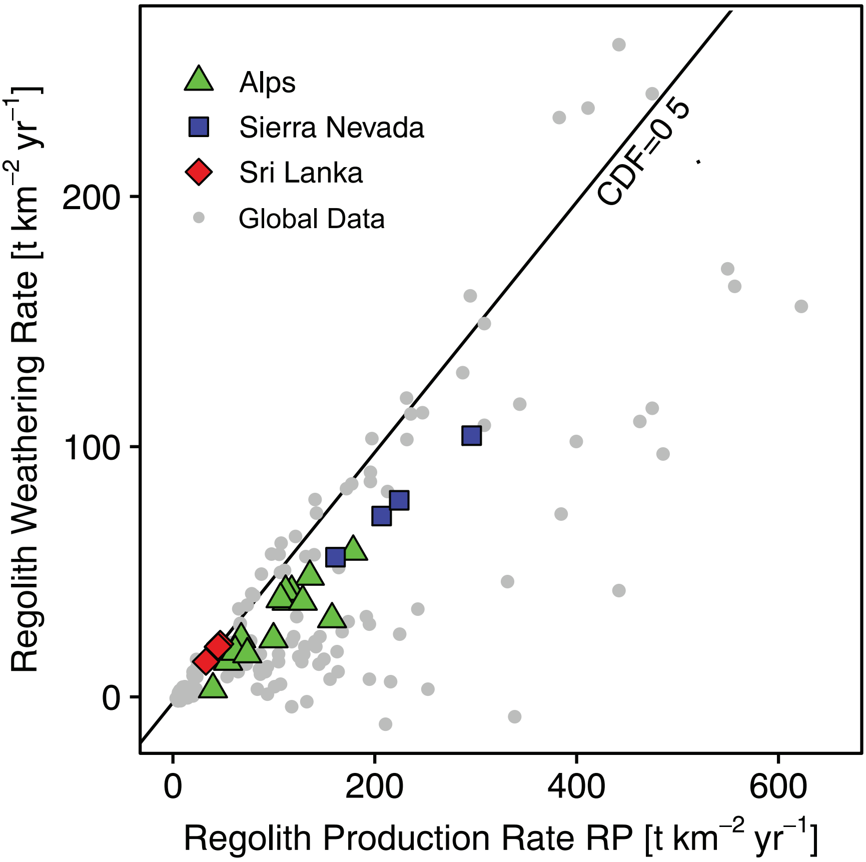

Fig. 7. Regolith profile weathering rate ($W_{regolith}$) *versus* regolith production rate (*RP*) for the three study sites. Regolith production rates are obtained from cosmogenic ^{10}Be in surface soil quartz as in figure 7. Regolith weathering rates are from the product of regolith production rate and soil *CDF*, (fig. 5; see eq 6). Grey symbols show global soil data from Dixon and von Blanckenburg (2012). The straight line shows the weathering-regolith production relationship for a chemical depletion fraction *CDF* of 0.5, which is the approximate maximum mass loss from felsic rocks, since roughly 50 % of the total initial rock mass either consists of quartz and minor refractory minerals, or is retained in secondary aluminosilicates and Fe- and Al-oxides, which are only sparsely soluble under most conditions. Data for the three sites are given in Data Table C2.

Weathering rates at all sites are correlated with regolith production rates (*RP*) and fall within the global range determined on soil samples (fig. 7). Only in Sri Lanka the empirical "maximum" weathering rate is reached for a given *RP*, whereas the Alps and the Sierra Nevada site are characterized by lower weathering rate for a given *RP*, testifying to their kinetically limited nature (fig. 7).

Sources of Constituents of River Dissolved Loads from End Member Mixing

The concentrations of dissolved constituents (major anions, cations, and Si) and properties such as pH, temperature and alkalinity are given in Data Tables A2 (Alps), SN2 (Sierra Nevada), and SL2 (Sri Lanka).

The elements used in the mixing diagrams (Ca, Mg, Na, Sr) of Data Publication Part 2, figure S1 are thought to be the most soluble elements and the least sensitive to secondary phase formation, such that to a first order the ratios between their concentrations can be considered to behave near-conservatively during mixing of different water masses. However, we show below that for some of these elements (Ca, Sr, Mg), the assumption that they are not incorporated into secondary phases or taken up by plants is not always valid. Nevertheless, the mixing diagrams show that silicate weathering is the sole source of dissolved constituents (besides rain) at the Sierra Nevada CZO. In particular, Sr and Nd isotope measurements indicate no significant influence of dust deposition at our sampling sites underlain by granodiorite, counter to the conclusion reached by Aciego and others(2017) (see next section for more details on potential dust input and Data Publication Part 2 for a re-assessment of the dust source and flux). Carbonate dissolution contributes Ca, Mg, and Sr to river water at the two other sites. In Sri Lanka, this carbonate source is likely deposition of carbonate-rich dust since the impact is seen in both the upper regolith and stream water chemistry. In the Alps, the contribution likely stems from weathering of marble layers disseminated in gneiss bedrock. Additionally, two end members of silicate weathering can be distinguished at the Alps site: a "hillslope" end member representing weathering in soils and a "deep" end member reflecting fluid-rock interactions taking place at depth in fractured rocks (Data Table C4). The deep end member is marked by strong scavenging of dissolved Mg (compared to surface waters collected in soils or rivers), presumably through the formation of Mg-rich clays in fractures, which constitutes an example of a non-conservative behavior of Mg. The waters circulating in these deep fractures are thought to reach the streams through seepage. However, both these end members represent weathering processes affecting Alps local silicate rocks.

At the Sierra Nevada CZO, besides fluid-rock interactions, the imprint of biotic uptake is visible in ground- and stream waters by the depletion of the rock-derived nutrients Ca, Mg, and Sr relative to Na. In contrast, shallow soil water samples are enriched in these nutrients, which we attribute to their release during litter decomposition.

Quantitative apportionment of dissolved constituents between these different sources was obtained by solving mixing equations (results shown in table 3, and in more detail in Data Table C4). In the Alps and Sri Lanka the contribution of carbonate inputs to stream dissolved Ca, Mg, and Sr can be significant (30 to 80 %). The fractional contribution of wet deposition to total inputs (silicate rock weathering plus wet and dry deposition) is significant for K and Na only, and increases from Alps (a few percent) to Sierra Nevada to Sri Lanka (where it reaches almost 90 % for Na). Dry deposition (carbonate dust) is significant in the Alps and Sri Lanka for Mg, Ca, and Sr, where its contribution is between 20 and 40 % for these elements (Data Table C5).

For each site, to compute DEE^X and DEE^X_{Na} we use the results from the end member mixing analysis to calculate silicate-specific solute concentrations to be used in equations (13) and (14). In other words, we calculate whether fluxes of silicate derived elements that are lost from the regolith appear in equal quantity in the streams draining the catchments. Additionally, given the significance of rain (for Na and K) and carbonate dust inputs (for Ca, Mg, and Sr) to the ecosystem's elemental budgets in Sri Lanka, at this site we compute "total" values Rec^X, DEE^X, and DEE^X_{Na} that encompass all inputs, using the results of the end member mixing analysis to quantify wet and dry deposition fluxes in the full versions of equations (12), (13), and (14). With this "total" calculation, we are essentially comparing all sources of solutes (silicate, carbonate, dust, rain) with the observed rate of loss in river water.

Denudation, Erosion, Weathering Rates, and Atmospheric Inputs

The landscape-scale denudation rates of 220 to 5500 t km^{-2} yr^{-1} for the Alps, 70 to 200 t km^{-2} yr^{-1} for the Sierra Nevada, and 50 to 100 t km^{-2} yr^{-1} for Sri Lanka (table 2,; Data Table C2; fig. 8) define the three categories of our "erodosequence": fast, moderate, and slow. The rates at the three sites are typical of these domains in global compilations of catchment-wide denudation rates (Portenga and Bierman,

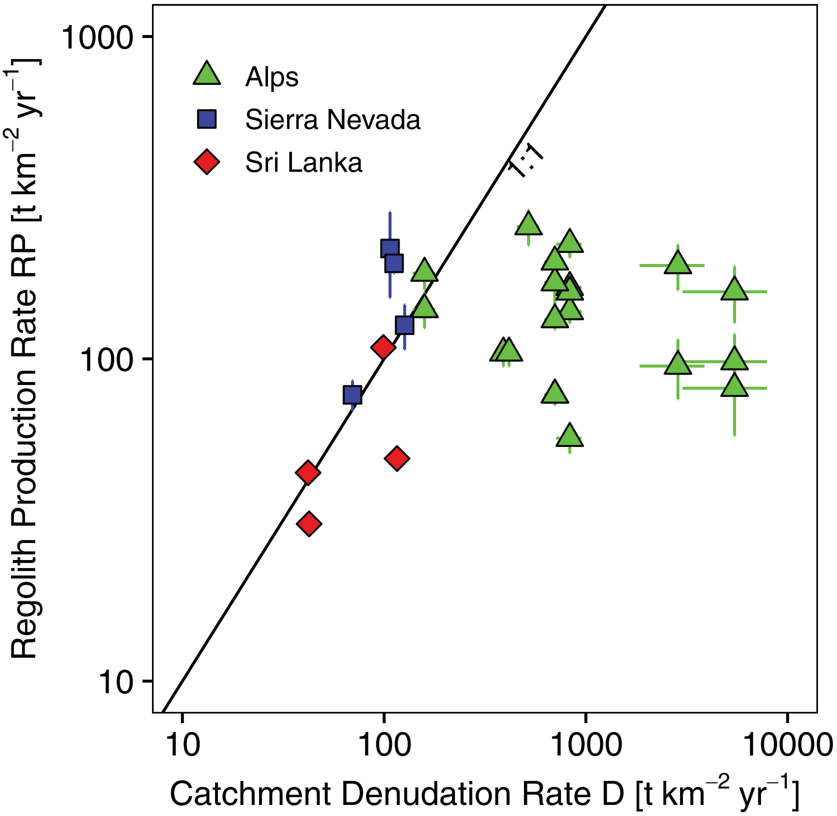

Fig. 8. Regolith production rates (*RP*) *versus* catchment-scale denudation rate (*D*) from cosmogenic ^{10}Be in quartz in adjacent creek and stream sediments for the three study sites. Regolith production rates from soil denudation rates from cosmogenic ^{10}Be in surface soil quartz are assumed to be equal to regolith production rate at steady-state, and. Regolith production represents a near landscape-wide average in Sierra Nevada and Sri Lanka. In the Alps, soils do not exceed a "speed limit" (450 t km^{-2} yr^{-1}, Dixon and von Blanckenburg, 2012) even though landscape-scale denudation rates are higher. Data are given in Data Table C1.

2011; Codilean and others, 2018). These landscape scale rates are ultimately set by a combination of tectonic and climatic forcing, but they do not necessarily reflect the fluxes found in the weathering zone or in river dissolved loads, which are capped by an upper limit (Dixon and von Blanckenburg, 2012) that we illustrate next.

Soil denudation rates *D* (taken to be equivalent to regolith production, *RP*, table 2 and Data Table C2) is 103 t km^{-2} yr^{-1} in the Alps, 221 t km^{-2} yr^{-1} in the Sierra Nevada, and 42 t km^{-2} yr^{-1} in Sri Lanka. Dividing regolith thickness by denudation (or regolith production) rate yields regolith residence times of 10 kyrs in the Alps, 86 kyrs in the Sierra Nevada, and 600 kys in Sri Lanka (table 2). These residence times are broadly reflected in the respective chemical depletion fractions (*CDF*) and thus set the state of weathering. Using the denudation rates in conjunction with mean *CDF* values (table 1) from each site and equation (6) to determine regolith weathering rates $W_{regolith}$ yields chemical weathering rates of 32 ± 25 t km^{-2} yr^{-1} and erosion rates (calculated as the difference between *D* and $W_{regolith}$), of 71 ± 55 t km^{-2} yr^{-1} in the Alps. At the Sierra Nevada site, chemical weathering rates are 80 ± 28 t km^{-2} yr^{-1} and erosion rates are 141 ± 50 t km^{-2} yr^{-1}. In Sri Lanka, chemical weathering rates are 20.8 ± 7.0 t km^{-2} yr^{-1} and erosion rates are 20.8 ± 7.0 t km^{-2} yr^{-1}.

In Sri Lanka and the Sierra Nevada *RP* agrees within a factor of two with landscape scale *D* as measured by cosmogenic ^{10}Be in river sediment, meaning that our regolith production rates effectively reflect landscape-scale averages (fig. 8). In the Alps this is not the case, and catchment-scale denudation rates exceed regolith production rates by up to two orders of magnitude. These rates of up to 5000 t km^{-2} yr^{-1} are typical of high, uplifting, and formerly glaciated mountains. Yet even here, the regolith production rates conform to the upper limit to soil production rates captured in the concept of a "speed limit" of 450 t km^{-2} yr^{-1} (Dixon and von Blanckenburg, 2012). Landscape-scale denudation rates include large mass wasting events that do not allow for the development of a weathering zone, and hence of soils, which form on stable hillslopes and ridges. In support of this hypothesis, we note that the regolith thickness, which is around 7 and 10 m in Sierra Nevada and Sri Lanka, respectively, is only 0.35 m in the Alps. Regolith depths of around 5 to 10 m are typical of weathering zones formed on felsic rock in landscapes with slow erosion (Bazilevskaya and others, 2012). The shallow depth in the Alps therefore likely results from the fast landscape scale erosion rates that prohibit long regolith residence times in order to maintain a stable relief (fig. 1). An alternative explanation is that the shallow soil thickness reflects non-steady state following the resetting of land surfaces by glaciation of the last ice age (Norton and von Blanckenburg, 2010; Norton and others, 2010). In the absence of independent *RP* rate estimates, this possibility is hard to conclusively rule out, but application of the time-dependent weathering model of Ferrier and Kirchner (2008) by Norton and others (2010) suggested that the $>$ 15 kyrs time elapsed since deglaciation is sufficient to allow for the attainment of steady-state soil thickness.

A means to assess whether weathering is at steady state (that is, that the rates of loss of soluble elements from the regolith over a multi-kyr time scale correspond to the river export rate of the dissolved elements over a multi-yr time scale) is offered by the comparison between regolith weathering rates $W_{regolith}$ and catchment scale weathering rates W_{river} (Buss and others, 2017, Hewawasam and others, 2013). We find that the silicate portion of W_{river}, calculated from equation (9) by multiplying the silicate weathering contribution to local stream chemistry with representative discharge data for streams in the area (table 2) is similar to or lower than $W_{regolith}$. In the Alps, W_{river} is 43 t km^{-2} yr^{-1} while $W_{regolith}$ is 32 ± 25 t km^{-2} yr^{-1}. In the Sierra Nevada, W_{river} is 11 t km^{-2} yr^{-1} where $W_{regolith}$ is 80 ± 28 t km^{-2} yr^{-1}. In Sri Lanka, W_{river} is 18 t km^{-2} yr^{-1} where $W_{regolith}$ is 20.8 ± 7.0 t km^{-2} yr^{-1}. We note that W_{river} and $W_{regolith}$ must not necessarily agree, given that the two approaches integrate over very different time scales, and W_{river} is affected by annual variations in runoff, an issue we address below by introducing a normalization of concentrations by that of Na. For example, the Sierra Nevada site has been affected by drought in the past decade (Aarons and others, 2019). W_{river} might also be lower than $W_{regolith}$ if a substantial fraction of solutes is exported by plant debris (see section below on the dissolved export fraction *DEE*). Nevertheless, the fact that both estimates are within the same range means that a) weathering at our sites is close to steady state; b) weathering takes place where soils form, rather than on fast-eroding soil-free surfaces that exist in the sampled catchments in the Alps where catchment-scale cosmogenic ^{10}Be estimates of *D* exceed soil-derived *D*, indicating fast erosion of soil-free surfaces (fig. 8).

Atmospheric inputs are much lower than regolith production rates in the Sierra Nevada and the Alps. In the Swiss Central Alps near Monte Rosa (Wagenbach and Geis, 1989) determined an average dust flux of 0.6 t km^{-2} yr^{-1} as recorded in a 50 yr glacier ice-core record, with a maximum annual input of 5.4 t km^{-2} yr^{-1}. Thus, we assume a range of 0.6 to 6 t km^{-2} yr^{-}1 for the Swiss Central Alps. With 6.6 t km^{-2} yr^{-1} in the Sierra Nevada (Arvin and others, 2017) dust inputs are in a similar range. As shown below, the ratio of elemental dust deposition to the local, bedrock-derived elemental supply flux (referred to as RP^X, eq 3) amounts to less than 4 % for K, Ca and Mg and to about 5 % for P at our sites. Therefore, the atmospheric supply flux of mineral nutritive elements can be considered to be insignificant relative to the local long-term supply fluxes from weathering (Uhlig and others, 2017). In contrast, Aciego and others(2017) concluded that dust flux in the Sierra Nevada outpaces nutrient supply from bedrock. We find – for a variety of reasons – that this conclusion is not valid for the granodiorite site studied here. Further details are given in Data Publication Part 2. Our interpretation of low dust fluxes to the Sierra Nevada site is supported by more recent measurements of dust fluxes (Aarons and others, 2019) that are an order of magnitude lower than those measured by Aciego and others (2017). In the Sri Lankan Highland the origin and magnitude of potential dust inputs have not been determined in detail. Yet Hewawasam and others (2013) have estimated an upper limit of atmospheric dust flux to the Sri Lankan Highlands of 5 to 10 t km^{-2} y^{-1}. This dust flux has been measured in marine sediments west of Sri Lanka (Dirtmap data base http://www.bridge.bris.ac.uk/projects/DIRTMAP; Kohfeld and Harrison, 2001) and is consistent with measured enrichment of Ca, Mg, Al, Ti, and Si in the Hakgala top soil by addition of carbonate and silicate-rich dust from global or regional sources (Hewawasam and others, 2013). To summarize, atmospheric inputs are low relative to bedrock supply at all three sites along the erodosequence in terms of total mass, although they are significant for the alkali-earth elements in Sri Lanka.

Ecosystem Fluxes

Biomass production (taken as numerically equivalent to GPP; see above) extracted from a global data product based on a machine-learning combination of FLUXNET eddy covariance site data, meteorological data and satellite imagery (Jung and others, 2019) at a 0.5° resolution is 780 ± 18 t km^{-2} yr^{-1} in the Alps, 1350 ± 54 t km^{-2} yr^{-1} in the Sierra Nevada, and 3000 ± 100 t km^{-2} yr^{-1} in Sri Lanka (table 2; fig. 9). Uncertainty is given as 2σ of the annual estimates from 1980–2013 (see detailed background data used to derive ecosystem fluxes in Data Table C5). The relative differences between the sites are consistent with Alpine slopes being covered with grassland and exceedingly rare patches of Edelweiss (*Leontopodium nivale*), the Sierra Nevada with mixed conifer forest, and the Sri Lankan Highlands with a pristine tropical rainforest. The absolute values are consistent with multi-yr eddy covariance flux tower measurements in similar environments in the Alps and Sierra Nevada (Galvagno and others, 2013; Kelly and Goulden, 2016), and with litter-trap experiments in a similar Alpine grassland and at the Sri Lanka site (Weerakkody and Parkinson, 2006a; Joos and others, 2010). Estimates of GPP derived purely from MODIS imagery at a 30 arcsecond resolution (Zhao and others, 2005, 2006) also agree well, as does the estimate of aboveground biomass production produced by Uhlig and others(2017) for the Sierra Nevada site. Figure 9 and Data Table C5 compare these different estimates. For consistency, we use biomass production from the FLUXNET upscaling (Jung and others, 2019) at all sites.

Using these fluxes in conjunction with foliar and wood concentrations of the nutritive elements (Data Tables A3, SN3, and SL3), we calculate U^X, the rate of incorporation of elements into plant biomass. Potassium and calcium are the two most abundant elements in biomass at all three sites, followed by P and Mg with roughly equal abundance. There are substantial inter-site differences, with element uptake being uniformly higher in Sri Lanka than Sierra Nevada by about an order of magnitude. In turn, Sierra Nevada has greater element uptake rates than the Alps, though only by a factor of two, with the exception of K (Data Table C5). The increase in U^X from the Alps to Sierra Nevada is largely explained by the biomass production rate

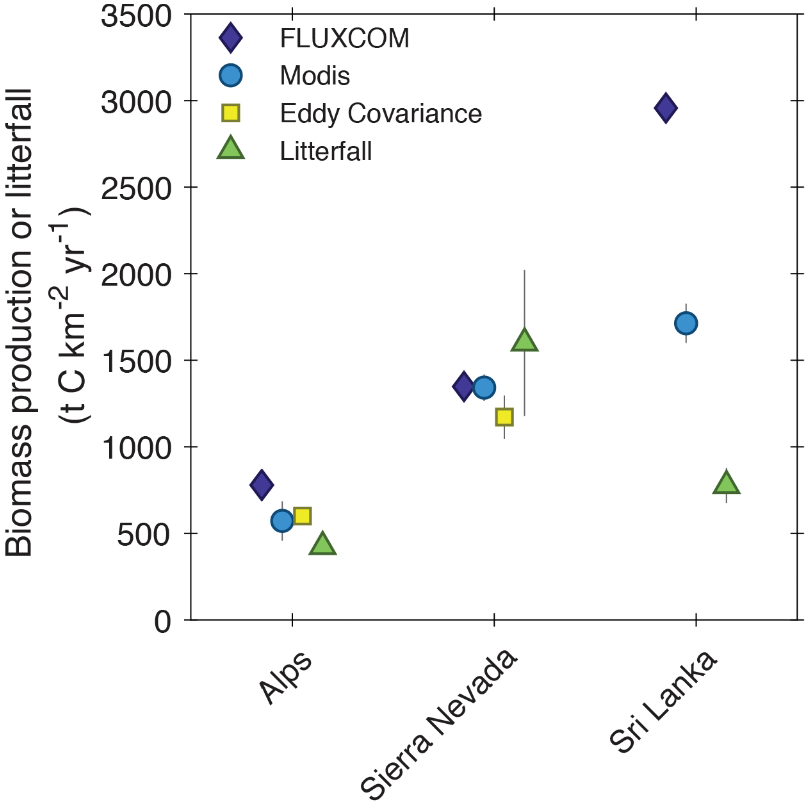

Fig. 9. Biomass production at the three sites, as estimated by different methods. FLUXCOM: Annual Gross Primary Production (*GPP*) estimates for 1980–2013 derived via a combination of FLUXNET eddy covariance data, remote sensing imagery and metrological data at a 0.5° resolution within a machine-learning framework (Jung and others, 2019). The uncertainties are smaller than symbol sizes unless indicated otherwise. Modis: GPP estimates from 16 years of Modis remote sensing data (2000–2015) at a 30 arcsecond resolution (Zhao and others, 2005, 2006). Eddy Covariance: The nearest available eddy covariance towers are: Torgnon in the Acosta Valley, 2160 masl, *ca.* 90 km to southwest of the Alps site (Galvagno, ms, 2011; Galvagno and others, 2013) and Providence Creek in the Sierra Nevada (Kelly and Goulden, 2016). Biomass production is estimated by assuming that NPP(C) = GPP(C)/2, and further that dry biomass consists of 50 wt % carbon, such that total biomass production is numerically equivalent to GPP. Litterfall: Estimates of aboveground biomass production, as estimated by a nearby litter experiment in the Alps (Joos and others, 2010), via a compilation of literature growth rates and allometry for the dominant *Pinus* species in Sierra Nevada (neglecting root biomass production, unlike Uhlig and others,2017), and from three years of litter-trap monitoring in Sri Lanka (Weerakkody and Parkinson, 2006b). See also Data Table C5. In this paper we use FLUXCOM data throughout to calculate the derived metrics (U^X, Rec^X) because this source is the most comprehensive combination of MODIS imagery, eddy covariance carbon fluxes and meteorological data. In contrast, litterfall for example can underestimate biomass production by the mode of field collection.

(Data Table C5), while the increase from Sierra Nevada to Sri Lanka reflects both increasing biomass production rates and higher plant element concentrations.

From the ratio of U^X to $W_{regolith}$, we derive the elemental recycling factors Rec^X, the ratio of elemental plant uptake relative to elemental release by weathering (eq 12). The Rec^X can be seen as a metric for nutrient supply *versus* ecosystem demand that however provides a minimum estimate of the number of cycles the nutrient takes through biomass as some fraction of element *X* might be lost from the system immediately after solubilization, for example at depth in the regolith, and take no part in biological recycling. The resulting values are given in Data Table C5. At all sites, Rec^X shows distinct ecological stoichiometric patterns, with Rec^X being the lowest for Fe and Na, followed by Si -

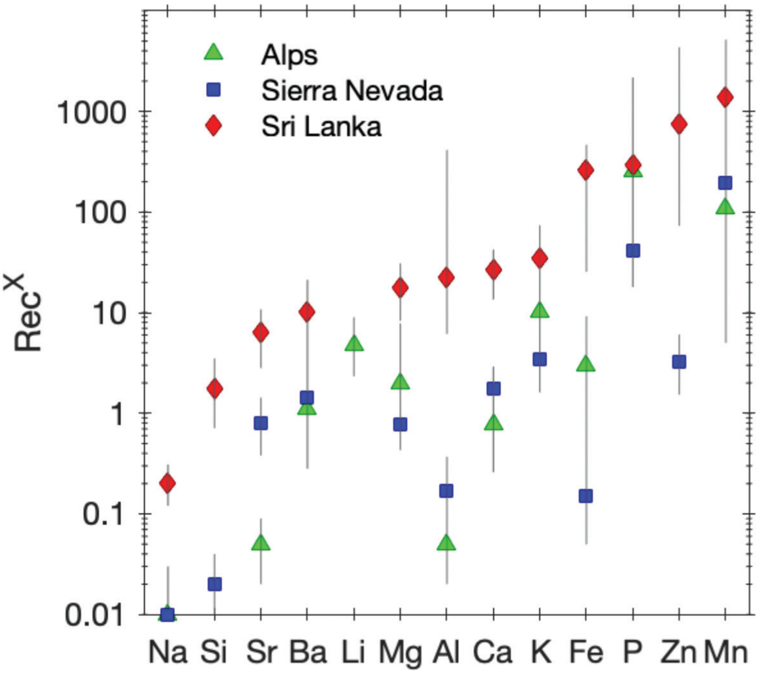

Fig. 10. Elemental recycling factor (Rec^X), defined as elemental biomass uptake (U^X) divided by elemental weathering rate ($W^X_{regolith}$) for a given element for the three study sites. Rec^X quantifies the number of passages of a nutritive element X through vegetation after solubilization from rocks and before being exported in stream water; that is, the plant uptake rate relative to its release rate from the source (regolith weathering, excluding atmospheric inputs) and presents a minimum estimate as not all solute released may reach the vegetation. Estimates of Rec^X are shown for the major mineral nutrients at the three sites (Data Table C5). Elements are sorted in ascending order of Rec^X.

generally assumed to be in low ecological demand for most gymnosperms and non-grass angiosperms (Hodson and others, 2005). Rec^X increases in the order Na < Si < Sr < Ba (< Li) < Mg < Al < Ca < K < Fe < P < Zn < Mn. The most essential mineral nutrients (for example, P, Zn, Mn), yield the highest Rec^X at all three sites (figs. 10 and 11). Recycling factors are > 1 for almost all nutrients in Sri Lanka, typical of a tropical recycling ecosystem. In these settings, dust inputs or deep nutrient uptake provide the "new" nutrient input to balance the minor nutrient loss in runoff (Schuessler and others, 2018). In Sri Lanka P is recycled ~ 300 times before being exported in stream water. In the Sierra Nevada and Alps sites, K, P, and Mg are the only elements consistently recycled multiple times (Uhlig and others, 2017). Figure 10 shows that recycling factors are not consistently offset between the Alps and Sierra Nevada. Given that U^X values are similar between the sites, this is a result of the low weathering release fluxes $W_{regolith}$. These results are in line with the hypothesis of Lang and others (2016) that recycling rates are determined by soil nutrient status and not necessarily ecosystem productivity.

Watershed Flux Balances

With the dissolved export efficiency DEE^X (eq 14), we evaluate whether the regolith elemental release rate $W^X_{regolith}$, integrated over the kyr residence time of regolith, is balanced with the riverine dissolved export flux W^X_{river} averaging over a few years. Differences introduced by short-term fluctuations in runoff are mitigated by means of the Na normalization. We note that before correction an apparent imbalance exists in

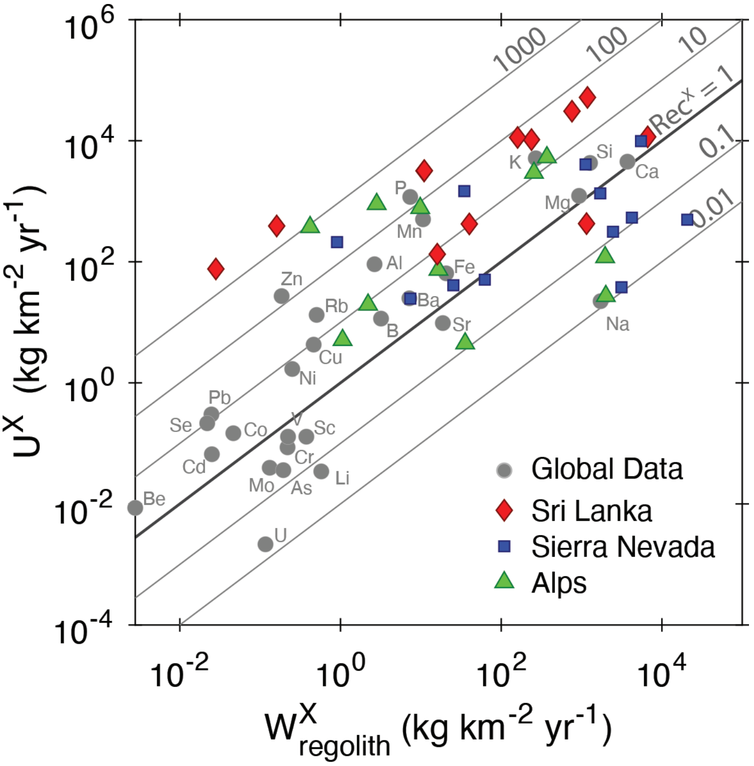

Fig. 11. Plant elemental uptake flux U^X vs element supply flux from regolith $W^X_{regolith}$. Contour lines show various recycling factors Rec^X which is the ratio $U^X/W^X_{regolith}$ (eq 12). For the three study sites, we use our site-specific measurements of plant concentration, biomass production, denudation rates, and τ^X_{Zr} to derive the two axes (fig. 10). For the global average data (grey circles), we used typical plant element concentrations from Reimann and others(2001), an estimate of global net primary production of 55 × 10^{15} g C yr^{-1} from Zhang and others(2017), the product of which was normalised by the global vegetated surface area (1.28 × 10^8 km^2) from Jung and others (2011) to derive global average U^X. We take average river concentrations from Gaillardet and others(2003) and Meybeck(2003) for trace and major elements, respectively, and global river discharge of 36 × 10^{15} l yr^{-1} (Milliman and Farnsworth, 2011), the product of which is normalised by global exorheic area (1.15 × 10^8 km^2) to derive a global average $W^X_{regolith}$. The mineral nutrients (P, Zn) show the highest global recycling factors, and other plant essential and beneficial elements (including K, Mg, Ca, Si) also plot at $Rec^X \geq 1$. The offset between the Sri Lanka site and the other two sites shows that the nature of this relationship is governed by erosion rate and in turn availability, superimposed onto which is biological demand.

the form of an excess for those elements added from atmospheric sources (Sr, Mg, Ca, Data Table C5). For almost all elements an export deficit is apparent with DEE^X_{Na} in the order of Al < Zn < Sr < Rb < P < Li < Ba < Mg < Si < Ca < K (fig. 12). Because the low-*DEE* elements Al and Zn are typically colloid-bound, whereas the other elements are also plant-essential, we suspect that a significant part of the release flux by weathering is partitioned into either colloidal transport or plant organs, and not returned into the local stream dissolved load. We return to this mystery in the following discussion section.

DISCUSSION

Shaping the Critical Zone along an Erodosequence

The regolith production and weathering rates (fig. 7) and the residence times of 10, 86, and 600 kyrs for the Alps, Sierra Nevada, and Sri Lanka regolith, respectively,

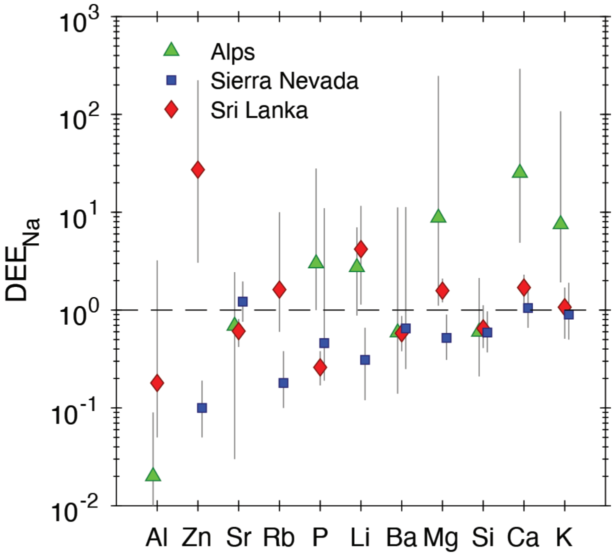

Fig. 12. Na-normalised dissolved export efficiency (DEE^X_{Na}) shown for the three study sites. DEE^X_{Na} quantifies the dissolved riverine export of element X from a watershed relative to its net release from the regolith. DEE^X_{Na} was calculated as defined in equation (14), using element concentrations as measured in river water, rock, soil and saprolite; elements are sorted in ascending order of DEE^X_{Na}. River water concentrations are corrected for non-silicate inputs (see EMMA section in Data Publication Part 2). Note that these corrections result in high uncertainties, in particular for the Alps data. See Data Table C1 and C5 for details. $DEE^X_{Na} > 1$ indicates solute inputs into the fluvial system in addition to silicate rock weathering.

reflect the eroding nature of these steadily eroding sites located on mountainous, well-drained hillslopes, that therefore present an "erodosequence" rather than the "chronosequence" that would form on non-eroding surfaces (fig. 1). Note that the difference in residence times is defined by the combination of both denudation rate and regolith thickness. The three sites are real-world examples of the model cases developed in figure 1. Sri Lanka is the thick, nutrient-depleted regolith with the longest residence time where ecosystems must necessarily be nourished by recycling and/or atmospheric inputs. The weathering regime can be termed "supply-limited" as little primary minerals remain and the τ^X_{Zr} values of soluble elements like Ca and Na approach -1. The long regolith residence time results from the tectonically quiescent setting (which limits landscape rejuvenation) in conjunction with the steady tropical climate (von Blanckenburg and others, 2004). The Sierra Nevada is a similarly deeply weathered system where plants have been suggested to obtain their nutrients at the weathering front (Uhlig and others, 2017); yet the fast denudation rate ensures that primary minerals are left, the τ^X_{Zr} values of soluble elements are intermediate, and the system can be called "kinetically limited", meaning that mineral solubility is too sluggish to allow for complete dissolution during the time taken for minerals to advect upwards to the surface. The Alps represent the shallow nutrient-rich system of figure 1. As a consequence, regolith thickness is minimal and *CDF* is low as primary minerals are only partially depleted. As with the Sierra Nevada, the system can be called "kinetically limited", meaning that weathering reactions receive no further benefit from mineral supply (Norton and von Blanckenburg, 2010).

In addition to constraining the role of solid residence time on weathering processes and rates, the erodosequence concept allows for the exploration of the relationship between solid and fluid residence time and its effect on weathering. In the hydrologic framework proposed by Maher and Chamberlain (2014) this relationship is expressed through the Damköhler coefficient *Dw*, which is a function of the availability of primary mineral and water flow. In other words, *Dw* is a function of fluid residence time *versus* solid residence time in the weathering zone. In this context, we can conceptually expect that Sri Lanka will reflect a low, typically "cratonic" *Dw*, whereas the Sierra Nevada and Alps sites will be characterized by a higher *Dw* more characteristic of collisional settings. Although the absence of hydrologic constraints on flow path length and fluid residence time at our sites precludes a full parametrization of *Dw*, the regolith thickness and primary mineral residence time supplied by our study is halfway towards its quantification.

The fact that river weathering fluxes W_{river}, reflecting the landscape scale, broadly agree with regolith weathering rates $W_{regolith}$, representing the hillslope scale (table 2), informs us that *in situ* soils and regolith, rather than colluvial deposits, are responsible for the bulk of silicate weathering fluxes. In the Alps, where loose rock debris from glacial deposits and landslide blankets the valleys and lower hill slopes, we would expect W_{river} to exceed $W_{regolith}$ if this material contributed a non-negligible weathering flux (Emberson and others, 2016). One explanation for such lack of a resolvable non-regolith weathering flux despite abundant colluvium is that a "thermodynamic limit" has been reached. If the supply of weatherable material and the provision of reactive surface area is sufficient, soil solutions and thus river water can quickly attain a saturation with respect to the suite of minerals undergoing dissolution. This is often approximated as a limit in dissolved silica concentrations (Maher and Chamberlain, 2014). Upon reaching this limit, concentrations (and thus weathering fluxes) cannot increase any further even when solutions interact with fresh rock debris. We note, however, that the Alps streams contain a component of carbonate dissolution (table 3, fig. S2), and, unlike the silicate weathering flux, this contribution (around 50 %) might increase by the interaction with colluvial deposits (Emberson and others, 2016).

Nourishing Ecosystems along an Erodosequence

The metrics used here permit an evaluation of whether weathering characteristics set the supply of mineral nutrients to the ecosystems that exist with them, focusing in particular on the plant-essential mineral nutrients P, K, and Mg. We note that this evaluation is not fully rigorous, since the gradient in regolith chemical depletion is not observed in isolation: climatic and ecological differences may also influence biomass growth along the erodosequence. As a result, the uptake of fresh mineral nutrient relative to recycled nutrient (called "new" by Cleveland and others (2013) is highest in the Alps, reflected by the low recycling factors. Sri Lanka has the lowest relative uptake of fresh mineral nutrients, which is manifest in our estimates of Rec^X for P, for example, an element that is recycled through the tropical forest about 300 times before being exported. The combined result of decreasing weathering rate and increasing primary productivity is that along the erodosequence, the prevailing ecosystems shift from acquiring (meaning relying on uptake of fresh nutrient from regolith) to almost fully recycling systems.

Whether an individual element is recycled depends on plant physiological demand relative to supply. Indeed, using global plant stoichiometry, plant growth rate averages, and global riverine weathering fluxes, the recycling ratio Rec^X for a suite of rock-derived elements increases with the ratio of an element concentration in vegetation relative to that in rock, as shown in figure 11. Elements that plot to the left have low ecological relevance while those to the right tend to have well-known biological functions. Yet at any given plant-to-rock concentration ratio, the global data in figure 11 has a scatter in Rec^X by more than one order of magnitude. This scatter results from weathering zone characteristics that are site-dependent. As further evidence for this, Rec^X at the Alps, Sierra Nevada, and Sri Lanka sites are plotted in figure 11. The rapidly eroding Alps site with thin soils has the lowest Rec^X for all elements, while Sri Lanka has the highest Rec^X. This suggests that where element supply is slow and the regolith is nutrient-depleted, recycling must be efficient to fulfill the needs of the ecosystem. Conversely, weathering zones characterized by rapid element supply through regolith production – like the Alps and Sierra Nevada sites – can operate with less efficient recycling. Either there is an energy penalty associated with obtaining nutrients from biogenic material when mineral forms are available, or more rapidly eroding sites preclude the possibility of recycling with the same efficiency as long-residence time tropical settings. These systematics add to recent results suggesting that it is the inventory of the plant-available mineral nutrients in the shallow and deep Critical Zone that potentially sets ecological stoichiometry (Uhlig and von Blanckenburg, 2019).

More generally, this recycling hypothesis has relevance for the suggestion that plants and associated microbiota impact weathering fluxes (Moulton and others, 2000; Berner and others, 2003; Chaudhuri and others, 2007; Cornelis and others, 2009; Riotte and others, 2014). In agreement with a recent study along a vegetation gradient in Chile (Oeser and von Blanckenburg, 2020a) we find that the large range of nutrient recycling factors, inversely related to erosion rate, buffers ecosystem nutrition making it virtually independent from rock weathering.

Is There a Hidden Elemental Export Pathway or Pool?

The element-specific "dissolved export efficiency" DEE^X (eq 13) suggests that for most of the major elements, $W^X_{regolith}$ is systematically larger than W^X_{river}. Exceptions include Ca and Mg in the Alps, where end member mixing analysis (Data Publication Part 2) shows that most river Ca, Mg and Sr are derived from dissolution of disseminated carbonates – and thus not accounted for in $W^X_{regolith}$. In terms of the DEE^X_{Na}, about half of the values are below unity (fig. 12). We explore four possible explanations for this apparent imbalance in fluxes: 1) methodological artifacts; 2) a departure from steady state in fluxes; 3) element fractionation along the hillslope or at depth; or 4) a hidden element export pathway or pool.

1) Methodological artifacts.—A DEE^X that differs from 1 may result from biases in the input data. Potential causes include i) the partial mobility of Zr (used as an immobile element in the calculation of τ^X_{Zr} hence of DEE^X; ii) erroneous correction of non-silicate inputs; iii) differing lithology between the river scale and the regolith profile scale, such that the river drains rocks including minerals of different chemistry or solubility than those directly underlying the soil profiles. Values of DEE^X_{Na} above > 1 can be attributed to causes ii) and iii) and indeed we find these for Mg, Ca, P, K, and Li in the Alps, where stream water contains non-silicate inputs. We also observe $DEE^X_{Na} > 1$ for Mg, Ca, and Li in Sri Lanka where supply of these elements via atmospheric deposition constitutes a significant fraction relative to weathering (fig. 12 and Data Table C5). Even though these sites have been subjected to an end member mixing analysis (Data Table C4), artifacts may remain if the correction for non-silicate inputs was slightly erroneous.

As we observe a systematic pattern of $DEE^X < 1$, cause i) can be dismissed as Zr mobility would result in an underestimation of τ^X_{Zr} and thus in an overestimation of DEE^X; while causes ii) and iii) are unlikely because they should not introduce a systematic bias. Thus, the fact that we consistently observe $DEE^X < 1$ for many elements (Data Table C5) cannot be readily explained by these methodological biases.

However, a systematic underestimation of W^X_{river} and of DEE^X could arise artificially if iv) a substantial fraction of soluble elements escaping the regolith in the "fine colloidal" form (100 to 300 nm; Zirkler and others, 2012; Gottselig and others, 2017, 2019) have not passed the 0.2-μm mesh size at which the stream samples were filtered. In this case this flux would neither appear in the nominal dissolved fraction nor remain in the regolith. In particular elements that are present in the colloidal form like Al, Ti, Mn, Fe, and the REEs (Trostle and others, 2016) and P (Gottselig and others, 2017) might be prone to this effect. Indeed, we find the lowest DEE^X for Al, an element of low solubility. This explanation is unlikely for elements that do not appear as colloids like Mg, Ca, K, Na, Sr, and Si (Trostle and others, 2016), and in any case is not supported by any evidence at our sites. As an alternative explanation, observations from the Shale Hills CZO suggest that very fine particles, containing amorphous Al-, Si, and Ti-precipitates and even Mg and K particles are leaving the weathering zone several meters beneath the surface (Kim and others, 2018). If these do not pass through the filter they might contribute to the deficit in the dissolved fraction of these elements.

2) Perturbation of the steady state in fluxes.—At a site in which the Critical Zone is at perfect steady state, input and output fluxes balance and are constant with time. If the steady state is perturbed, deviations from the erosion rate *versus* weathering rate relationships may emerge (Ferrier and West, 2017). One common test of flux constancy is to compare millennial time scale D or RP from cosmogenic nuclides with annual to decadal time scale solid and dissolved export rates from river monitoring. Another possibility to test for the steady state is to compare the loss rate of soluble elements from the regolith ($W_{regolith}$) to the flux of solutes export by rivers (W_{river}). This requires that the measured river concentrations and runoff are representative over the time scales of $W_{regolith}$ estimates, and that $W_{regolith}$ has been largely invariant over these time scales. At face value, if $DEE^X < 1$, this means that $W_{river} < W_{regolith}$ and that the system is not operating at steady state. However, to evaluate whether other explanations exist, we eliminate the strongly time-dependent terms in equation (13) via the metric DEE^X_{Na} (eq 14) in which the Na normalization removes differences in W^X_{river} that arise from short-term fluctuations in runoff. Because Na behaves conservatively in the Critical Zone (that is, negligible incorporation into secondary solids and minimal uptake into non-halophilic and non-C4/CAM plants (Marschner and Marschner, 2012)), the DEE^X_{Na} metric is essentially a measure of the difference between the X/Na ratio in river water and that predicted based on loss from regolith. After correcting W^X_{river} (including Na) for non-silicate inputs, DEE^X_{Na} is still consistently below 1 for Si, Mg, Ba, Li, P, Rb, and Zn in Sierra Nevada. For Sri Lanka, where dry and wet deposition inputs contribute to a large extent to the ecosystem's nutrient budget, "total" DEE^X_{Na} is below 1 for Si, Ba, P, and Zn.

We also evaluated whether the use of Na as a normalizing element might introduce a bias if the rate of Na solubilization relative to other elements has varied over the time scale of the regolith residence time. If this were the case, the ratio $\left(\tau^X_{Zr}\right)/\left(\tau^{Na}_{Zr}\right)$ at a given point in regolith may vary with time. For example, this could be induced by glacial-interglacial climate cycles that induce time-variant dissolution of the Na-rich plagioclase that delivers most of the Na. We regard this explanation as unlikely since this would require that a) the relative differences between mineral dissolution rate constants depend substantially on climate, and b) the cyclicity of a perturbation is of a similar time scale as regolith residence time. As further support for the lack of transient effects, we note that for a number of elements DEE^X_{Na} agrees with DEE^X in Sierra Nevada (Uhlig and others, 2017) and Sri Lanka (Schuessler and others, 2018). We thus conclude that causes other than a lack of steady state contribute to the imbalance.

3) Element fractionation along hillslopes or at depth.—An apparent missing elemental flux may be an indicator for a genuine characteristic of weathering zones, namely that the regolith weathering is heterogeneous at the hillslope scale and the sites chosen for either regolith or solute chemistry sampling did not reflect a representative average of this heterogeneity. For example, Riebe and others(2017) have reviewed the hypothesis that subsurface flow paths and erosion cause weathering zone thicknesses – and thus weathering intensities, captured in *CDF* or τ_{Zr}^{X} – to differ along hillslopes. Conceptually, the weathering zone is predicted to be thinner and less weathered near the channel than near ridges. As a result, elemental depletion determined upslope or on ridge profiles might differ from the dissolved export that integrates different portions of the landscape. Indeed, mathematical formulations of hillslope weathering show that geochemical mass balances using mobile soil samples can overestimate weathering rates by neglecting downslope transport of material altered upslope (Yoo and others, 2007). Empirical data, including from the Alps site, confirm that $W_{regolith}$ varies with altitude and hillslope position (Norton and von Blanckenburg, 2010). However, we note that while this explanation might influence the non-sodium normalized metric DEE^{X} (eq 13, which relies on the extrapolation of representative soil-pit specific chemistry and regolith production rates to the catchment scale), the simplified form of DEE_{Na}^{X} does not involve any rate terms (eq 14*) nor even an assumption of a consistent degree of chemical depletion $\left(\tau_{Zr}^{X}\right)$ across a hillslope. Instead, the inherent assumption is that the ratio $\left(\tau_{Zr}^{X}\right)/\left(\tau_{Zr}^{Na}\right)$ does not vary systematically across hillslopes, such that by sampling for example, mostly ridgetops (the Alps) or hillslopes (Sri Lanka) we do not induce an artificial bias. The validity of this assumption is supported by measurements of soil chemistry across catenas in the Susquehanna Shale Hills CZO (Hasenmueller and others, 2017), along catenas on granitic rock in South Africa (Khomo and others, 2013), and at the summits and footslopes of catchments at the granitic Catalina CZO (Lybrand and Rasmussen, 2014). At these sites, absolute values of τ_{Zr}^{X} do vary spatially – both laterally and vertically - but the ratio $\left(\tau_{Zr}^{X}\right)/\left(\tau_{Zr}^{Na}\right)$ does not systematically vary along any of the catenas, lending confidence to our use of DEE_{Na}^{X} (eq 14). There is of course unavoidable uncertainty that arises from landscape-scale heterogeneity; this is propagated into the uncertainties on the DEE_{Na}^{X} values. We do not regard these explanations to be the origin for the systematic bias we observe and thus proceed to evaluate what we consider to be the most likely: a hidden pool or pathway.

4) A hidden pathway or pool.—What we mean with this notion is a genuine, systematic Critical Zone process, the nature of which entails that the corresponding river fluxes of the concerned elements are systematically reduced compared to expectations derived from the regolith chemistry. We will argue below from elemental and stable isotope mass balances that at our sites this process takes place “outside” of the regolith, but before elements enter the dissolved pool ('dissolved” as defined operationally by the filtration scheme adopted for this study, that is < 0.2 µm in size).

A first “hidden pathway” might exist in the form of an “un-sampled” dissolved flux for elements that exhibit a positive slope in concentration discharge (C-Q) diagrams. These include Al, Ti, Fe, and the REE (Trostle and others, 2016; Kim and others, 2018). For these elements, an underestimate of W_{river}^{X} and DEE^{X} could result from the observation that their stream dissolved concentrations typically increase at high discharge (Trostle and others, 2016), unlike most major elements that exhibit either constant (‘chemostatic') concentrations or slight dilution with increasing runoff. By not sampling these extreme events at sufficient sampling resolution, a large fraction of the dissolved flux can be missed. Stille and others(2006) were among the first to observe a deficit, in this case for the light rare earth elements that are enriched in plants, and attributed their hosting pool to be organic matter in the A-horizon and their export to be restricted to rare events of high flow. It is thus noteworthy that elements with positive C-Q slopes are often those appearing in colloidal form (Trostle and others, 2016) or together with dissolved organic carbon when flushed from soils (Zhi and others, 2019). Of the elements for which we detected a low DEE_{Na}^{X}, Al and Ba might be subject to this pathway (fig. 12, Data table C5), and possibly also P because of its preferred colloidal form (Gottselig and others, 2017; Gottselig and others, 2019). However, these explanations are unlikely to hold for the metals like Ca, Mg and Sr that do not appear in colloidal form and usually feature negative or chemostatic C-Q relationships (Godsey and others, 2019).

We therefore consider whether biological processes are a possible explanation for the systematic observation that $DEE_{Na}^{X} < 1$ for these elements, since these metals often have well defined biochemical roles. We suggest that uptake from soil water into plant organs and removal by erosion is a likely mechanism. The hidden flux can thus be explained by incorporation of an element into the body of plants, whilst at the same time preventing its return into the dissolved pool by recycling. What would be the plant pool containing this complementary elemental compartment? In the pre-human period or in pristine settings, this could be erosion of plant litter and woody debris, or ash exported by wind after fires. Megafauna (Schoelynck and others, 2019) or herbivory in general (Borer and others, 2020) represent another potential element transport vector. In mountain landscapes it could be woody debris, of which a significant portion can be eroded and stored (Wohl and others, 2012; Turowski and others, 2016). Additional explanations that are not mutually exclusive but are unique to anthropogenically impacted settings include wood export by logging or crop harvest (Vandevenne and others, 2012), or the export of nutrients in grazing animals' excrement. In fact, similar imbalances between predicted regolith weathering fluxes and observed riverine export are observed at 12 large forest-covered areas in North America that are used for intense timber production (de Oliveira Garcia and others, 2018). There, the elemental imbalances increased with ecosystem demand. On average, 17, 20, 16, and 94 % of Ca, K, Mg, and P, respectively, was lost (de Oliveira Garcia and others, 2018), comparable with our estimates from DEE^{X}. In that case logging was invoked as the cause of the so-called 'negative nutrient budget'. A condition for this export pathway to explain DEE_{Na}^{X} values below 1 is that their absolute DEE^{X} is at least matched by uptake of this element U^{X} (Data table C5). This is the case for the plant-essential elements Mg, Ca, K, and P and also the case for the plant beneficial element Si, as discussed in our companion paper (Frings and others, 2021b). In the case of Si, estimates of plant uptake (U^{Si}) are very similar to the deficit observed between regolith Si loss and stream Si export. The face-value implication is that a large fraction of plant silica, likely in the form of phytoliths, is eroded rather than recycled or stored in soils. This is corroborated by a Ge/Si-δ^{30}Si mass balance model Frings and others, 2021b), which is independent of fluxes and relies only on element and isotope ratios. This model showed that the export of biomass Si is of the same order of magnitude as dissolved Si. For Si, another possibility is that very fine Si-oxide particles are leaving the weathering zone several meters beneath the surface (Kim and others, 2018) and go undetected as they are removed by filtration (see above; scenario 1).

The suggestion that $DEE_{Na}^{X} < 1$ is the expression of a genuine phenomenon (scenario 4 above) requires support from a tool that is insensitive to the potential biases discussed (scenarios 1 to 3 above). One such tool is a graphical analysis that shows how a loss in one part of the system shows up as an excess in another. In figure 13 a set of X/Na ratios are plotted against each other, assuming Na is conservative once solubilised from rock, and not part of the "hidden" flux or pool. X is a less soluble element that is prone to be partitioned into the "hidden" flux or pool, be that by colloid partitioning or by bio-uptake. In this figure, X/Na ratios are normalized to the parent rock ratios, to represent data from different sites on the same scale; and presented in logarithmic scale in order to enable a graphical representation of the parameters of

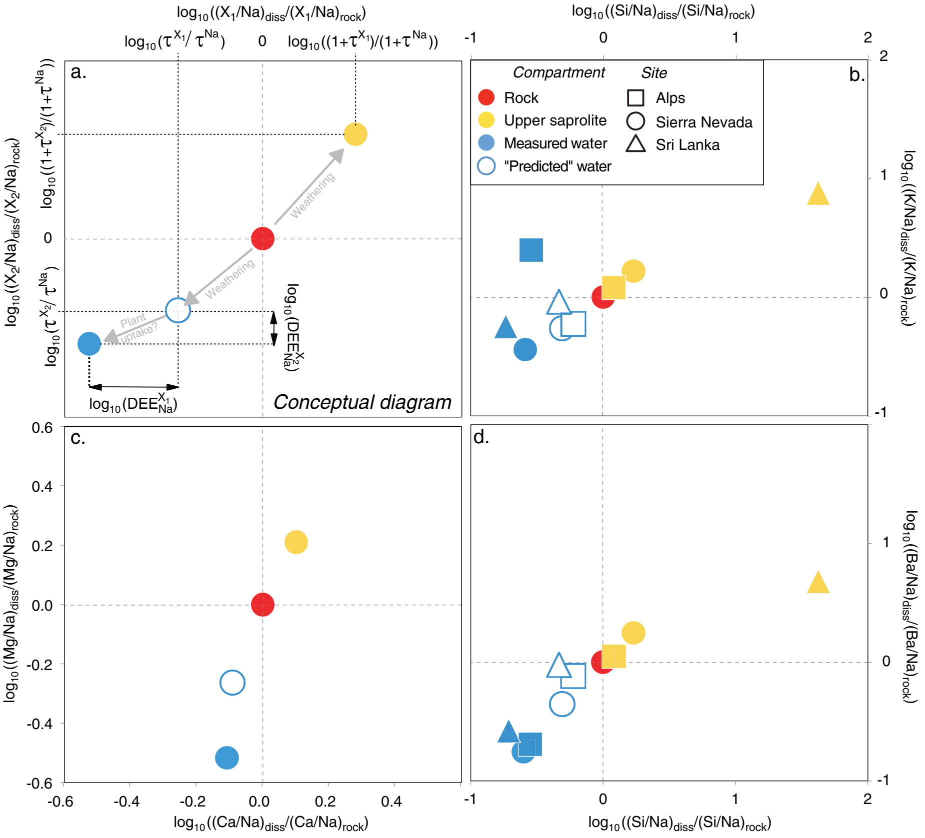

Fig. 13. Graphical representation of the combined effects of net weathering loss (mineral dissolution minus secondary phase precipitation, quantified by τ^X) and additional partitioning of elements into a "hidden" sink and quantified by the new metric DEE^X_{Na}. a) Conceptual diagram where X/Na of Critical Zone compartments are normalized to the source rock X/Na ratio for comparison of data from different sites on the same scale and logged to enable a graphical representation of DEE^X_{Na}. By definition, the rock lies at the origin. Residual solids remaining after weathering (best represented by the upper saprolite) are most depleted in Na and less depleted in the less soluble elements (Mg, Ca, K, Ba, or Si), shifting them into the upper-right quadrant. The ratio between the X/Na ratios of the weathering solid residual and the source rock is equal to $(1+\tau^X)/(1+\tau^{Na})$ (see derivation in Appendix 1). The predicted composition of the complementary load exported by water from the weathering zone lies in the lower-left, that is, enriched in Na over the less soluble elements and should be offset from the origin by τ^X/τ^{Na}. The actual (measured) composition of water is displaced from the "predicted" water composition by the DEE^X_{Na} (see derivation in Appendix 1). DEE^X_{Na} thus quantifies element partitioning into "hidden" solid compartments not contained in dissolved river water or upper saprolite. Panels b-d show Na-normalized concentrations for the three sites; b) Si *versus* K; c) Mg *versus* Ca (shown only for Sierra Nevada, since uncertainties from the carbonate correction are too high in the Alps and Sri Lanka); d) Ba *versus* Si. An offset between 'predicted' and observed water composition (that is, $DEE^X_{Na} < 1$) is observed for Mg in Sierra Nevada, K in the Alps, and Ba and Si at all three study sites; of which all elements have well defined biological roles.

DEE^X_{Na}. The coordinate of the most weathered material is equal to $(1+\tau^X)/(1+\tau^{Na})$ (see derivation in Appendix). This treatment allows us to determine where the water chemical composition deriving from this weathering should plot, provided that the partitioning into the missing flux of this element was absent: the coordinate of this "predicted water" is equal to τ^X/τ^{Na}. The difference between "predicted water" and the actual water exported from the weathering zone is a graphical representation of

DEE^X_{Na}. A depletion of the actual river water in missing elements with respect to Na relative to the "predicted" water" strongly suggests that this difference is due to incorporation into such pool. At our sites, such a difference is observed for Mg in Sierra Nevada, K in the Alps, and Ba and Si at all three sites (fig. 13), consistent with our DEE^X_{Na} calculations (fig. 12).

Another tool is found in the ratios of metal stable isotopes. Along our erodosequence, the average isotope ratio of dissolved elements being exported from the weathering zone is not equal to that of the bedrock. This is not surprising in itself: differences in isotope ratios between an element contained in rock and that in the solute released from this rock often emerge in the weathering zone due to isotope fractionation during weathering and bio-cycling. However, the mass balance assuming that a weathering rock is partitioned into soil that is eroded as river sediment and the complementary dissolved load is often not fulfilled. Expressing this imbalance as a mixing equation we get:

$$\delta_{rock} \neq f\delta_{diss} + (1-f)\delta_{soil} \tag{16}$$

where δ is the conventional isotope ratio notation that denotes deviation in permil from the isotope ratio of a reference material, f is the fraction of element X exported as solute, and the subscripts 'diss' and 'soil' refer to dissolved and topsoil, respectively, the measurements of which implicitly include dust inputs, if present. We can obtain an estimate of f from τ^X_{Zr}. Expressed in words, the mean isotope ratio of solute and topsoil, weighted by $-\tau^X_{Zr}$ and $\left(1+\tau^X_{Zr}\right)$, respectively, is often not equal to parent material. Bouchez and others (2013) show how a normalized dissolved element export flux can be defined based on isotope ratios alone:

$$w^X_{isotope} = \frac{\delta^X_{soil} - \delta^X_{rock}}{\delta^X_{soil} - \delta^X_{diss}} \tag{17}$$

where the lower case $w^X_{isotope}$ implies the weathering flux (including dust, if present) normalized to elemental regolith production (eq 3). This requires no knowledge of fractionation factors but does assume steady state mass balance. Since the equivalent normalized flux for $W^X_{regolith}$ is $W^X_{regolith}/RP^X = -\tau^X_{Zr}$, then the isotopic manifestation of the DEE phenomenon can be quantified as:

$$DEE^X_{isotope} = {}^{w^X_{isotope}}\Big/_{-\tau^X_{Zr}} \tag{18}$$

This is an isotopic expression of DEE^X_{Na} differing from unity, and is a feature we observe at these sites for Mg stable isotopes (Uhlig and others, 2017), Si stable isotopes (Frings and others, 2021a), Sr stable isotopes (Bouchez and von Blanckenburg, 2021), and the Ge/Si 'pseudoisotope' ratio (Frings and others, 2021b), and at sites comprising a vegetation gradient in Chile where $DEE^{Sr}_{isotope}$ correlates with bulk soil erosion rate (Oeser and von Blanckenburg, 2020b). Assuming that isotope fractionation during mineral dissolution is absent (a reasonable assumption beyond the time scale of "incipient weathering") the two important processes that generate differences in isotope ratios between fluids and solids (Bouchez and others, 2013) are fractionation during incorporation into secondary materials, and uptake of elements into pants.

For Mg, Ca, and Sr isotope ratio differences between river solutes and regolith (assumed to be representative of bulk sediment exported by rivers) have been reported (for example, $^{88}Sr/^{86}Sr$ (Andrews and others, 2016, Oeser and von Blanckenburg, 2020b), $^{26}Mg/^{24}Mg$ (Uhlig and others, 2017), and $^{44}Ca/^{40}Ca$ (Lehn and others, 2017) and for these specific studies these differences cannot be explained by secondary solid formation, since the phases forming at these sites do not incorporate Mg, Ca or Sr to an appreciable extent. Yet these elements are bio-essential. The separation of these isotope compartments can thus be explained by incorporation of an isotopically fractionated mass into the body of plants, whilst at the same time preventing its return into the dissolved pool by recycling.

General Significance of the Erodosequence Approach

Our 'erodosequence' and the methods we combine in novel ways provide important mechanistic information about chemical weathering and nutrient cycling in settings whose distinct difference is primarily erosion rate. In fast eroding mountains the majority of the weathering flux is generated in those parts of the landscape that are covered by soil that is eroding at slower rates than the mountain range. We have also shown that, provided the steady-state assumption embedded into the erodosequence approach is valid over the integration time scales of the weathering zone, powerful metrics for nutrient recycling and for potential export or net storage of elements contained in plant litter can be easily derived. However, we also caution that for sites experiencing non-negligible atmospheric inputs (whether wet or dry depositional fluxes), careful accounting of the non-regolith element sources is a prerequisite to the accuracy of these metrics.

In terms of ecosystem nutrition, our erosion-rate driven gradients show characteristics similar to those found in the chronosequence approach, that differ in the degree of regolith depletion. For example, old, climatically buffered, infertile landscapes (OCBILS) or those with high plant diversity and strong nutrient recycling differ from lower diversity ecosystems commonly found in young, frequently disturbed, fertile landscapes (YODFELs) (Lambers and others, 2008). It was suggested that these differences in plant diversity are set by phosphorus availability (Laliberte and others, 2013). These predictions are opposite to those by Shakespeare (in Henry IV): "Best is the fattest soil to weeds".

Regarding weathering and the operation of the global thermostat via CO_2 drawdown, an important consequence is that ecosystems have the ability to buffer mineral nutrient uptake via recycling, and thus weathering rate is not a straightforward function of primary production (Uhlig and von Blanckenburg, 2019; Oeser and von Blanckenburg, 2020a). More specifically, plant growth may not necessarily accelerate rock weathering as suggested in models and syntheses of weathering throughout Earth's history (Berner and others, 2003, Pagani and others, 2009). Rather, there may be many subtle ways including positive as well as negative feedbacks in which traits of plants and associated soil microbiota shape the weathering zone and control element fluxes. We hope that the suite of new metrics introduced in this study, and associated isotope studies, will eventually allow us to pinpoint these interactions in novel ways.

A criticism of this approach could be that our "erodosequence" approach is subject to confounding factors. For example, bedrock properties are similar but not identical, and climate (and thus vegetation) also differs between sites. Thus the "erodosequence" contains components of a "climosequence" (for example, Egli and others, 2003; Ferrier and others, 2012; Oeser and others, 2018). Another criticism could be that even if steady state is attained in weathering zone thickness, some properties of the Critical Zone may fluctuate at much shorter time scales, by, for example, species invasion, such that weathering fluxes and bio-uptake fluxes are partially decoupled on observational time scales. Finally, the apparent observation of systematic flux imbalances, expressed as dissolved export efficiencies < 1, is the first of its kind. Whether it is due to a hitherto unidentified bias, or even if the observation is valid elsewhere, requires further field testing. Nevertheless, the independent stable isotope partitioning studies that hint at the same effect lend support to the interpretation that plant biomass erosion plays a widespread and important role in Critical Zone element budgets.

Implications for Critical Zone Metal Isotope Geochemistry

Stable isotope ratios of metals and metalloids like Li, B, Mg, Si, Fe, Cu, Zn, Sr, Mo, Ba, U have recently emerged as proxies for aspects of the weathering process. They might also record weathering in the past, when extracted from the sedimentary record (Frings, 2019). In general, these isotope ratios trace processes in the Critical Zone such as (1) the formation of secondary phases during (Frings and others, 2016), or (2) biological cycling (Opfergelt and Delmelle, 2012; Bullen and Chadwick, 2016; Uhlig and others, 2017). These tools do not trace absolute rates, but rather the relative magnitude of these fluxes relative to element (Bouchez and others, 2013). An important point is that a difference in isotope ratios between source rock and exported solutes for metals that are not incorporated into pedogenic clays or oxides can develop only if some fraction of plant biomass containing that element escapes re-dissolution and is exported or stored as solid plant debris. Indeed, the companion papers to this publication, that rely on the same sample set and background data as presented here, contain examples of this point. For example, the companion papers show how Ge/Si ratios in conjunction with Si isotope data can be incorporated into a Si mass-balance model which requires that the export of secondary, fractionated solids (largely clays and plant material) becomes increasingly important at shorter regolith residence times (80 % of initially solubilized Si in the rapidly eroding Alps sites *versus* 32 % in the slowly eroding Sri Lanka site). The mass-balance also shows that plant material is a surprisingly large contributor to Si export from these catchments (Frings and others, 2021a, 2021b). Along the same lines, stable $^{88}Sr/^{86}Sr$ ratios (Bouchez and von Blanckenburg, 2021) from these samples show that in the Alps, one third of Sr solubilized from regolith is directly drained to aquifers and streams without experiencing any biological cycling. Two thirds of this Sr are taken up by plants and is exported in its entirety as particulate organic debris, in line with the *DEE*-based interpretation reported here. In the Sierra Nevada plants take up the entirety of the Sr solubilized from regolith and re-release it wholesale into stream discharge. In Sri Lanka, despite intense recycling a significant fraction of Sr in litter still remains refractory to re-dissolution and is exported in organic debris.

Nevertheless, a quantitative interpretation of these isotope data, and their use in inferring scenarios of Earth's surface evolution (Misra and Froelich, 2012; Pogge von Strandmann and others, 2013; Caves and others, 2019) requires knowledge of how the isotope ratios respond to the controlling tectonic, climatic and biological factors. We still lack systematic observations of isotope variations across a large range of denudation rates and thus the “weathering intensity” that controls the manifestation of isotope fractionation between regolith and fluid (Dellinger and others, 2015). The erodosequence presented in this study, and the associated gradient in elemental fluxes between different Critical Zone compartments, provides the necessary framework to calibrate these isotope systems.

ACKNOWLEDGMENTS

We are grateful to the Southern Sierra Nevada Critical Zone Observatory for field support, Jutta Schlegel and Josi Holtz for support of measurements and laboratory maintenance, and to three anonymous reviewers for their careful and constructive comments. This study was funded by GFZ Potsdam and the Helmholtz Laboratory for the Geochemistry of the Earth Surface (HELGES) by the the Helmholtz Association of German Research Centers.

APPENDIX

GRAPHICAL ANALYSIS OF THE DISSOLVED EXPORT EFFICIENCY (DEE^{X}_{NA}) AND THE MASS TRANSFER COEFFICIENT (τ^{X})

We used Na-normalized element concentrations (X/Na) in both End Member Mixing Analysis (EMMA) (Appendix S2, fig. S2) and to represent the effect of weathering and biological uptake on the various compartments of the Critical Zone as denoted by the DEE^{X} (fig. 13). Here we show a derivation for a graphical representation of the mass transfer coefficient τ^{X} (eq 5) and the dissolved export efficiency DEE^{X}_{Na} (eq 14) in X/Na diagrams. Introducing X/Na ratios into the definition of τ^{X} in equation (5) (the subscript "*Zr*" is omitted here for the sake of clarity):

$$\tau^{X}+1=\frac{\left(\frac{X}{Zr}\right)_{weathered}}{\left(\frac{X}{Zr}\right)_{rock}}=\frac{\left(\frac{X}{Na}\right)_{weathered}}{\left(\frac{X}{Na}\right)_{rock}}\times\frac{\left(\frac{Na}{Zr}\right)_{weathered}}{\left(\frac{Na}{Zr}\right)_{rock}} \tag{A1}$$

Because the term $\frac{(Na/Zr)_{weathered}}{(Na/Zr)_{rock}}$ is equal to $\tau^{Na}+1$ (from eq 5 when X = Na), it follows:

$$\frac{\left(\frac{X}{Na}\right)_{weathered}}{\left(\frac{X}{Na}\right)_{rock}}=\frac{\tau^{X}+1}{\tau^{Na}+1} \tag{A2}$$

This allows us to plot the position of the solid weathered component (taken here as the uppermost saprolite) in a X/Na diagram normalized to the parent rock X/Na ratio (such that sites with different bedrock chemistry can be displayed simultaneously). The coordinate of the weathered component along the X/Na-axis is thus equal to $\frac{\tau^{X}+1}{\tau^{Na}+1}$.

The same approach can be followed to derive a "predicted" water component - the dissolved counterpart to the solid weathered component. By definition, the relative amount of element X lost to solution during weathering is $-\tau^{X}$, such that the X/Na ratio of the dissolved load resulting from weathering should be:

$$\left(\frac{X}{Na}\right)_{predicted\ water}=\left(\frac{X}{Na}\right)_{rock}\times\left(\frac{\tau^{X}}{\tau^{Na}}\right) \tag{A3}$$

From which it follows that:

$$\frac{\left(\frac{X}{Na}\right)_{predicted\ water}}{\left(\frac{X}{Na}\right)_{rock}}=\frac{\tau^{X}}{\tau^{Na}} \tag{A4}$$

The coordinate of the predicted water end member along the X/Na-axis in the diagram is therefore equal to $\frac{\tau^{X}}{\tau^{Na}}$.

Finally, DEE^{X}_{Na} emerges from the difference between the predicted water and the measured water. Recalling the definition of DEE^{X}_{Na} from equation (14) and using equation (A4):

$$DEE^{X}_{Na}=\frac{\frac{\left(\frac{X}{Na}\right)_{water}}{\left(\frac{X}{Na}\right)_{rock}}}{\frac{\tau^{X}}{\tau^{Na}}}=\frac{\frac{\left(\frac{X}{Na}\right)_{water}}{\left(\frac{X}{Na}\right)_{rock}}}{\frac{\left(\frac{X}{Na}\right)_{predicted\ water}}{\left(\frac{X}{Na}\right)_{rock}}}=\frac{\left(\frac{X}{Na}\right)_{water}}{\left(\frac{X}{Na}\right)_{predicted\ water}} \tag{A5}$$

DEE_{Na}^{X} is therefore equal to the ratio between the X/Na ratio of the measured water and the X/Na ratio of the water composition predicted from the comparison between the rock and the weathered solid. Representing this ratio graphically as an offset along the X/Na-axis is best achieved by logging both sides of equation (A5):

$$log_{10}\left(DEE_{Na}^{X}\right) = log_{10}\left(\frac{\left(\frac{X}{Na}\right)_{water}}{\left(\frac{X}{Na}\right)_{rock}}\right) - log_{10}\left(\frac{\left(\frac{X}{Na}\right)_{predicted\ water}}{\left(\frac{X}{Na}\right)_{rock}}\right) \tag{A6}$$

The magnitude of DEE_{Na}^{X} can therefore be evaluated graphically for two elements (two X's) in a log-log plot of X/Na ratios as the difference between the position of the measured and predicted water components. In such a diagram, the position of the weathered solids and of the predicted waters are given by (from eqs A2 and A4):

$$log_{10}\left(\frac{\tau^{X}+1}{\tau^{Na}+1}\right) = log_{10}\left(\frac{\left(\frac{X}{Na}\right)_{weathered}}{\left(\frac{X}{Na}\right)_{rock}}\right) \tag{A7}$$

$$log_{10}\left(\frac{\tau^{X}}{\tau^{Na}}\right) = log_{10}\left(\frac{\left(\frac{X}{Na}\right)_{predicted\ water}}{\left(\frac{X}{Na}\right)_{rock}}\right) \tag{A8}$$

SUPPLEMENTARY DATA LINKED TO THIS PUBLICATION

http://earth.eps.yale.edu/%7eajs/SupplementaryData/2021/vonBlanckenburg

von Blanckenburg, F., Schuessler, J. A., Bouchez, J., Frings, P. J., Uhlig, D., Oelze, M., Frick, D. A., Hewawasam, T., Dixon, J. E., and Norton, K., 2021, Geochemical data on rock weathering in a global erodosequence: GFZ Data Services, v. doi.org/10.5880/GFZ.3.3.2021.001

Part 1:

- Table A1. Swiss Alps analyses of soil, saprolite, rock
- Table A2. Swiss Alps analyses of water samples
- Table A3. Swiss Alps analyses of plant samples from the Swiss Alps
- Table SN1. Sierra Nevada analyses of soil, saprolite, rock
- Table SN2. Sierra Nevada analyses of water samples
- Table SN3. Sierra Nevada analyses of plant samples
- Table SL1. Sri Lanka analyses of soil, saprolite, rock
- Table SL2. Sri Lanka analyses of water samples. Element concentration analyses and pH
- Table SL3. Sri Lanka analyses of plant samples
- Table C1. Summary of principle site characteristics
- Table C2. Compilation of Denudation rates from river cosmogenic nuclides in river sediment and soil associated production rates
- Table C3. Compilation of soil production rates, CDF, and chemical weathering rates
- Table C4. Fractional contributions of endmembers from a inversion of dissolved elements in streams
- Table C5. Flux Summary: Plant uptake rates, recycling ratios, and dissolved export efficiency
- Table C6. Data quality control for plant concentration analyses

Part 2:

1. Sources of River Solutes from End Member Mixing Analysis (EMMA)
2. Re-assessment of dust input in the Sierra Nevada
3. Rock and Regolith Mineralogical Composition from X-Ray Diffraction (XRD)

REFERENCES

Aarons, S. M., Arvin, L. J., Aciego, S. M., Riebe, C. S., Johnson, K. R., Blakowski, M. A., Koornneef, J. M., Hart, S. C., Barnes, M. E., Dove, N., Botthoff, J. K., Maltz, M., and Aronson, E. L., 2019, Competing droughts affect dust delivery to Sierra Nevada: Aeolian Research, v. 41, p. 100545, https://doi.org/10.1016/j.aeolia.2019.100545

Aciego, S. M., Riebe, C. S., Hart, S. C., Blakowski, M. A., Carey, C. J., Aarons, S. M., Dove, N. C., Botthoff, J. K., Sims, K. W., and Aronson, E. L., 2017, Dust outpaces bedrock in nutrient supply to montane forest ecosystems: Nat Commun, v. 8, p. 14800, https://doi.org/10.1038/ncomms14800

Amundson, R., Richter, D. D., Humphreys, G. S., Jobbagy, E. G., and Gaillardet, J., 2007, Coupling between Biota and Earth Materials in the Critical Zone: Elements, v. 3, p. 327–332, https://doi.org/10.2113/gselements.3.5.327

Andrews, M. G., Jacobson, A. D., Lehn, G. O., Horton, T. W., and Craw, D., 2016, Radiogenic and stable Sr isotope ratios (87 Sr/ 86 Sr, δ 88/86 Sr) as tracers of riverine cation sources and biogeochemical cycling in the Milford Sound region of Fiordland, New Zealand: Geochimica et Cosmochimica Acta, v. 173, p. 284–303, https://doi.org/10.1016/j.gca.2015.10.005

Arvin, L. J., Riebe, C. S., Aciego, S. M., and Blakowski, M. A., 2017, Global patterns of dust and bedrock nutrient supply to montane ecosystems: Science Advances, v. 3, p. eaao1588, https://doi.org/10.1126/sciadv.aao1588

Bales, R. C., Hopmans, J. W., O'Geen, A. T., Meadows, M., Hartsough, P. C., Kirchner, P., Hunsaker, C. T., and Beaudette, D., 2011, Soil Moisture Response to Snowmelt and Rainfall in a Sierra Nevada Mixed-Conifer Forest: Vadose Zone Journal, v. 10, p. 786–799, https://doi.org/10.2136/vzj2011.0001

Balogh-Brunstad, Z., Kent Keller, C., Thomas Dickinson, J., Stevens, F., Li, C. Y., and Bormann, B. T., 2008, Biotite weathering and nutrient uptake by ectomycorrhizal fungus, Suillus tomentosus, in liquid-culture experiments: Geochimica et Cosmochimica Acta, v. 72, n. 11, p. 2601–2618, https://doi.org/10.1016/j.gca.2008.04.003

Bateman, P. C., and Wones, D. R., 1972, Huntington Lake Quadrangle, central Sierra Nevada, California; analytic data: Professional Paper, https://doi.org/10.3133/pp724A

Bazilevskaya, E., Lebedeva, M., Pavich, M., Rother, G., Parkinson, D. Y., Cole, D., and Brantley, S. L., 2012, Where fast weathering creates thin regolith and slow weathering creates thick regolith: Earth Surface Processes and Landforms, v. 38, n. 8, p. 847–858, https://doi.org/10.1002/esp.3369

Behrens, R., Bouchez, J., Schuessler, J. A., Dultz, S., Hewawasam, T., and von Blanckenburg, F., 2015, Mineralogical transformations set slow weathering rates in low-porosity metamorphic bedrock on mountain slopes in a tropical climate: Chemical Geology, v. 411, p. 283–298, https://doi.org/10.1016/j.chemgeo.2015.07.008

Behrens, R., Wirth, R., and von Blanckenburg, F., 2021, Rate limitations of nano-scale weathering front advance in the slow-eroding Sri Lankan Highlands: Geochimica et Cosmochimica Acta, https://doi.org/10.1016/j.gca.2021.06.003

Bernasconi, S. M., Bauder, A., Bourdon, B., Brunner, I., Bunemann, E., Christl, I., Derungs, N., Edwards, P., Farinotti, D., Frey, B., Frossard, E., Furrer, G., Gierga, M., Göransson, H., Gülland, K., Hagedorn, F., Hajdas, I., Hindshaw, R., Ivy-Ochs, S., Jansa, J., Jonas, T., Kiczka, M., Kretzschmar, R., Lemarchand, E., Luster, J., Magnusson, J., Mitchell, E. A. D., Venterink, H. O., Plötze, M., Reynolds, B., Smittenberg, R. H., Stahli, M., Tamburini, F., Tipper, E. T., Wacker, L., Welc, M., Wiederhold, J. G., Zeyer, J., Zimmermann, S., and Zumsteg, A., 2011, Chemical and Biological Gradients along the Damma Glacier Soil Chronosequence, Switzerland: Vadose Zone Journal, v. 10, p. 867–883, https://doi.org/10.2136/vzj2010.0129

Berner, R., Lasaga, A. C., and Garrels, R., 1983, The carbonate-silicate geochemical sycle and its effect on atmospheric carbon dioxide over the past 100 million years: American Journal of Science, v. 283, p. 641–683, https://doi.org/10.2475/ajs.283.7.641

Berner, E. K., Berner, R. A., and Moulton, K. L., 2003, Plants and Mineral Weathering: Present and Past, in Holland, H. D., and Turekian, K. K., editors, Treatise on Geochemistry: Amsterdam, Kidlington, Waltham, Elsevier, p. 169–188, https://doi.org/10.1016/B0-08-043751-6/05175-6

Birks, H. H., and Birks, H. J. B., 2004, The rise and fall of forests: Science, v. 305, n. 5683, p. 484–485, https://doi.org/10.1126/science.1101357

Blum, J. D., and Erel, Y., 1997, Rb-Sr isotope systematics of a granitic soil chronosequence: The importance of biotite weathering: Geochimica et Cosmochimica Acta, v. 61, p. 3193–3204, https://doi.org/10.1016/S0016-7037(97)00148-8

Borer, E. T., Harpole, W. S., Adler, P. B., Arnillas, C. A., Bugalho, M. N., Cadotte, M. W., Caldeira, M. C., Campana, S., Dickman, C. R., Dickson, T. L., Donohue, I., Eskelinen, A., Firn, J. L., Graff, P., Gruner, D. S., Heckman, R. W., Koltz, A. M., Komatsu, K. J., Lannes, L. S., MacDougall, A. S., Martina, J. P., Moore, J. L., Mortensen, B., Ochoa-Hueso, R., Olde Venterink, H., Power, S. A., Price, J. N., Risch, A. C., Sankaran, M., Schutz, M., Sitters, J., Stevens, C. J., Virtanen, R., Wilfahrt, P. A., and Seabloom, E. W., 2020, Nutrients cause grassland biomass to outpace herbivory: Nat Commun, v. 11, p. 6036, https://doi.org/10.1038/s41467-020-19870-y

Bouchez, J., and Gaillardet, J., 2014, How accurate are rivers as gauges of chemical denudation of the Earth surface?: geology, v. 42, p. 171–174, https://doi.org/10.1130/G34934.1

Bouchez, J., and von Blanckenburg, F., 2021, The role of vegetation in setting strontium stable isotope ratios in the Critical Zone: American Journal of Science, v. 321, n. 8, p. 1246–1283, https://doi.org/10.24.75/08.2021.04

Bouchez, J., von Blanckenburg, F., and Schuessler, J. A., 2013, Modeling novel stable isotope ratios in the weathering zone: American Journal of Science, v. 313, p. 267-308, https://doi.org/10.2475/04.2013.01

Brantley, S. L., and Lebedeva, M., 2011, Learning to Read the Chemistry of Regolith to Understand the Critical Zone: Annual Review of Earth and Planetary Sciences, v. 39, p. 387–416, https://doi.org/10.1146/annurev-earth-040809-152321

Brantley, S. L., Megonigal, J. P., Scatena, F. N., Balogh-Brunstad, Z., Barnes, R. T., Bruns, M. A., Van Cappellen, P., Dontsova, K., Hartnett, H. E., Hartshorn, A. S., Heimsath, A., Herndon, E., Jin, L., Keller, C. K., Leake, J. R., McDowell, W. H., Meinzer, F. C., Mozdzer, T. J., Petsch, S., Pett-Ridge, J., Pregitzer, K. S., Raymond, P. A., Riebe, C. S., Shumaker, K., Sutton-Grier, A., Walter, R., and Yoo, K., 2011, Twelve testable hypotheses on the geobiology of weathering: Geobiology, v. 9, p. 140–65, https://doi.org/10.1111/j.1472-4669.2010.00264.x

Brantley, S. L., DiBiase, R. A., Russo, T. A., Shi, Y., Lin, H., Davis, K. J., Kaye, M., Hill, L., Kaye, J., Eissenstat, D. M., Hoagland, B., Dere, A. L., Neal, A. L., Brubaker, K. M., and Arthur, D. K., 2016, Designing a suite of measurements to understand the critical zone: Earth Surface Dynamics, v. 4, p. 211–235, https://doi.org/10.5194/esurf-4-211-2016

Brooks, J. R., Barnard, H. R., Coulombe, R., and McDonnell, J. J., 2010, Ecohydrologic separation of water between trees and streams in a Mediterranean climate: Nature Geoscience, v. 3, p. 100–104, https://doi.org/10.1038/ngeo722

Buendía, C., Kleidon, A., and Porporato, A., 2010, The role of tectonic uplift, climate, and vegetation in the long-term terrestrial phosphorous cycle: Biogeosciences, v. 7, p. 2025–2038, https://doi.org/10.5194/bg-7-2025-2010

Bullen, T., and Chadwick, O., 2016, Ca, Sr and Ba stable isotopes reveal the fate of soil nutrients along a tropical climosequence in Hawaii: Chemical Geology, v. 422, p. 25–45, https://doi.org/10.1016/j.chemgeo.2015.12.008

Buss, H. L., Mathur, R., White, A. F., and Brantley, S. L., 2010, Phosphorus and iron cycling in deep saprolite, Luquillo Mountains, Puerto Rico: Chemical Geology, v. 269, p. 52–61, https://doi.org/10.1016/j.chemgeo.2009.08.001

Buss, H. L., Chapela Lara, M., Moore, O. W., Kurtz, A. C., Schulz, M. S., and White, A. F., 2017, Lithological influences on contemporary and long-term regolith weathering at the Luquillo Critical Zone Observatory: Geochimica et Cosmochimica Acta, v. 196, p. 224–251, https://doi.org/10.1016/j.gca.2016.09.038

Callahan, R. P., Ferrier, K. L., Dixon, J., Dosseto, A., Hahm, W. J., Jessup, B. S., Miller, S. N., Hunsaker, C. T., Johnson, D. W., and Sklar, L. S., 2019, Arrested development: Erosional equilibrium in the southern Sierra Nevada, California, maintained by feedbacks between channel incision and hillslope sediment production: GSA Bulletin, v. 131, p. 1179–1202, https://doi.org/10.1130/B35006.1

Caves, J. K., Jost, A. B., Lau, K. V., and Maher, K., 2016, Cenozoic carbon cycle imbalances and a variable weathering feedback: Earth and Planetary Science Letters, v. 450, p. 152-163, https://doi.org/10.1016/j.epsl.2016.06.035

Caves Rugenstein, J. K., Ibarra, D. E., and von Blanckenburg, F., 2019, Neogene cooling driven by land surface reactivity rather than increased weathering fluxes: Nature, v. 571, p. 99–102, https://doi.org/10.1038/s41586-019-1332-y

Chabaux, F., Blaes, E., Stille, P., Roupert, R. D., Pelt, E., Dosseto, A., Ma, L., Buss, H. L., and Brantley, S. L., 2013, Regolith formation rate from U-series nuclides: Implications from the study of a spheroidal weathering profile in the Rio Icacos watershed (Puerto Rico): Geochimica et Cosmochimica Acta, v. 100, p. 73–95, https://doi.org/10.1016/j.gca.2012.09.037

Chadwick, K. D., and Asner, G. P., 2016, Tropical soil nutrient distributions determined by biotic and hillslope processes: Biogeochemistry, v. 127, p. 273-289, https://doi.org/10.1007/s10533-015-0179-z

Chadwick, K. D., and Asner, G. P.2020, Geomorphic transience moderates topographic controls on tropical canopy foliar traits: Ecology Letter, v.23, n. 8, p.1276–1286, https://doi.org/10.1111/ele.13531

Chadwick, O. A., Brimhall, G. H., and Hendricks, D. M., 1990, From a black to a gray box - a mass balance interpretation of pedogenesis: Geomorphology, v. 3, p. 369–390, https://doi.org/10.1016/0169-555X(90)90012-F

Chadwick, O. A., Derry, L. A., Vitousek, P. M., Huebert, B. J., and Hedin, L. O., 1999, Changing sources of nutrients during four million years of ecosystem development: Nature, v. 397, p. 491-497, https://doi.org/10.1038/17276

Chapin, F. S., Matson, P. A., and Vitousek, P., 2011, Principles of Terrestrial Ecosystem Ecology, Springer, New York, https://doi.org/10.1007/978-1-4419-9504-9

Chaudhuri, S., Clauer, N., and Semhi, K., 2007, Plant decay as a major control of river dissolved potassium: A first estimate: Chemical Geology, v. 243, n. 1–2, p. 178–190, https://doi.org/10.1016/j.chemgeo.2007.05.023

Chorover, J., Kretzschmar, R., Garcia-Pichel, F., and Sparks, D. L., 2007, Soil biogeochemical processes within the Critical Zone: Elements, v. 3, n. 5, p. 321–326, https://doi.org/10.2113/gselements.3.5.321

Cleveland, C. C., Houlton, B. Z., Smith, W. K., Marklein, A. R., Reed, S. C., Parton, W., Del Grosso, S. J., and Running, S. W., 2013, Patterns of new versus recycled primary production in the terrestrial biosphere: Proceedings of the National Academy of Sciences of the United States of America, v. 110, p. 12733–12737, https://doi.org/10.1073/pnas.1302768110

Codilean, A. T., Munack, H., Cohen, T. J., Saktura, W. M., Gray, A., and Mudd, S. M., 2018, OCTOPUS: an open cosmogenic isotope and luminescence database: Earth System Science Data, v. 10, p. 2123–2139, https://doi.org/10.5194/essd-10-2123-2018

Cornelis, J. T., Ranger, J., Iserentant, A., and Delvaux, B., 2009, Tree species impact the terrestrial cycle of silicon through various uptakes: Biogeochemistry, v. 97, p. 231–245, https://doi.org/10.1007/s10533-009-9369-x

Dahlgren, R. A., Boettinger, J. L., Huntington, G. L., and Amundson, R. G., 1997, Soil development along an elevational transect in the western Sierra Nevada, California: Geoderma, v. 78, p. 207–236, https://doi.org/10.1016/S0016-7061(97)00034-7

Dellinger, M., Gaillardet, J., Bouchez, J., Calmels, D., Louvat, P., Dosseto, A., Gorge, C., Alanoca, L., and Maurice, L., 2015, Riverine Li isotope fractionation in the Amazon River basin controlled by the weathering regimes: Geochimica et Cosmochimica Acta, v. 164, p. 71–93, https://doi.org/10.1016/j.gca.2015.04.042

de Oliveira Garcia, W., Amann, T., and Hartmann, J., 2018, Increasing biomass demand enlarges negative forest nutrient budget areas in wood export regions: Scientific Reports, v. 8, p. 5280, https://doi.org/10.1038/s41598-018-22728-5

Dixon, J. L., and von Blanckenburg, F., 2012, Soils as pacemakers and limiters of global silicate weathering: Comptes Rendus Geoscience, v. 344, p. 597–609, https://doi.org/10.1016/j.crte.2012.10.012

Dixon, J. L., Heimsath, A. M., and Amundson, R., 2009a, The critical role of climate and saprolite weathering in landscape evolution: Earth Surface Processes and Landforms, v. 34, p. 1507–1521, https://doi.org/10.1002/esp.1836

Dixon, J. L., Heimsath, A. M., Kaste, J., and Amundson, R., 2009b, Climate-driven processes of hillslope weathering: geology, v. 37, p. 975–978, https://doi.org/10.1130/G30045A.1

Dixon, J. L., Hartshorn, A. S., Heimsath, A. M., DiBiase, R. A., and Whipple, K. X., 2012, Chemical weathering response to tectonic forcing: A soils perspective from the San Gabriel Mountains, California: Earth and Planetary Science Letters, v. 323–324, p. 40–49, https://doi.org/10.1016/j.epsl.2012.01.010

Dosseto, A., Buss, H. L., and Suresh, P. O., 2012, Rapid regolith formation over volcanic bedrock and implications for landscape evolution: Earth and Planetary Science Letters, v. 337, p. 47–55, https://doi.org/10.1016/j.epsl.2012.05.008

Egli, M., Dahms, D., and Norton, K., 2014, Soil formation rates on silicate parent material in alpine environments: Different approaches-different results?: Geoderma, v. 213, p. 320–333, https://doi.org/10.1016/j.geoderma.2013.08.016

Egli, M., Mirabella, A., Sartori, G., and Fitze, P., 2003, Weathering rates as a function of climate: results from a climosequence of the Val Genova (Trentino, Italian Alps): Geoderma, v. 111, p. 99–121, https://doi.org/10.1016/S0016-7061(02)00256-2

Egli, M., Mirabella, A., and Sartori, G., 2008, The role of climate and vegetation in weathering and clay mineral formation in late Quaternary soils of the Swiss and Italian Alps: Geomorphology, v. 102, p. 307–324, https://doi.org/10.1016/j.geomorph.2008.04.001

Emberson, R., Hovius, N., Galy, A., and Marc, O., 2016, Chemical weathering in active mountain belts controlled by stochastic bedrock landsliding: Nature Geoscience, v. 9, p. 42–45, https://doi.org/10.1038/ngeo2600

Fan, Y., Miguez-Macho, G., Jobbagy, E. G., Jackson, R. B., and Otero-Casal, C., 2017, Hydrologic regulation of plant rooting depth: Proceedings of the National Academy of Sciences of the United States of America, v. 114, n. 40, p. 10572–10577, https://doi.org/10.1073/pnas.1712381114

Ferrier, K. L., and Kirchner, J. W., 2008, Effects of physical erosion on chemical denudation rates: A numerical modeling study of soil-mantled hillslopes: Earth and Planetary Science Letters, v. 272, p. 591–599, https://doi.org/10.1016/j.epsl.2008.05.024

Ferrier, K. L., and West, N., 2017, Responses of chemical erosion rates to transient perturbations in physical erosion rates, and implications for relationships between chemical and physical erosion rates in regolith-mantled hillslopes: Earth and Planetary Science Letters, v. 474, p. 447–456, https://doi.org/10.1016/j.epsl.2017.07.002

Ferrier, K. L., Kirchner, J. W., and Finkel, R. C., 2011, Estimating millennial-scale rates of dust incorporation into eroding hillslope regolith using cosmogenic nuclides and immobile weathering tracers: Journal of Geophysical Research, v. 116, n. F3, p. F03022, https://doi.org/10.1029/2011JF001991

Ferrier, K. L., Kirchner, J. W., and Finkel, R. C. 2012, Weak influences of climate and mineral supply rates on chemical erosion rates: Measurements along two altitudinal transects in the Idaho Batholith: Journal of Geophysical Research-Earth Surface, v. 117, n. F2, p. F02026, https://doi.org/10.1029/2011JF002231

Fischer, M., Huss, M., Barboux, C., and Hoelzle, M., 2014, The new Swiss Glacier Inventory SGI2010: relevance of using high-resolution source data in areas dominated by very small glaciers: Arctic, Antarctic, and Alpine Research, v. 46, p. 933–945, https://doi.org/10.1657/1938-4246-46.4.933

Frings, P. J., 2019, Palaeoweathering: how do weathering rates vary with climate?: Elements: An International Magazine of Mineralogy, Geochemistry, and Petrology, v. 15, n. 4, p. 259–265, https://doi.org/10.2138/gselements.15.4.259

Frings, P. J., and Buss, H. L., 2019, The Central Role of Weathering in the Geosciences: Elements: An International Magazine of Mineralogy, Geochemistry, and Petrology, v. 15, n. 4, p. 229–234, https://doi.org/10.2138/gselements.15.4.229

Frings, P. J., Clymans, W., Fontorbe, G., De La Rocha, C. L., and Conley, D. J., 2016, The continental Si cycle and its impact on the ocean Si isotope budget: Chemical Geology, v. 425, p. 12–36, https://doi.org/10.1016/j.chemgeo.2016.01.020

Frings, P. J., Oelze, M., Schubring, F., Frick, D. A., and von Blanckenburg, F., 2021a, Interpreting silicon isotopes in the Critical Zone: American Journal of Science, v. 321, n. 8, p. 1164–1203, https://doi.org/10.24.75/08.2021.02

Frings, P. J., Schubring, F., Oelze, M., and von Blanckenburg, F., 2021b, Quantifying biotic and abiotic Si fluxes in the Critical Zone with Ge/Si ratios along a gradient of erosion rates: American Journal of Science, v. 321, n. 8, p. 1204–1245, https://doi.org/10.24.75/08.2021.03

Gabet, E. J., and Mudd, S. M., 2009, A theoretical model coupling chemical weathering rates with denudation rates: geology, v. 37, n. 2, p. 151–154, https://doi.org/10.1130/G25270A.1

Gaillardet, J., Dupre, B., and Viers, J., 2003, Trace elements in river waters, in Hollland, H. D., and Turekian, K. K., editors, Treatise on Geochemistry: Elsevier, v. 5, p. 225–272, https://doi.org/10.1016/B0-08-043751-6/05165-3

Galvagno, M., ms, 2011, Carbon dioxide exchange of an alpine grassland: integration of eddy covariance, proximal sensing and models, Ph.D. thesis, University of Milano-Bicocca, Italy.

Galvagno, M., Wohlfahrt, G., Cremonese, E., Rossini, M., Colombo, R., Filippa, G., Julitta, T., Manca, G., Siniscalco, C., and di Cella, U. M., 2013, Phenology and carbon dioxide source/sink strength of a subalpine grassland in response to an exceptionally short snow season: Environmental Research Letters, v. 8, n. 2, p. 025008, https://doi.org/10.1088/1748-9326/8/2/025008

Ghestem, M., Veylon, G., Bernard, A., Vanel, Q., and Stokes, A., 2013, Influence of plant root system morphology and architectural traits on soil shear resistance: Plant and Soil, v. 377, p. 43–61, https://doi.org/10.1007/s11104-012-1572-1

Godsey, S. E., Hartmann, J., and Kirchner, J. W., 2019, Catchment chemostasis revisited: Water quality responds differently to variations in weather and climate: Hydrological Processes, v. 33, p. 3056–3069, n.24, https://doi.org/10.1002/hyp.13554

Gottselig, N., Amelung, W., Kirchner, J. W., Bol, R., Eugster, W., Granger, S. J., Hernández-Crespo, C., Herrmann, F., Keizer, J. J., Korkiakoski, M., Laudon, H., Lehner, I., Löfgren, S., Lohila, A., Macleod, C. J. A., Mölder, M., Müller, C., Nasta, P., Nischwitz, V., Paul-Limoges, E., Pierret, M. C., Pilegaard, K., Romano, N., Sebastià, M. T., Stähli, M., Voltz, M., Vereecken, H., Siemens, J., and Klumpp, E., 2017, Elemental Composition of Natural Nanoparticles and Fine Colloids in European Forest Stream Waters and Their Role as Phosphorus Carriers: Global Biogeochemical Cycles, v. 31, n. 10, p. 1592–1607, https://doi.org/10.1002/2017GB005657

Gottselig, N., Sohrt, J., Uhlig, D., Nischwitz, V., Weiler, M., and Amelung, W., 2019, Groundwater controls on colloidal transport in forest stream water: Science of the Total Environment, v. 717, p. 134638, https://doi.org/10.1016/j.scitotenv.2019.134638

Granger, D. E., and Riebe, C. S., 2007, Cosmogenic Nuclides in Weathering and Erosion, in Holland, H. D., and Turekian, K. K., editors, Treatise on Geochemistry: Elsevier Ltd., v. 5, p. 1–43, https://doi.org/10.1016/B978-008043751-4/00238-8

Hahm, W. J., Riebe, C. S., Lukens, C. E., and Araki, S., 2014, Bedrock composition regulates mountain ecosystems and landscape evolution: Proceedings of the National Academy of Sciences of the United States of America, v. 111, n. 9, p. 3338–3343, https://doi.org/10.1073/pnas.1315667111

Hasenmueller, E. A., Gu, X., Weitzman, J. N., Adams, T. S., Stinchcomb, G. E., Eissenstat, D. M., Drohan, P. J., Brantley, S. L., and Kaye, J. P., 2017, Weathering of rock to regolith: The activity of deep roots in bedrock fractures: Geoderma, v. 300, p. 11–31, https://doi.org/10.1016/j.geoderma.2017.03.020

Hayes, N. R., Buss, H. L., Moore, O. W., Krám, P., and Pancost, R. D., 2020, Controls on granitic weathering fronts in contrasting climates: Chemical Geology, v. 535, p. 119450, https://doi.org/10.1016/j.chemgeo.2019.119450

Hedin, L. O., Vitousek, P. M., and Matson, P. A., 2003, Nutrient losses over four million years of tropical forest development: Ecology, v. 84, n. 9, p. 2231–2255, https://doi.org/10.1890/02-4066

Heimsath, A. M., Dietrich, W. E., Nishiizumi, K., and Finkel, R. C., 1997, The soil production function and landscape equilibrium: Nature, v. 388, p. 358–361, https://doi.org/10.1038/41056

Hengl, T., de Jesus, J. M., MacMillan, R. A., Batjes, N. H., Heuvelink, G. B. M., Ribeiro, E., Samuel-Rosa, A., Kempen, B., Leenaars, J. G. B., Walsh, M. G., and Gonzalez, M. R., 2014, SoilGrids1km–global soil information based on automated mapping: PLoS One, v. 9, p. e105992, n. 8, https://doi.org/10.1371/journal.pone.0105992

Hewawasam, T., von Blanckenburg, F., Schaller, M., and Kubik, P., 2003, Increase of human over natural erosion rates in tropical highlands constrained by cosmogenic nuclides: Geology, v. 31, n. 7, p. 597–600, https://doi.org/10.1130/0091-7613(2003)031<0597:IOHONE>2.0.CO;2

Hewawasam, T., von Blanckenburg, F., Bouchez, J., Dixon, J. L., Schuessler, J. A., and Maekeler, R., 2013, Slow advance of the weathering front during deep, supply-limited saprolite formation in the tropical Highlands of Sri Lanka: Geochimica et Cosmochimica Acta, v. 118, p. 202–230, https://doi.org/10.1016/j.gca.2013.05.006

Hilley, G. E., Chamberlain, C. P., Moon, S., Porder, S., and Willett, S. D., 2010, Competition between erosion and reaction kinetics in controlling silicate-weathering rates: Earth and Planetary Science Letters, v. 293, n. 1–2, p. 191–199, https://doi.org/10.1016/j.epsl.2010.01.008

Hodson, M. J., White, P. J., Mead, A., and Broadley, M. R., 2005, Phylogenetic variation in the silicon composition of plants: Annals of Botany, v. 96, n. 6, p. 1027–1046, https://doi.org/10.1093/aob/mci255

Hoffland, E., Giesler, R., Jongmans, A. G., and van Breemen, N., 2003, Feldspar tunneling by fungi along natural productivity gradients: Ecosystems, v. 6, p. 739–746, https://doi.org/10.1007/s10021-003-0191-3

Hunsaker, C. T., and Johnson, D. W., 2017, Concentration-discharge relationships in headwater streams of the Sierra Nevada, California: Water Resources Research, v. 53, n. 9, p. 7869–7884, https://doi.org/10.1002/2016WR019693

Hunsaker, C.T., and Neary, D.G., 2012. Sediment loads and erosion in forest headwater streams of the Sierra Nevada, California, in Webb, Ashley A.; Bonell, Mike; Bren, Leon; Lane, Patrick NJ; McGuire, Don; Neary, Daniel G.; Nettles, Jami; Scott, David F.; Stednik, John; Wang, Yanhui, editors, Revisiting Experimental Catchment Studies in Forest Hydrology: Proceedings of a Workshop held during the XXV IUGG General Assembly in Melbourne, June-July 2011, IAHS Publication 353, Wallingford, United Kingdom, International Association of Hydrological Sciences, p. 195–204.

Jobbagy, E. G., and Jackson, R. B., 2001, The distribution of soil nutrients with depth: Global patterns and the imprint of plants: Biogeochemistry, v. 53, p. 51–77, https://doi.org/10.1023/A:1010760720215

Jongmans, A. G., vanBreemen, N., Lundstrom, U., vanHees, P. A. W., Finlay, R. D., Srinivasan, M., Unestam, T., Giesler, R., Melkerud, P. A., and Olsson, M., 1997, Rock-eating fungi: Nature, v. 389, p. 682–683, https://doi.org/10.1038/39493

Joos, O., Hagedorn, F., Heim, A., Gilgen, A. K., Schmidt, M. W., Siegwolf, R., and Buchmann, N., 2010, Summer drought reduces total and litter-derived soil CO2 effluxes in temperate grassland-clues from a C-13 litter addition experiment: Biogeosciences, v. 7, n. 3, p. 1031–1041, https://doi.org/10.5194/bg-7-1031-2010

Jung, M., Reichstein, M., Margolis, H. A., Cescatti, A., Richardson, A. D., Arain, M. A., Arneth, A., Bernhofer, C., Bonal, D., Chen, J. Q., Gianelle, D., Gobron, N., Kiely, G., Kutsch, W., Lasslop, G., Law, B. E., Lindroth, A., Merbold, L., Montagnani, L., Moors, E. J., Papale, D., Sottocornola, M., Vaccari, F., and Williams, C., 2011, Global patterns of land-atmosphere fluxes of carbon dioxide, latent heat, and sensible heat derived from eddy covariance, satellite, and meteorological observations: Journal of Geophysical Research: Biogeosciences, v. 116, n. G3, https://doi.org/10.1029/2010JG001566

Jung, M., Koirala, S., Weber, U., Ichii, K., Gans, F., Camps-Valls, G., Papale, D., Schwalm, C., Tramontana, G., and Reichstein, M., 2019, The FLUXCOM ensemble of global land-atmosphere energy fluxes: Scientific data, v. 6, p. 74, https://doi.org/10.1038/s41597-019-0076-8

Kelly, A. E., and Goulden, M. L., 2016, A montane Mediterranean climate supports year-round photosynthesis and high forest biomass: Tree Physiology, v. 36, n. 4, p. 459–468, https://doi.org/10.1093/treephys/tpv131

Khomo, L., Bern, C. R., Hartshorn, A. S., Rogers, K. H., and Chadwick, O. A., 2013, Chemical transfers along slowly eroding catenas developed on granitic cratons in southern Africa: Geoderma, v. 202-203, p. 192–202, https://doi.org/10.1016/j.geoderma.2013.03.023

Kim, H., Gu, X., and Brantley, S. L., 2018, Particle fluxes in groundwater change subsurface shale rock chemistry over geologic time: Earth and Planetary Science Letters, v. 500, p. 180–191, https://doi.org/10.1016/j.epsl.2018.07.031

Kohfeld, K. E., and Harrison, S. P., 2001, DIRTMAP: the geological record of dust: Earth-Science Reviews, v. 54, n. 1–3, p. 81–114, https://doi.org/10.1016/S0012-8252(01)00042-3

Kump, L. R., and Arthur, M. A., 1997, Global chemical erosion during the Cenozoic: Weatherability balances the budgets, Tectonic Uplift and Climate Change, Springer, p. 399–426, https://doi.org/10.1007/978-1-4615-5935-1_18

Laliberte, E., Grace, J. B., Huston, M. A., Lambers, H., Teste, F. P., Turner, B. L., and Wardle, D. A., 2013, How does pedogenesis drive plant diversity?: Trends in Ecology & Evolution, v. 28, n. 6, p. 331–340, https://doi.org/10.1016/j.tree.2013.02.008

Lambers, H., Raven, J. A., Shaver, G. R., and Smith, S. E., 2008, Plant nutrient-acquisition strategies change with soil age: Trends in Ecology & Evolution, v. 23, n. 2, p. 95–103, https://doi.org/10.1016/j.tree.2007.10.008

Lang, F., Bauhus, J., Frossard, E., George, E., Kaiser, K., Kaupenjohann, M., Krüger, J., Matzner, E., Polle, A., Prietzel, J., Rennenberg, H., and Wellbrock, N., 2016, Phosphorus in forest ecosystems: New insights from an ecosystem nutrition perspective: Journal of Plant Nutrition and Soil Science, v. 179, n. 2, p. 129–135, https://doi.org/10.1002/jpln.201500541

Larsen, I. J., Montgomery, D. R., and Greenberg, H. M., 2014, The contribution of mountains to global denudation: geology, v. 42, n. 6, p. 527–530, https://doi.org/10.1130/G35136.1

Lebedeva, M. I., Fletcher, R. C., and Brantley, S. L., 2010, A mathematical model for steady-state regolith production at constant erosion rate: Earth Surface Processes and Landforms, v. 35, n. 5, p. 508–524, https://doi.org/10.1002/esp.1954

Lehn, G. O., Jacobson, A. D., Douglas, T., McClelland, J., Barker, A., and Khosh, M., 2017, Constraining seasonal active layer dynamics and chemical weathering reactions occurring in North Slope Alaskan watersheds with major ion and isotope (δ34SSO4, δ13CDIC, 87Sr/86Sr, δ44/40Ca, and δ44/42Ca) measurements: Geochimica et Cosmochimica Acta, v. 217, p. 399–420, https://doi.org/10.1016/j.gca.2017.07.042

Lin, H., 2010a, Earth's Critical Zone and hydropedology: concepts, characteristics, and advances: Hydrology and Earth System Sciences, v. 14, p. 25–45, https://doi.org/10.5194/hess-14-25-2010

Lin, H.2010b, Linking principles of soil formation and flow regimes: Journal of Hydrology, v. 393, p. 3–19, https://doi.org/10.1016/j.jhydrol.2010.02.013

Liu, F., Hunsaker, C., and Bales, R. C., 2013, Controls of streamflow generation in small catchments across the snow-rain transition in the Southern Sierra Nevada, California: Hydrological Processes, v. 27, p. 1959–1972, https://doi.org/10.1002/hyp.9304

Lucas, Y., 2001, The role of plants in controlling rates and products of weathering: Importance of biological pumping: Annual Review of Earth and Planetary Sciences, v. 29, p. 135–163, https://doi.org/10.1146/annurev.earth.29.1.135

Lybrand, R. A., and Rasmussen, C., 2014, Linking soil element-mass-transfer to microscale mineral weathering across a semiarid environmental gradient: Chemical Geology, v. 381, p. 26–39, https://doi.org/10.1016/j.chemgeo.2014.04.022

Maher, K., 2010, The dependence of chemical weathering rates on fluid residence time: Earth and Planetary Science Letters, v. 294, n. 1–2, p. 101–110, https://doi.org/10.1016/j.epsl.2010.03.010

Maher, K.2011, The role of fluid residence time and topographic scales in determining chemical fluxes from landscapes: Earth and Planetary Science Letters, v. 312, n. 1–2, p. 48–58, https://doi.org/10.1016/j.epsl.2011.09.040

Maher, K., and Chamberlain, C. P., 2014, Hydrologic regulation of chemical weathering and the geologic carbon cycle: Science, v. 343, n. 6178, p. 1502–1504, https://doi.org/10.1126/science.1250770

Maher, K., and von Blanckenburg, F., 2016, Surface ages and weathering rates from Be-10 (meteoric) and Be-10/Be-9: Insights from differential mass balance and reactive transport modeling: Chemical Geology, v. 446, p. 70–86, https://doi.org/10.1016/j.chemgeo.2016.07.016

Marschner, H., and Marschner, P., 2012, Mineral Nutrition of Higher Plants: London, United Kingdom, Academic Press, p. 889.

Mavris, C., Götze, J., Plötze, M., and Egli, M., 2012, Weathering and mineralogical evolution in a high Alpine soil chronosequence: A combined approach using SEM-EDX, cathodoluminescence and Nomarski DIC microscopy: Sedimentary Geology, v. 280, p. 108–118, https://doi.org/10.1016/j.sedgeo.2012.04.008

McCorkle, E. P., Berhe, A. A., Hunsaker, C. T., Johnson, D. W., McFarlane, K. J., Fogel, M. L., and Hart, S. C., 2016, Tracing the source of soil organic matter eroded from temperate forest catchments using carbon and nitrogen isotopes: Chemical Geology, v. 445, p. 172–184, https://doi.org/10.1016/j.chemgeo.2016.04.025

Meybeck, M., 2003, Global occurrence of major elements in rivers: Treatise on Geochemistry, v. 5, p. 207–223, https://doi.org/10.1016/B0-08-043751-6/05164-1

Milliman, J. D., and Farnsworth, K. L., 2011, River discharge to the coastal ocean . A global synthesis: Cambridge, United Kingdom, Cambridge University Press, 384 p.

Misra, S., and Froelich, P. N., 2012, Lithium Isotope History of Cenozoic Seawater: Changes in Silicate Weathering and Reverse Weathering: Science, v. 335, n. 6070, p. 818–823, https://doi.org/10.1126/science.1214697

Moulton, K. L., West, A. J., and Berner, R. A., 2000, Solute flux and mineral mass balance approaches to the quantification of plant effects on silicate weathering: American Journal of Science, v. 300, n. 7, p. 539–570, https://doi.org/10.2475/ajs.300.7.539

Norton, K. P., and von Blanckenburg, F., 2010, Silicate weathering of soil-mantled slopes in an active Alpine landscape: Geochimica et Cosmochimica Acta, v. 74, p. 5243–5258, https://doi.org/10.1016/j.gca.2010.06.019

Norton, K. P., von Blanckenburg, F., and Kubik, P. W., 2010, Cosmogenic nuclide-derived rates of diffusive and episodic erosion in the glacially sculpted upper Rhone Valley, Swiss Alps: Earth Surface Processes and Landforms, v. 35, p. 651–662,https://doi.org/10.1002/esp.1961

Oeser, R. A., Stroncik, N., Moskwa, L.-M., Bernhard, N., Schaller, M., Canessa, R., van den Brink, L., Köster, M., Brucker, E., Stock, S., Fuentes, J. P., Godoy, R., Matus, F. J., Pedraza, R. O., McIntype, P. O., Paulino, L., Seguel, O., Bader, M. Y., Boy, J., Dippold, M. A., Ehlers, T. A., Kühn, P., Kuzyakov, Y., Leinweber, P., Scholten, T., Spielvogel, S., Spohn, M., Übernickel, K., Tielbörger, K., Wagner, D., and von Blanckenburg, F., 2018, Chemistry and microbiology of the Critical Zone along a steep climate and vegetation gradient in the Chilean Coastal Cordillera: Catena, v. 170, p. 183–203, https://doi.org/10.1016/j.catena.2018.06.002

Oeser, R. A., and von Blanckenburg, F., 2020a, Do degree and rate of silicate weathering depend on plant productivity?: Biogeosciences, v. 17, p. 4883–4917, https://doi.org/10.5194/bg-17-4883-2020

Oeser, R. A., and von Blanckenburg, F.2020b, Strontium isotopes trace biological activity in the Critical Zone along a climate and vegetation gradient: Chemical Geology, v. 558, p. 119861, https://doi.org/10.1016/j.chemgeo.2020.119861

O'Geen, A. T., Safeeq, M., Wagenbrenner, J., Stacy, E., Hartsough, P., Devine, S., Tian, Z., Ferrell, R., Goulden, M., and Hopmans, J. W., 2018, Southern Sierra Critical Zone Observatory and Kings River Experimental Watersheds: A synthesis of measurements, new insights, and future directions: Vadose Zone Journal, v. 17, n. 1, p. 1–18, https://doi.org/10.2136/vzj2018.04.0081

Opfergelt, S., and Delmelle, P., 2012, Silicon isotopes and continental weathering processes: Assessing controls on Si transfer to the ocean: Comptes Rendus Geoscience, v. 344, p. 723–738, https://doi.org/10.1016/j.crte.2012.09.006

Pagani, M., Caldeira, K., Berner, R., and Beerling, D. J., 2009, The role of terrestrial plants in limiting atmospheric CO(2) decline over the past 24 million years: Nature, v. 460, p. 85–88, https://doi.org/10.1038/nature08133

Pawlik, Ł., Phillips, J. D., and Šamonil, P., 2016, Roots, rock, and regolith: Biomechanical and biochemical weathering by trees and its impact on hillslopes-A critical literature review: Earth-Science Reviews, v. 159, p. 142–159, https://doi.org/10.1016/j.earscirev.2016.06.002

Pogge von Strandmann, P. A. E., Jenkyns, H. C., and Woodfine, R. G., 2013, Lithium isotope evidence for enhanced weathering during Oceanic Anoxic Event 2: Nature Geoscience, v. 6, p. 668–672, https://doi.org/10.1038/ngeo1875

Porder, S., 2019, How plants enhance weathering and how weathering is important to plants: Elements: An International Magazine of Mineralogy, Geochemistry, and Petrology, v. 15, n. 4, p. 241–246, https://doi.org/10.2138/gselements.15.4.241

Porder, S., and Hilley, G. E., 2011, Linking chronosequences with the rest of the world: predicting soil phosphorus content in denuding landscapes: Biogeochemistry, v. 102, p. 153–166, https://doi.org/10.1007/s10533-010-9428-3

Porder, S., Vitousek, P. M., Chadwick, O. A., Chamberlain, C. P., and Hilley, G. E., 2007, Uplift, erosion, and phosphorus limitation in terrestrial ecosystems: Ecosystems, v. 10, p. 158–170, https://doi.org/10.1007/s10021-006-9011-x

Portenga, E. W., and Bierman, P. R., 2011, Understanding Earth's eroding surface with 10Be: GSA Today, v. 21, p. 4–10, https://doi.org/10.1130/G111A.1

Reimann, C., Koller, F., Frengstad, B., Kashulina, G., Niskavaara, H., and Englmaier, P., 2001, Comparison of the element composition in several plant species and their substrate from a 1 500 000–km2 area in Northern Europe: Science of The Total Environment, v. 278, n. 1–3, p. 87–112, https://doi.org/10.1016/S0048-9697(00)00890-1

Riebe, C. S., and Granger, D. E., 2013, Quantifying effects of deep and near-surface chemical erosion on cosmogenic nuclides in soils, saprolite, and sediment: Earth Surface Processes and Landforms, v. 38, n. 5, p. 523–533, https://doi.org/10.1002/esp.3339

Riebe, C. S., Kirchner, J. W., and Finkel, R. C., 2003, Long-term rates of chemical weathering and physical erosion from cosmogenic nuclides and geochemical mass balance: Geochimica et Cosmochimica Acta, v. 67, n. 22, p. 4411–442, https://doi.org/10.1016/S0016-7037(03)00382-X

Riebe, C. S., Hahm, W. J., and Brantley, S. L., 2017, Controls on deep critical zone architecture: a historical review and four testable hypotheses: Earth Surface Processes and Landforms, v. 42, p. 128–156, n. 1, https://doi.org/10.1002/esp.4052

Riotte, J., Maréchal, J. C., Audry, S., Kumar, C., Bedimo Bedimo, J. P., Ruiz, L., Sekhar, M., Cisel, M., Chitra Tarak, R., Varma, M. R. R., Lagane, C., Reddy, P., and Braun, J. J., 2014, Vegetation impact on stream chemical fluxes: Mule Hole watershed (South India): Geochimica et Cosmochimica Acta, v. 145, p. 116–138, https://doi.org/10.1016/j.gca.2014.09.015

Sauer, D., Schellmann, G., and Stahr, K., 2007, A soil chronosequence in the semi-arid environment of Patagonia (Argentina): Catena, v. 71, n. 3, p. 382–393, https://doi.org/10.1016/j.catena.2007.03.010

Schoelynck, J., Subalusky, A. L., Struyf, E., Dutton, C. L., Unzué-Belmonte, D., Van de Vijver, B., Post, D. M., Rosi, E. J., Meire, P., and Frings, P., 2019, Hippos (Hippopotamus amphibius): The animal silicon pump: Science Advances, v. 5, n. 5, p. eaav0395, https://doi.org/10.1126/sciadv.aav0395

Schoonejans, J., Vanacker, V., Opfergelt, S., Granet, M., and Chabaux, F., 2016, Coupling uranium series and 10Be cosmogenic radionuclides to evaluate steady-state soil thickness in the Betic Cordillera: Chemical Geology, v. 446, p. 99–109, https://doi.org/10.1016/j.chemgeo.2016.03.030

Schuessler, J. A., Kämpf, H., Koch, U., and Alawi, M., 2016, Earthquake impact on iron isotope signatures recorded in mineral spring water: Journal of Geophysical Research: Solid Earth, v. 121, p. 8548–8568, https://doi.org/10.1002/2016JB013408

Schuessler, J. A., von Blanckenburg, F., Bouchez, J., Uhlig, D., and Hewawasam, T., 2018, Nutrient cycling in a tropical montane rainforest under a supply-limited weathering regime traced by elemental mass balances and Mg stable isotopes: Chemical Geology, v. 497, p. 74–87, https://doi.org/10.1016/j.chemgeo.2018.08.024

Smits, M. M., Bonneville, S., Benning, L. G., Banwart, S. A., and Leake, J. R., 2012, Plant-driven weathering of apatite - the role of an ectomycorrhizal fungus: Geobiology, v. 10, n. 5, p. 445–456, https://doi.org/10.1111/j.1472-4669.2012.00331.x

Stallard, R. F., 1995, Tectonic, environmental, and human aspects of weathering and erosion: A Global Review using a Steady-State Perspective: Annual Review of Earth Planetary Sciences, v. 23, p. 11–39, https://doi.org/10.1146/annurev.ea.23.050195.000303

Stille, P., Steinmann, M., Pierret, M.-C., Gauthier-Lafaye, F., Chabaux, F., Viville, D., Pourcelot, L., Matera, V., Aouad, G., and Aubert, D., 2006, The impact of vegetation on REE fractionation in stream waters of a small forested catchment (the Strengbach case): Geochimica et Cosmochimica Acta, v. 70, n. 13, p. 3217–3230, https://doi.org/10.1016/j.gca.2006.04.028

Sullivan, P. L., Ma, L., West, N., Jin, L., Karwan, D. L., Noireaux, J., Steinhoefel, G., Gaines, K. P., Eissenstat, D. M., Gaillardet, J., Derry, L. A., Meek, K., Hynek, S., and Brantley, S. L., 2016, CZ-tope at Susquehanna Shale Hills CZO: Synthesizing multiple isotope proxies to elucidate Critical Zone processes across timescales in a temperate forested landscape: Chemical Geology, v. 445, p. 103–119, https://doi.org/10.1016/j.chemgeo.2016.05.012

Trostle, K. D., Ray Runyon, J., Pohlmann, M. A., Redfield, S. E., Pelletier, J., McIntosh, J., and Chorover, J., 2016, Colloids and organic matter complexation control trace metal concentration-discharge relationships in Marshall Gulch stream waters: Water Resources Research, v. 52, n. 10, p. 7931–7944, https://doi.org/10.1002/2016WR019072

Turowski, J. M., Hilton, R. G., and Sparkes, R., 2016, Decadal carbon discharge by a mountain stream is dominated by coarse organic matter: Geology, v. 44, n. 1, p. 27–30, https://doi.org/10.1130/G37192.1

Uhlig, D., and von Blanckenburg, F., 2019, How Slow Rock Weathering Balances Nutrient Loss During Fast Forest Floor Turnover in Montane, Temperate Forest Ecosystems: Frontiers in Earth Science, v. 7, p. 159, https://doi.org/10.3389/feart.2019.00159

Uhlig, D., Schuessler, J. A., Bouchez, J., Dixon, J. L., and von Blanckenburg, F., 2017, Quantifying nutrient uptake as driver of rock weathering in forest ecosystems by magnesium stable isotopes: Biogeosciences, v. 14, p. 3111–3128, https://doi.org/10.5194/bg-14-3111-2017

Uhlig, D., Amelung, W., and Blanckenburg, F., 2020, Mineral Nutrients Sourced in Deep Regolith Sustain Long-Term Nutrition of Mountainous Temperate Forest Ecosystems: Global Biogeochemical Cycles, v. 34, n. 9, p. e2019GB006513, https://doi.org/10.1029/2019GB006513

Uroz, S., Calvaruso, C., Turpault, M. P., and Frey-Klett, P., 2009, Mineral weathering by bacteria: ecology, actors and mechanisms: Trends in Microbiology, v. 17, n. 8, p. 378–387, https://doi.org/10.1016/j.tim.2009.05.004

Vandevenne, F., Struyf, E., Clymans, W., and Meire, P., 2012, Agricultural silica harvest: have humans created a new loop in the global silica cycle?: Frontiers in Ecology and the Environment, v. 10, p. 243–248, https://doi.org/10.1890/110046

Vitousek, P. M., and Farrington, H., 1997, Nutrient limitation and soil development: Experimental test of a biogeochemical theory: Biogeochemistry, v. 37, p. 63–75, https://doi.org/10.1023/A:1005757218475

Vitousek, P., Chadwick, O., Matson, P., Allison, S., Derry, L., Kettley, L., Luers, A., Mecking, E., Monastra, V., and Porder, S., 2003, Erosion and the rejuvenation of weathering-derived nutrient supply in an old tropical landscape: Ecosystems, v. 6, p. 762–772, https://doi.org/10.1007/s10021-003-0199-8

von Blanckenburg, F., 2005, The control mechanisms of erosion and weathering at basin scale from cosmogenic nuclides in river sediment: Earth and Planetary Science Letters, v. 237, n. 3–4, p. 462–479, https://doi.org/10.1016/j.epsl.2005.06.030

von Blanckenburg, F., Hewawasam, T., and Kubik, P. W., 2004, Cosmogenic nuclide evidence for low weathering and denudation in the wet, tropical highlands of Sri Lanka: Journal of Geophysical Research-Earth Surface, v. 109, n. F3, https://doi.org/10.1029/2003JF000049

von Blanckenburg, F., Bouchez, J., and Wittmann, H., 2012, Earth surface erosion and weathering from the 10Be(meteoric)/9Be ratio: Earth and Planetary Science Letters, v. 351–352, p. 295–305, https://doi.org/10.1016/j.epsl.2012.07.022

von Blanckenburg, F., Wittmann, H., and Schuessler, J. A., 2016, HELGES: Helmholtz Laboratory for the Geochemistry of the Earth Surface: Journal of large-scale research facilities JLSRF, v. 2, https://doi.org/10.17815/jlsrf-2-141

von Blanckenburg, F., Schuessler, J. A., Bouchez, J., Frings, P. J., Uhlig, D., Oelze, M., Frick, D. A., Hewawasam, T., Dixon, J. E., and Norton, K., 2021, Geochemical data on rock weathering in a global erodosequence: GFZ Data Services, v. , https://doi.org/10.5880/GFZ.3.3.2021.001

Wagenbach, D., and Geis, K., 1989, The mineral dust record in a high altitude Alpine glacier (Colle Gnifetti, Swiss Alps) Paleoclimatology and paleometeorology: modern and past patterns of global atmospheric transport, Springer, p. 543–564, https://doi.org/10.1007/978-94-009-0995-3_23

Waldbauer, J. R., and Chamberlain, C. P., 2005, Influence of uplift, weathering, and base cation supply on past and future CO 2 levels, in Baldwin, I. T., Caldwell, M. M., Heldmaier, G., Jackson, R. B., Lange, O. L., Mooney, H. A., Schulze, E.-D., Sommer, U., Ehleringer, J. R., Dearing, M. D., and Cerling, T. E., editors: A history of atmospheric CO2 and its effects on Plants, Animals, and Ecosystems: New York, Springer, v. 177, p. 166–184, https://doi.org/10.1007/0-387-27048-5_8

Wardle, D. A., Walker, L. R., and Bardgett, R. D., 2004, Ecosystem properties and forest decline in contrasting long-term chronosequences: Science, v. 305, p. 509–513, https://doi.org/10.1126/science.1098778

Weerakkody, J., and Parkinson, D., 2006a, Input, accumulation and turnover of organic matter, nitrogen and phosphorus in surface organic layers of an upper montane rainforest in Sri Lanka: Pedobiologia, v. 50, n. 4, p. 377–383, https://doi.org/10.1016/j.pedobi.2006.06.006

Weerakkody, J., and Parkinson, D.2006b, Leaf litter decomposition in an upper montane rainforest in Sri Lanka: Pedobiologia, v. 50, p. 387–395, n. 5, https://doi.org/10.1016/j.pedobi.2006.07.002

White, A. F., Schulz, M. S., Vivit, D. V., Blum, A. E., Stonestrom, D. A., and Anderson, S. P., 2008, Chemical weathering of a marine terrace chronosequence, Santa Cruz, California I: Interpreting rates and controls based on soil concentration-depth profiles: Geochimica et Cosmochimica Acta, v. 72, n. 1, p. 36–68, https://doi.org/10.1016/j.gca.2007.08.029

Wilcke, W., Velescu, A., Leimer, S., Bigalke, M., Boy, J., and Valarezo, C., 2017, Biological versus geochemical control and environmental change drivers of the base metal budgets of a tropical montane forest in Ecuador during 15 years: Biogeochemistry, v. 136, p. 167–189, https://doi.org/10.1007/s10533-017-0386-x

Wohl, E., Dwire, K., Sutfin, N., Polvi, L., and Bazan, R., 2012, Mechanisms of carbon storage in mountainous headwater rivers: Nature Communications, v. 3, p. 1263, https://doi.org/10.1038/ncomms2274

Yoo, K., Amundson, R., Heimsath, A. M., Dietrich, W. E., and Brimhall, G. H., 2007, Integration of geochemical mass balance with sediment transport to calculate rates of soil chemical weathering and transport on hillslopes: Journal of Geophysical Research: Earth Surface, v. 112, n. F2, p. 15, https://doi.org/10.1029/2005JF000402

Zhang, Y., Xiao, X., Wu, X., Zhou, S., Zhang, G., Qin, Y., and Dong, J., 2017, A global moderate resolution dataset of gross primary production of vegetation for 2000–2016: Scientific data, v. 4, p. 170165, https://doi.org/10.1038/sdata.2017.165

Zhao, M., Heinsch, F. A., Nemani, R. R., and Running, S. W., 2005, Improvements of the MODIS terrestrial gross and net primary production global data set: Remote Sensing of Environment, v. 95, n. 2, p. 164–176, https://doi.org/10.1016/j.rse.2004.12.011

Zhao, M., Running, S. W., and Nemani, R. R., 2006, Sensitivity of Moderate Resolution Imaging Spectroradiometer (MODIS) terrestrial primary production to the accuracy of meteorological reanalyses: Journal of Geophysical Research: Biogeosciences, v. 111, n. G1, https://doi.org/10.1029/2004JG000004

Zhi, W., Li, L., Dong, W., Brown, W., Kaye, J., Steefel, C., and Williams, K. H., 2019, Distinct Source Water Chemistry Shapes Contrasting Concentration-Discharge Patterns: Water Resources Research, v. 55, n. 5, p. 4233–4251, https://doi.org/10.1029/2018WR024257